UNIVERSITAT POLITÈCNICA DE CATALUNYA
BARCELONATECH

ESCOLA TÈCNICA SUPERIOR D'ENGINYERS DE CAMINS, CANALS I PORTS DE BARCELONA

MASTER IN NUMERICAL METHODS IN ENGINEERING

MASTER THESIS

Analysis of droplet dynamics on the GDL surface of a PEM fuel cell cathode

---

Author:
Àlex Jarauta Arabí

Supervisor:
Marino Arroyo Balaguer
External Supervisors:
Marc Secanell Gallart (UofA)
Jordi Pons i Prats (CIMNE)

June 28, 2013

Abstract

Water management is one of the key factors in fuel cell performance. The water produced within the fuel cell is evacuated through the gas channels, but at high current densities water can block the channel, thus limiting the current density generated in the fuel cell. A semi-analytical model of a water droplet emerging from a pore of the GDL surface in a PEM fuel cell channel is developed. The geometry of the static and deformed shape is characterized and the main geometric variables (i.e. radius, height, perimeter) only depend on the contact angles. The forces acting on the droplet are the drag force of the air and the surface tension force, which acts as adhesion force. The drag coefficient is computed numerically for the working conditions and is characterized as a linear function depending on the Reynolds number and the hysteresis angle. The computed drag coefficient is bigger compared with the drag coefficient computed with the equation found in literature. The governing equation of the droplet dynamics is Newton's Second Law applied to the x-coordinate of the center of mass, and it is solved with fourth-order Runge-Kutta method. The analytical study solves the problem of a growing droplet in a gas flow channel to see the effects of: i) air velocity and liquid mass flow in droplet deformation and oscillation; and, ii) droplet height in frequency of oscillation. Results show the oscillations of the droplet as it emerges from the pore. The predicted values for both drag and surface tension force are higher than the results found in literature. Higher air velocity values lead to more deformation of the droplet and oscillation with lower frequency but higher amplitude. Similar effects have been identified when the liquid mass flow is increased, leading to faster detachment of the droplet. The predicted frequency oscillation values are significantly lower than the values from literature, but these results are obtained for different water injection conditions.

Table of Contents

List of Figures

List of Tables

Acknowledgements

I would like to thank Eugenio Oñate for giving me the opportunity of becoming a member of CIMNE.

I would also like to thank my supervisors Marino Arroyo, Marc Secanell and Jordi Pons for their guidance and support during the writing of this thesis. Marc, thanks for offering me the opportunity to go to Edmonton, for all the interesting discussions that we had and for your patience during these months. Jordi, thanks again for your encouragement and support, and being interested in my research as much as I am.

Thanks also to the ESDLab people for making me feel at home during my stay in Edmonton, to my office mates in Castelldefels for your companionship and also thanks to my friends for their support.

I thank my parents, Eusebi and Adolfina, for giving me the opportunity of study and showing me the importance of learning. Thanks for all your support, patience and encouragement. Thanks also to my brother Eduard for his support and making me feel closer to home when I was in Edmonton.

Last but not least, I would like to thank my beloved girlfriend Cris for her love and patience, for helping me write this thesis and smiling when the droplet started to dance on the screen. Thanks for your patience during last year, despite the huge distance between us and thank you for being by my side during all these wonderful years and making me a better person.

Thanks to all af you because I could not have written this thesis without your support.

Chapter 1

Introduction

A fuel cell is an electrochemical device that has the ability to turn the chemical energy in a fuel directly into electricity with high efficiency. Inside the fuel cell, oxidation and reduction electrochemical reactions take place producing low-voltage current (DC) and heat. The former is used to do useful work while the latter is wasted or can be used in cogeneration applications. Fuel cells are usually compared with other energy convertors, like reciprocating engines or batteries. Batteries and fuel cells have the same operating principle, based on the electrochemical reactions at the anode and the cathode. The main difference being that batteries store the reactant inside the cell instead of in a separate storage tank.

There are different types of fuel cells depending on the materials used in the electrolytes, the substances that react in the anode and the cathode or the working temperature. The current work focuses on Polymer Electrolyte Membrane (PEM) fuel cells, which can work between -40 and 100°C and use hydrogen as fuel, oxygen as cathode reactant and Nafion® as the electrolyte (Figure 1.1).

The working principle of the PEM fuel cell is based on two electrochemical reactions. The process starts at the anode, where the hydrogen flows in the anode Gas Flow Channel (GFC) and diffuses through the pores in the Gas Diffusion Layer (GDL). Attached to the GDL is the Catalyst Layer (CL). The CL is made using a platinum-based ink which is painted on either the PEM or the GDL. The ink contains carbon, Pt and electrolyte. The resulting coating is a thin (about 10 μm) porous layer. The Pt catalyses the first reaction: the hydrogen oxidation reaction.

$$\mathrm{H_2} \longrightarrow \mathrm{2H^+ + 2e^-} \tag{1.1}$$

After this reaction, the next layer is the membrane which is made of Nafion®. The membrane allows the protons to travel across its section but it is impermeable for the electrons and gases. The electrons have to go back through the GDL and the current collector (that act as the walls of the anode gas flow channel) in order to meet the protons at the other side of the membrane, thus generating the desired electric current. In the cathode, the oxygen flows in the cathode gas channels, diffuses through the GDL and in the catalyst layer reacts with the protons from the membrane, performing the second reaction:

$$\mathrm{2H^+ + 2e^-} + \frac{1}{2}\mathrm{O_2} \longrightarrow \mathrm{2H_2O} \tag{1.2}$$

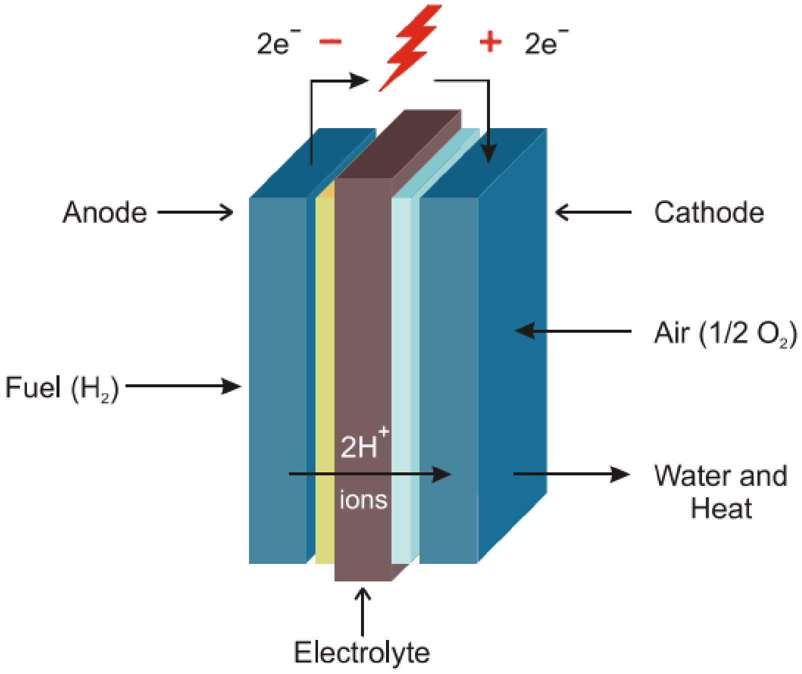

Figure 1.1: Schematic view of a PEM fuel cell [1]

The union of the anode GDL and CL, membrane and cathode CL and GDL is also known as Membrane Electrode Assembly (MEA). When fuelled with hydrogen, the fuel cell has zero emissions, since the only product of the electrochemical reaction is water and heat. The water generated in the reaction is one of the key factors influencing the fuel cell performance. The membrane needs water in order to conduct the protons; if there is not enough water, the membrane dries out and the fuel cell cannot work any longer. Alternatively, if there is too much water, the pores in the CL and GDL flood preventing the reactant gases from diffusing through it. The exceeding water has therefore to be evacuated through the cathode gas channels. This is the starting point of the present work.

There are three types of two-phase flow in the gas channels depending on different factors. Their names change depending on the author, however, these flows are usually known as droplet, film and slug flow [2], as shown on Figure 1.2.

The present work focuses on droplet flow and the conditions that lead to film and slug flow. Since it is very difficult to develop an analytical equation for the shape of a water film, the best way to proceed is the analysis of a single static and deformed droplet and then identify the conditions that lead to film and slug flow formation. In addition, the area coverage of the formed droplets is another variable that needs to be considered, and this variable takes values from 0 to 1 only when the flow is identified as droplet flow.

1.1 Motivation

Water management is one of the most critical issues in fuel cell design. During operation a fuel cell produces water. At moderate current densities the water can

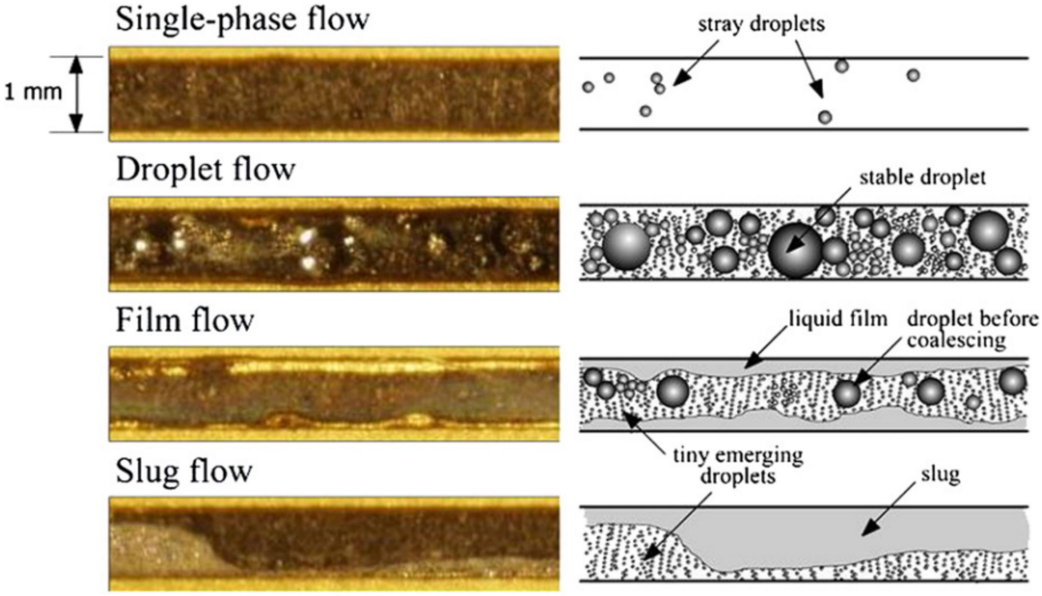

Figure 1.2: Flow types that can be found in a PEMFC cathode channel. Reproduced from reference [2]

leave the cell in vapour form. At high current densities however, water vapour condenses in the GDL blocking the pores in the layer and blocking the gas channels [3], [4], [5], [6], [7], [8], [9], [10]. Blocking of the pores in the GDL leads to a lack of reactant at the reaction site and a limited current density is reached. Similarly channel blockage leads to non-uniform gas distribution and large pressure losses. As a result, a limiting current density is also reached. If water removal from the cell could be improved, higher current densities could be reached leading to fuel cells that achieve higher power with the same material. This would make fuel cells cheaper, lighter and smaller. Therefore, understanding how water is removed from the cell is critical, in addition to the understanding of the following points:

a) The most important issue to solve is that MEA models need to predict channel water removal rate. Currently, there are excellent MEA models but the boundary conditions for the channel side are very poor. Since two-phase channel models are too complicated, a simple but yet accurate analytical model is needed.

b) Description of the water droplet geometry as it deforms due to the air flowing around. The forces acting on the droplet depend on the current geometry, so it is vital to have it fully characterized in order to obtain an accurate value of the forces.

c) Optimal flow rate to remove the droplet and to predict the flow regime (Figure 1.2). The detachment velocity is a key factor of the water removal from the gas channel, hence its importance when a model is developed.

d) Area covereage of the water in the GDL surface of the channel. This variable is an indicator of the available area for the oxygen to diffuse through the GDL. If the area is fully covered, the fuel cell cannot operate.

e) Drag coefficient C_{D} characterization for the droplet in its static and defomed shapes. The drag force is responsible for the droplet deformation, and it has a linear relationship with the drag coefficient. Thus, it is important to have the values of this coefficient for the different flow regimes and droplet deformation states.

f) Two-phase flow in the channel and porous media (GDL) is very difficult to describe analytically, so a numerical modelling is needed. Most of the numerical models seen in the literature use the Volume of Fluid (VOF) method. New methods should be used in order to check accuracy or achieve computational cost improvements.

g) Lack of experimental data on droplet emergence, growth, oscillation and detachment in a fuel cell channel. The results obtained with the analytical model need to be validated with an experiment under the conditions considered in the model.

Because of all the aforementioned reasons, the author of this work has been motivated to study and develope an improved analytical model of a water droplet emerging from a pore of the GDL in a cathode channel of a PEM fuel cell. In the future, points *f* and *g* will also be addressed.

1.2 Literature Review

It is well known that water management is a key factor in the behavior of PEMFCs [4]. Several studies have been focused on the development of a water droplet in a cathode channel [3], [11], [4], [5], [6]. Finding the conditions that lead to droplet shedding is the main objective of these works.

The following sections are a review of the work done so far regarding two main topics. The first one corresponds to the analysis of a single water droplet laying on a surface subjected to different forces, such as airflow drag and gravity forces. The second part is focused on the works done so far on the analysis of a PEM fuel cell cathode channel. In the latter, the analytical models are reviewed highlighting the most important features of the droplet modeling, as well as the the different numerical simulations that have been carried out up to the present day, and the experiments done so far.

1.2.1 Water droplet shedding

Most of the numerical studies regarding the simulation of droplet growth and deformation use the Volume of Fluid method to solve this complex problem. The first published work about this method was released in 1981 by Hirt and Nichols [12], and it was not a numerical method by itself. In fact, it was based on the continuity equation applied to the volume fraction variable (C_{k}), which was used together with the mass and momentum equations. The former read:

$$\frac{\partial}{\partial t}\left(C_{\mathrm{k}}\rho_{\mathrm{k}}\right)+\nabla\cdot\left(C_{\mathrm{k}}\rho_{\mathrm{k}}\vec{u}_{\mathrm{k}}\right)=0 \tag{1.3}$$

where ρ_{k} and $\vec{u}_{\mathrm{k}}$ are the density and the velocity of the fluid k, respectively. On the other hand, C_{k} is the volume fraction variable, and its value is 0 for the nodes outside the fluid, 1 inside the fluid and between 0 and 1 when the considered element contains the interface between two fluids. Consequently, the interface between fluids could be determined by applying that surface-tracking technique to a fixed Eulerian mesh, thus enabling the user to know the location and shape of it [4], [6]. That method, however, had some drawbacks. For example, the advective term of equation (1.3) was very difficult to discretize due to the jump of the volume fraction function in the interface [13], but the analysis of the VOF method goes beyond the scope of the present work. If the reader is interested, further information about the VOF method analysis can be found in [13].

One of the first works reported on the literature that analyzed water droplets was done by Dussan and Chow [14] in 1983. In this work, the authors did a numerical study of the shape of the contact line when the gravitational force was acting on the droplet. The governing equations used where the momentum and mass conservation equations, together with stress and velocity boundary conditions in the fluid-fluid interface. It is important to remark that the problem was formulated with the assumption of constant volume for the droplet. Depending on the applied conditions, the authors concluded that the contact line had an optimal shape, which was characterized by some geometrical variables. Even though the results proved to be promising, the whole study was based on the hypothesis that the slope of the interface between both fluids was small.

An experimental study was done by Extrand and Kumagai in 1995 [15]. The objective of the study was to find out the effects of the chemical nature and the roughness of a surface on the contact angle hysteresis and the retentive force when a water droplet was laying on a tilted plane. An important conclusion of the study was that the nature of the surface, which defines the contact angle with the droplet, was the dominant factor of the droplet deformation. In other words, the effects of roughness on the contact angle hysteresis were negligible when compared to the surface composition [15]

In 1997, Dimitrakopoulos and Higdon numerically investigated the deformation of droplets laying on surfaces subjected to low-Reynolds shear flows [16]. The governing equations for both the droplet and the surrounding fluid were again the mass and momentum equations, and some velocity and tension boundary conditions were applied at the interface. The equations were solved using an iterative method combined with the spectral boundary element method, giving some results for the velocity of both fluids and the interface deformation. Despite the complex formulation and numerical solution of the problem, one can observe some gaps on it. One example are the triple contact points, that had the no-slip boundary condition applied on them but they moved anyways. An extension of that work can be found in [17], were the problem is analyzed in 3 dimensions and the zones of the contact line that violate the no-slip boundary condition are identified.

Recend trends on water droplet dynamics are reducing the working scale to the molecular size. In other words, researchers have realised that the best way to characterize the water droplet shape at any state is to model it as a subset of particles. Although these studies go beyond the scope of the present work, the results shown could give a different point of view for the studies in the macroscopic scale. As an example, two studies that should be considered are [18] and [19]. These works could contribute to the points b, d and f from section 1.1, but the rest would remain without any improvement.

1.2.2 Fuel cell channels

Chen et al. [8] published an analytical model of a water droplet in a PEMFC cathode channel based on a macroscopic force balance. Other works of liquid droplets dynamics in solid surfaces are reported in the literature, but this study was the first one regarding a water droplet subjected to an airflow and laying on a porous surface [8]. In their work, they performed a force balance on a droplet with a preset shape in equilibrium , thus being able to find a relationship between the surface tension force and the external forces acting on the droplet, i.e. pressure, shear and viscous forces. The force balance resulted in a single equation relating the flow conditions, i.e. mean velocity and air viscosity, and the droplet geometrical variables, namely height, length and contact angle hysteresis. The last term will be further described, but it is defined as the difference between the advancing and the receding angles, which are the contact angles when the droplet is in its deformed state. The analytical study was steady-state since it was based on the equilibrium of the forces acting on the droplet.

The conclusions extracted from [8] refered to the channel geometry and some other properties. Firstly, if the channel length-to-height aspect radio by the capillary number was greater than $\frac{\pi}{12}$, the droplets could be prevented from lodging in the channel. In addition, lengthening the GFC while holding the other parameters fixed enlarged the instability window (the angle hysteresis that promotes the droplet removal). The same effect could be achieved if the mean gas flow velocity was increased, which meant that the pressure drop in the channel was higher. The last conclusion was that by increasing the static contact angle, or equivalently, making the GDL/GFC interface more hydrophobic, water droplets could be prevented from lodging in the channel. The main drawback of that model was that it did not take into account the effect of pinning (i.e., the contact area between the droplet and the GDL surface was considered to be always circular), which was a key aspect for the droplet detachment [20]. Additionally, the points b, e, d and f from section 1.1 were not fulfilled.

Kumbur et al. [7] developed a model of a water droplet in the flow channel of a PEM fuel cell in order to predict its detachment. By means of a macroscopic force balance a relationship was found between the geometrical parameters of the droplet and channel parameters, such as the height, the hydrophobicity of the bottom surface and the airflow velocity. An experiment was carried out, and the experimental data extracted was used to find a model that related the content of Teflon in the GDL surface and the surface tension. Thus, they improved Chen's work by relating the contact angle hysteresis with the flow conditions, the Teflon content in the GDL and the roughness of the surface, in addition to several geoemtric variables. Nevertheless, they still could not explain b, e, d and g. An important conclusion is that at low air velocities, the droplet instability was insensitive to the hydrophobicity of the surface. That fact could be used to minimize costs in the PEMFC manufacture and avoid efficiency loss, since a highly hydrophobic GDL has more electrical resistance and is more expensive [7]. The analytical equations in this study were also based on the equilibrium of forces, i.e. it was a steady-state analysis. Thus, no transient analytical model was yet developed.

An exhaustive analysis of the static and deformed shape of the water droplet was done by Esposito et al. [20]. While the study of Kumbur et al. gave an analytical expression for the hysteresis angle, it did not characterized the main geometric variables of the static and deformed droplet. In other words, the points b) and d) from section 1.1 were still not explained. This study was an improvement compared with the two previous works since the analytical model was transient and the effects of the forces on the droplet were a function of time. In the work of Esposito et al., several geometric properties, such as advancing angle, droplet radius, height and perimeter, were expressed as a function of the center of mass x-coordinate (x_{CM}) for a fixed droplet volume. Although the wetting area over the GDL was approximated by a cylinder, results seem to explain properly the phenomena. Firstly, the drag force increased linearly with the increase of x_{CM}, whereas the force exerted by the surface tension and the inertial force had a linear decay. On the other hand, x_{CM} was found to decrease over time due to the deformation of the droplet. The transient model as a function of the droplet height proved to be valid for height over 0.5mm, but the detachment height predictions did not agree with their own experimental results. The reason is that the drag coefficient used was that from a free spherical particle immersed in a fluid [20]. Therefore, an improvement on this coefficient would probably result in a more accurate model. Furthermore, the models developed by Kumbur et al. and Esposito et al. do not take into account the gravity force since they impose a force balance in the x direction.

An extension of the study done by Chen et al. [8] was done by Cho et al. [21]. That study focused on droplets that were initially spherical and their deformed shape was close to a sphere, so the average curvature could be approximated by the initial radius. The authors took the results of Chen et al. [8] as a starting point but they removed the hypothesis of the droplet constant shape. Therefore, the study showed different plots regarding the force components acting on the droplet, the droplet shape change and the detachment velocity. At low gas velocities, the viscous force proved to be dominant on small droplets whereas on large droplets the pressure force was dominant. On the other hand, the droplet deformation increased significantly when the droplet height was close to the channel height. The detachment velocity was analysed using a generalised equation for the drag coefficient C_{D} obtained with fitted data for the conditions of the study. As expected, the detachment velocity decayed with an increasing droplet diameter, and the relationship between the Weber and the Reynolds numbers found in reference [8] was corrected. Despite the characterization of the droplet deformation, the authors did not identified well the deformed shape of the droplet and the evolution of the contact line with the GDL surface, and the points b, e and g were not explained.

In addition to the analytical models above, researchers also studied droplet dynamics using numerical methods. A two-dimensional numerical simulation was developed by Zhu et al. [6] considering a straight channel of 250μm of height and 1000μm of length, with a micropore of width 50μm. The interface between the water droplet and the air was simulated using the Volume of Fluid (VOF) method [12], and the velocity of the two-phase mixture was modeled using the Navier-Stokes equation. The surface tension was modelled using the Continuum Surface Force (CSF, reference [22]) as a volumetric force in the momentum equation. The main target of the study was to observe the effects of the static contact angle, pore size and air and water inlet velocities on the water droplet dynamics, and to predict a critical velocity for the water removal. As a result, it could be seen that if the hydrophobicity of the GDL surface grew, the shear stress and the pressure forces dominated over the surface tension, thus promoting water removal and eventually detachment. Conversely, low hydrophobicity made the water droplet follow a film pattern due to surface tension. For hydrophobic surfaces, the advancing and receding angles evolved over time, whereas they remained constant if the surface was hydrophilic. Although that study took into account several variables that affected the behaviour of the droplet, it didn't considered a change in the channel geometry. The shortcomings of the work can be summarised with the points a and g from section 1.1. Some analytical models predicted that certain length-to-height ratio of the channel promoted water removal [8] and that should have been taken into account. Moreover, the contact angle of the droplet with the channel surface is a boundary condition, so it not well specified how is modelled the change of static contact angle into advancing and receding angles.

Considering the GDL surface completely hydrophobic, smaller pore size showed slower both droplet deformation and break-up processes. The effects of the air inlet velocity were pretty much intuitive: the forces that deformed and broke the water droplet, which were the pressure force and the shear stress, were directly related with the air inlet velocity. Results showed that for both low and high airflow velocities, water droplet formed a film flow. On the other hand, if the water injection velocity was lowered, the effects were negligible. However, for high injection velocities (3 ms^{-1} in a 50μl diameter pore) the water droplet blocked the channel almost instantly, and then it attached to the top wall (which was hydrophilic) and was dragged following a film pattern. Finally, the critical air velocity was found to be lower if the hydrophobicity was higher, as well as for larger dimensions of the droplet. In addition, the critical velocity had been predicted to be higher compared to other studies that considered the water droplet to be sitting in the bottom of the channel instead of emerging from it [3].

A three-dimensional numerical simulation was developed by the same authors [4], which was an extension of the previous work and it was closer to the actual case since more parameters were taken into account, namely water coverage ratio, critical diameter, friction factor and water saturation. The numerical model was the same and again it was combined with the VOF method, both adapted to three dimensions. Results showed similar results regarding the static contact angle of the GDL surface: water removal was achieved with a hydrophobic GDL surface. The three-dimensional simulations also revealed that with higher hydrophobicity the contact line of the droplet was shorter and the droplet growed higher. Moreover, it was stated that all the steps followed by the water droplet (i.e. emergence, growth, deformation, detachment and removal) were almost periodic, and the frequency of these processes increased with decreasing the wettability of the GDL [4]. It is important to remark that, despite the improvements from their previous work, they still couldn't solve points e, a and g.

The effects of the air inlet velocity were the same, adding the fact that the three-phase contact line deformed further downstream. The rest of the parameters decreased when the air velocity was higher. Earlier detachment of droplets and larger detachment diameter were observed when the water injection velocity was increased. Nevertheless, the detachment diameter and flow resistance coefficient remained constant for low injection velocities. Besides, for equivalent water volume, smaller pore size resulted in smaller detachment diameter. It is important to note that all numerical simulations done until the present day are based on the Volume of Fluid method [6] [4] [3] [2].

Although the previous numerical studies can track the evolution of the air-water interface, there are still many improvements to take into account. For instance, the GDL surface is not a homogeneous surface at all. It consists of small fibers one in top of each other with layers of Teflon randomly distributed over it (Figure 1.3). Thus, the surface of the GDL has roughness and it is chemically heterogeneous.

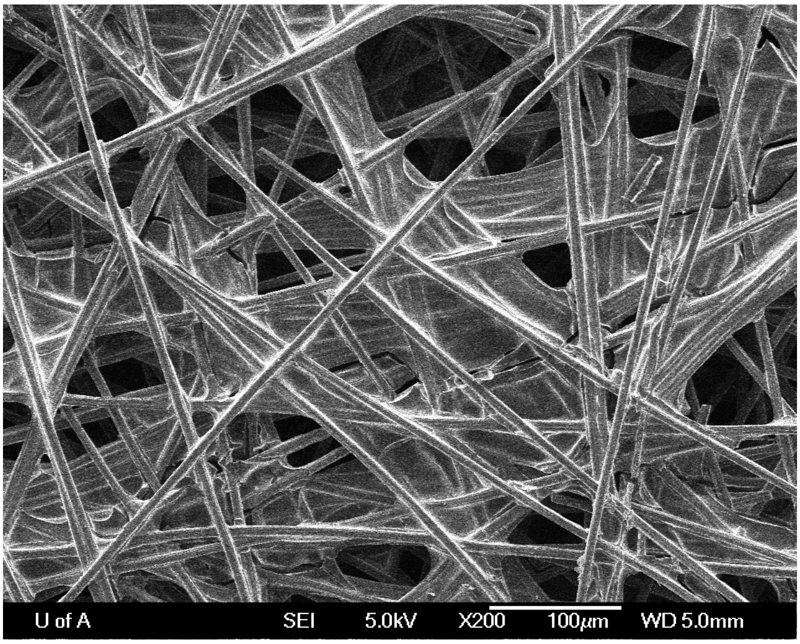

Figure 1.3: Microscale picture of the GDL surface covered with Teflon. Courtesy of Marc Secanell, ESDLab, University of Alberta

Since the channel affect the reactant transport to the MEA and MEA affects water production, it would be wise to design a computational domain that includes both MEA and channel. There is no agreement on the mechanism of emergence of the water from the GDL into the channel. Some authors believe that the generated water in the cathode side diffuses through the GDL with the shape of a tree [REF] whereas other authors state that the water diffuses with the shape of an inversed tree [REF]. These diffusion phenomena should be implemented in a CFD software together with the channel geometry in order to have an accurate model of the water area coverage, thus solving point d.

The mechanics of a single droplet emerging from a pore should be studied in more detail. Point e can be solved with a numerical simulation, and the result can be used in an analytical model, thus creating a semi-analytical model. This type of model would be easier to solve and couple to a MEA model and it would have the benefits of both the numerical and analytical analysis.

1.2.3 Experimental characterization

One of the main problems related with fuel cell experiments is that fuel cells are devices whose accessibility is very limited. Most of the experiments carried out to see the water droplet behavior inside a cathode flow channel are related with visualization using a transparent window [23] [24] [10] [9], neutron imaging [25] [26], IR-thermography [27] [28] and MRI [29]. The first option gives good optical access to the channel, enabling the caption of high resolution images. Nevertheless, the properties of this transparent window differ significantly from the rest of the bipolar plate walls. Recent studies use more advanced technology, such as high speed cameras [9] [30] [2], but the conclusions extracted regarding water droplet and film formation, and water removal are very similar to previous studies [23] [24] [10]. The results are consistent with the published numerical studies [3], [6], [4]. The rest of the aforementioned methods can obtain images of the fuel cell interior while it is operating, but usually the resolution of the results only allows to see the water distribution along the channel. Nonetheless, recent studies demonstrate an important improvement in image resolution [31].

The main conclusions extracted from the analytical and numerical studies are that water is easily removed from the channels with a hydrophobic GDL and relatively high airflow and water injection velocities. Zhang et al. [10] stated that for the experiments showed in their work, the airflow velocity threshold was 4 ms^{-1}. Under those conditions, water tended to attach to the channel walls and flow in film form. Besides, Zhan et al. [9] took into account the channel turns, concluding that velocities higher than 7 ms^{-1} for the air were enough to move the water through the turns. Another solution to remove the water from the channels was to increase the operation temperature since it lowered the surface tension of the water, but it led to the dehydratation of the membrane, thus lowering the fuel cell performance and efficiency. The ex-situ study developed by Colosqui et al. [30] suggested that the effects of gravity were important depending on the orientation of the channels. On the other hand, high resolution images had proven the appearance of small residual droplets from previous films that acted as nucleating agents for the droplet-to-film transition [30].

An experimental study was carried out by Theodorakakos et al. in order to study the water droplet dynamics inside the cathode microchannel. The set-up of the experiment showed the droplet behavior from a top-view, so it was easy to identify the shape and motion of the droplets. The results obtained suggesed that with the considered conditions, the flow pattern corresponded to a single droplet and no film flow was observed. On the other hand, the advancing and receding angles could not be directly measured, which was a drawback. Those angles were obtained in another experiment, where a water droplet was sitting on the bottom of a channel with an airflow circulating around it. It was important to remark that the forces acting on the water droplet were not the same in the case of a droplet emerging from a pore than a droplet sitting on a surface [3], [4]. The obtained angles were used in a numerical simulation based on the Volume of Fluid (VOF) method, and the results clearly showed the different dynamics of a droplet laying on a surface and another one emerging from a pore. The main drawback of this study was that the experiment was based on a droplet laying on a channel, and not emerging from it, hence its lack of accuracy regarding and actual fuel cell.

Carton et al. [2] ran an experiment as well to compare the observed phenomena with their numerical simulation. In their experiment a water droplet was placed in the channel; therefore, the effects of an emerging water droplet could not be recorded with enough accuracy. The results obtained were similar to previous studies, but the main difference was that the set-up of the experiment and the computational domain in the simulations was a double serpentine channel. If one of the channels was blocked due to slug flow formation, the other one had an increase in the velocity and pressure maximum values, which could damage the PEMFC membrane [2]. Moreover, water flooding affected directly the fuel cell voltage, keeping it constant.

Last but not least, two studies of the cathode channel geometry have been found in the literature [32], [33]. The results are focused towards the design of a channel that lowers the air pressure drop and promotes water removal, which is a good contribution to points c, d and g. Additionally, in [32] the authors identified the conditions that lead to water stagnation in the fuel channel turns, which is one of the critical factors in the fuel cell malfunction.

Literature shows that analytical models can still be improved. Although numerical simulations show accurate results regarding the shape evolution of the liquid phase inside the channel, the governing physics of the hysteresis angle remain without explanation. In addition, the drag coefficient should be characterized as well as the drag force since it is the responsible for droplet detachment and oscillation. A semi-analytical model that takes into account the drag coefficient computed numerically is considered the best option since it has a lower computational cost than the full numerical solution and it the physical phenomena described does not depend on surface reconstruction techniques used in the VOF method.

1.3 Contributions

This work is focused on developing an analytical model for a water droplet emerging from a pore. An analytical approach is used because it can be easily integrated with a MEA model. VOF methods unfortunately are computationally too expensive to be used in combination with a detailed MEA model such as Secanell et al. [34]. Based on the presented literature review, the model proposed by Esposito et al. is the most complete since it accounts for droplet deformations, advancing and receding angles and droplet oscillation. However, the model by Esposito et al. has three main drawbacks:

a) their expression for adhesion force is not accurate as discussed later in section 2.1.2.

b) their predictions for the drag force are innacurate as discussed in section 2.4.2.

c) the results for droplet frequency of oscillation were compared with a study that used different water injection conditions, so results cannot be compared.

The main contribution of this work is to develop an analytical model that is more complete and accurate than the previous analytical models in the literature [8], [7], [20] by introducing the following:

a) the adhesion force is obtained using the formula proposed by Antonini et al. [35] (equation (2.31) from section 2.1.2). This expression allows to account for any droplet geometry.

b) an expression for C_D based on CFD simulations of our droplet geometry.

c) an improved characterization of the droplet deformed geometry.

If the results found with the improved analytical model of the droplet prove to be better than the ones from the literature, it will represent a step forward toward a highly accurate analytical model. Moreover, the improved results will encourage the author to code a numerical solver for the problem and to perform several experiments to validate the results as well.

1.4 Structure of the Thesis

The present thesis is divided in four main parts. The first one is the Introduction, where the fuel cell is described in order to introduce the subject of the study and the motivation. A literature review about water droplet modelling is included, with focus on water droplet emerging from a pore in a PEM fuel cell cathode gas flow channel. The thesis contributions are also detailed.

The next chapter starts with a short description of the physical phenomena involved in the emergence of a droplet and describes the model of the droplet, which consists of a geometry model and a dynamic model. The former is a characterization of the droplet geometry from its static to its fully deformed shape, so the main geometric variables (the contact angles, the radius, the height) are characterized. The dynamic model uses the mentioned variables to simulate the droplet growth and deformation.

Chapter 3 presents the different results obtained from the simulations. The results describe the evolution of the contact angles during the growth of the droplet, as well as the position of the center of mass and the forces acting on it. Additionally, there is a study of the drag coefficient used in the air drag force model to prove that the results are significantly different from other similar studies.

Finally, the fourth chapter includes the conclusions extracted from the results, highlighting the most important findings that have been observed. The conclusions describe the contributions of the present work but identifies its drawbacks as well. Thus, the lacks of the present study are identified as future work.

Chapter 2

Droplet modelling

2.1 Introduction

The droplet model development and parametrization are explained in the current section. One has to bear in mind that, although the phenomena studied is a small droplet of a few microliters of volume, its behaviour depends on many factors. The hydrophobicity of the surface where it is laying on is the main variable that determines its shape [15]. If the air or another fluid that surrounds the droplet starts flowing, pressure and viscous forces appear and deform the droplet [16], [17], [8], [6]. When the deformation process starts, the contact force of the droplet with the solid surface is unbalanced and it starts increasing and deforming the contact line in order to recover the force balance [15]. It is clear, then, that all these processes have to be taken into account during the droplet model development.

2.1.1 Physical phenomena

Prior to the characterization of the water droplet, all the physics involved in the growth, deformation and detachment must be described.

Contact angles

Regarding surface and interfacial energies, the first term that has to be defined is the work of adhesion. It is defined as the reversible work that needs to be done to separate two unit areas from contact to the infinity in the vacuum [36]. Depending on the separated media, it is refered as work of adhesion (W_{12}) when they are different or work of cohesion (W_{11}) when it is the same material. This magnitude is always positive since all media tend to attract each other in vaccuum.

The next variables are the surface energy and the surface tension. Both of them are defined as the free energy change (γ) when the surface area of a medium is increased by a unit area, which is equivalent to separating two half-unit areas from contact:

$$\gamma_1 = \frac{1}{2}W_{11} \tag{2.1}$$

When the media is solid, then γ_1 becomes γ_{S} and it is measured in J m^{-2}. Conversely, when the media is liquid, γ_1 becomes γ_{L} and it is measured in N m^{-1}. If one looks carefully at the units, they are dimensionally the same. Nonetheless, the previous values have been defined on the vacuum. If the process happens in air, they are lowered since the material absorbs vapour [36]. The surface tension value for liquid water in air at room temperature is equal to 72 mN m^{-1} [36], [8], [20], [4].

On the other hand, the interfacial energy (γ_{12}) is identified as the free energy change when the interfacial area of two immiscible fluids changes by a unit area:

$$\gamma_{12} = \frac{1}{2}W_{11} + \frac{1}{2}W_{22} - W_{12} = \gamma_1 + \gamma_2 - W_{12} > 0 \tag{2.2}$$

Note the positive condition, since if γ_{12} is negative it means that the area expands indefinitely or, in other words, both fluids are miscible and the interface dissolves, which is not the case of the present study. Equation (2.2) is also known as the Dupré equation, and it can be written in an alternative form. The interfacial energy is, indeed, the same as the one expended on separating two media 1 in medium 2 (W_{121}) or in reverse (W_{212}):

$$\gamma_{12} = \frac{1}{2}W_{121} = \frac{1}{2}W_{212} \tag{2.3}$$

If one considers a liquid-solid interface, equation (2.2) can be rewritten as follows:

$$\gamma_{12} = \gamma_{\mathrm{SL}} = \gamma_{\mathrm{S}} + \gamma_{\mathrm{L}} - W_{\mathrm{SL}} \tag{2.4}$$

Since the problem of a water droplet laying on a surface and surrounded by air involves three media, the third component must be added to the previous equations. The work of adhesion in a third medium is defined as the energy change on separating two media 1 and 2 in medium 3 and is given by:

$$W_{132} = W_{12} + W_{33} - W_{13} - W_{23} = \gamma_{13} + \gamma_{23} - \gamma_{12} \tag{2.5}$$

This magnitude can be either positive or negative. In the former case, the condition $\gamma_{13} + \gamma_{23} > \gamma_{12}$ is then fulfilled and it means that medium 2 will spread over medium 1. If it is negative, then medium 3 will displace medium 2, which will totally wet the surface of medium 1.

Before introducing the contact angle description, there is one final remark to make regarding adhesion energies and adhesion forces. If one wants to separate two surfaces involving the same change in energy, the required adhesion force depends on the path and on the duration of the process. As an example, let us consider a simple example where to surfaces of the same material are separated one from another in two different ways: normal direction (the whole surface at a time) or peeling. The energy needed in both cases is the same, but the required force is really different: the peeling process needs a force 8 orders of magnitude less than the planar separation [36].

Moving on to the contact angles, lets consider a spherical droplet in medium V that approaches and settles on the rigid flat surface S (Figure 2.1).

The interfacial energies between the three media can be related using the static contact angle as shown in Figure 2.1:

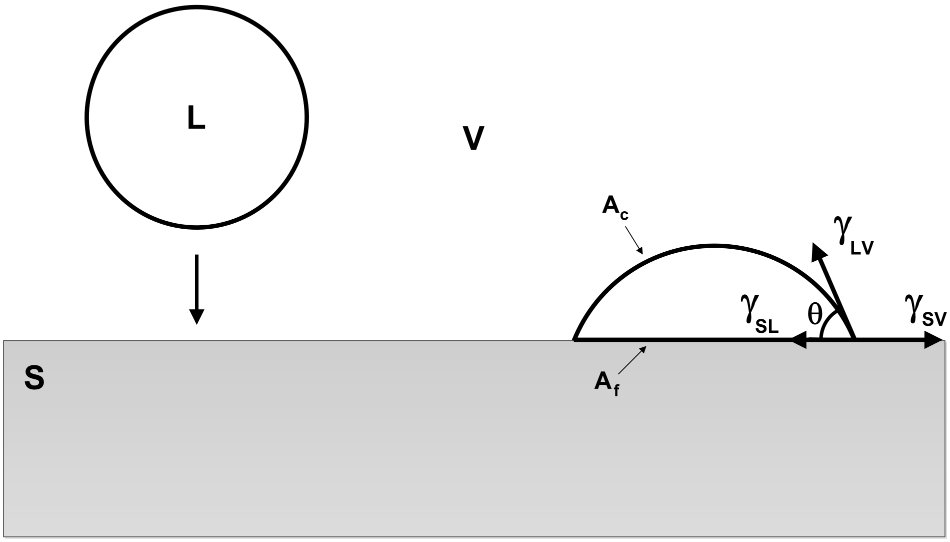

Figure 2.1: Settling of a liquid droplet on a solid surface

$$\gamma_{SV} - \gamma_{LV}\cos\theta - \gamma_{SL} = 0 \tag{2.6}$$

The deduction of this equation is done considering that the final total surface energy of the system is given by equation (2.7)

$$W_{\mathrm{TOT}} = \gamma_{LV}\left(A_{\mathrm{c}} + A_{\mathrm{f}}\right) - W_{\mathrm{SVL}}A_{\mathrm{f}} \tag{2.7}$$

where A_{f} is the flat area of the droplet and A_{c} is the curved area. At equilibrium, equation (2.7) becomes (2.8)

$$\gamma_{LV}\left(dA_{\mathrm{c}} + dA_{\mathrm{f}}\right) - W_{\mathrm{SVL}}dA_{\mathrm{f}} = 0 \tag{2.8}$$

The expression in equation (2.8) can be divided by dA_{f}, giving the following equation:

$$\gamma_{LV}\left(\frac{dA_{\mathrm{c}}}{dA_{\mathrm{f}}} + 1\right) - W_{\mathrm{SVL}} = 0 \tag{2.9}$$

The ratio $\frac{dA_{\mathrm{c}}}{dA_{\mathrm{f}}}$ equals $\cos\theta$ and if one does this substitution, equation (2.9) reads:

$$\gamma_{LV}\left(\cos\theta + 1\right) = W_{\mathrm{SVL}} = \gamma_{SV} + \gamma_{LV} - \gamma_{SL}$$

$$\gamma_{SL} + \gamma_{LV}\cos\theta = \gamma_{SV} \tag{2.10}$$

The deduction of the area ratio can be found in Appendix A. Further information regarding surface and interfacial forces can be found in Chapter 17 of [36]. The previous equations do not depend on the size of the droplet. However, when the curvature of the droplet is relatively high, the pressure inside it starts to be significant and it is known as Laplace pressure. The pressure difference between the liquid and the gas surrounding the droplet are related with the surface tension and the radius of curvature according to the Young-Laplace equation:

$$p_{\text{liq}} - p_{\text{gas}} = \frac{2\gamma}{R} \tag{2.11}$$

where p_{liq} is the pressure inside the droplet, p_{gas} is the pressure of the surrounding gas, γ is the surface tension and R is the droplet radius.

The surface tension forces acting on the interface of the droplet have been described so far. However, the present problem analyses a water placed within an airflow, which generates two additional forces. The first one is the pressure force and appears due to the pressure drop across the droplet [8], [21]. The other one is the viscous force that the air does when it flows around the droplet. Despite the fact that the mass of the droplet is extremely low, there is in fact an extra force, the gravitational force.

Non-dimensional analysis

In Fluid Mechanics, one can find several dimensionless numbers that represent a ratio between two different types of forces acting on a fluid. One of the most known numbers is the Reynolds number, which relates the inertial and the viscous forces:

$$Re = \frac{\rho u L}{\mu} \tag{2.12}$$

where ρ and μ are the fluid density and viscosity, respectively, u is the mean velocity and L is a characteristic length (the droplet height in the present study). When the problem analysed involves a droplet or a bubble of a certain fluid, it is common to use several dimensionless parameters that relate the aforementioned forces with the surface tension force. First, there is the Capillary number, which is the ratio between the viscous and the surface tension forces acting on the droplet:

$$Ca = \frac{\mu u}{\gamma} \tag{2.13}$$

where μ is the fluid viscosity (1.98×10^{-5} Pa s for the air at room temperature), u is the velocity (14.5 m s^{-1}) and γ is the surface tension between the two phases (0.072 N m^{-1} for liquid water in air). Using these values in the previous equation, it yields $\text{Ca} = 0.004 << 1$, which means that the viscous effects can be neglected compared with the surface tension forces. On the other hand, the Bond number expresses the ratio between gravitational forces and the surface tension:

$$Bo = \frac{\rho g d^2}{\gamma} \tag{2.14}$$

where ρ is the fluid density (1000 kg m^{-3} for liquid water at room temperature), g is the gravity acceleration and d is the droplet diameter. In this work, the maximum value of the diameter is 0.8 mm, and therefore the Bond number is 0.087, which means that surface tension forces are dominant over the gravitational forces. Depending on the country, the Bond number is also known as the Etvos number [21].

Finally, the ratio between the inertial forces and the surface tension is described by the Weber number:

$$We = \frac{\rho u^2 d}{\gamma} \tag{2.15}$$

Usually, for a micro gas channel the surface tension dominates over the rest. However, under the conditions of the present work, the Weber number is 2.8, which means that the inertial and the surface tension force effects are similar and none of them can be neglected with respect the other. In conclusion, surface tension and inertial forces are the most important forces acting on the value, and the rest will not be considered.

For a fuel cell channel, the air velocity is lower, approximately 0.15 m s $^{-1}$ (see section 2.4.4). Under these conditions, and considering the same parameters than before, the values of the Capillary and Weber numbers are 4.13×10^{-5} and 3×10^{-4}, respectively. Thus, the surface tension effects are dominant over the rest of the forces in a fuel cell channel.

It must be said that the capillary and the Weber numbers are related by the Reynolds number:

$$We = Ca \cdot Re \tag{2.16}$$

There are still more parameters defined on the emergence of a droplet in a microchannel. As it has been said in Chapter 1, there are three types of flow patterns for water droplets. A parameter that indicates if the droplet is closer to a film flow or to a spherical droplet is the water coverage ratio (A_w), which is defined as the ratio between water coverage area and GDL area in the channel. It is expected that the higher the hydrophobicity of the GDL, the lower the water coverage ratio [4]. The same relationship is found with the critical diameter (D_p), which is the diameter of the detached sphere divided by the length of the microchannel. On the other hand, the friction factor (f) is an indicator of the channel blockage, and it is defined by the following formula:

$$f = \frac{\Delta P}{\frac{1}{2}\rho u_a^2 \left(\frac{L}{D_H}\right)} \tag{2.17}$$

where ΔP is the pressure drop in the channel, u_a and ρ are the inlet velocity and density of the air, respectively, and L and D_H are the length and hydraulic diameter of the channel. As the droplet grows, f grows as well until the droplet detaches, which means a sudden drop of f. The water saturation (S_w) is another parameter that follows a similar pattern, and it has been defined as the ratio of water volume into the microchannel to the volume of the channel. In addition, the water saturation is lower for more hydrophobic surfaces [4].

2.1.2 Surface tension force modeling

In the previous section, the surface tension force has been described but an explicit equation has not been provided yet. When a droplet emerges from a pore in an airflow stream, the surface tension acts as the adhesion force since the air drag force tends to detach it from the surface. In 1995, Extrand and Kumagai [15] derived an analytical expression for the adhesion force:

$$F = \int_0^{2\pi} \gamma \cos\theta \cdot \cos\phi \zeta d\phi \tag{2.18}$$

where γ is the surface tension between both fluids, θ is the contact angle with the surface, ϕ is the azimuthal angle and ζ is the equivalent radius (Figure 2.2).

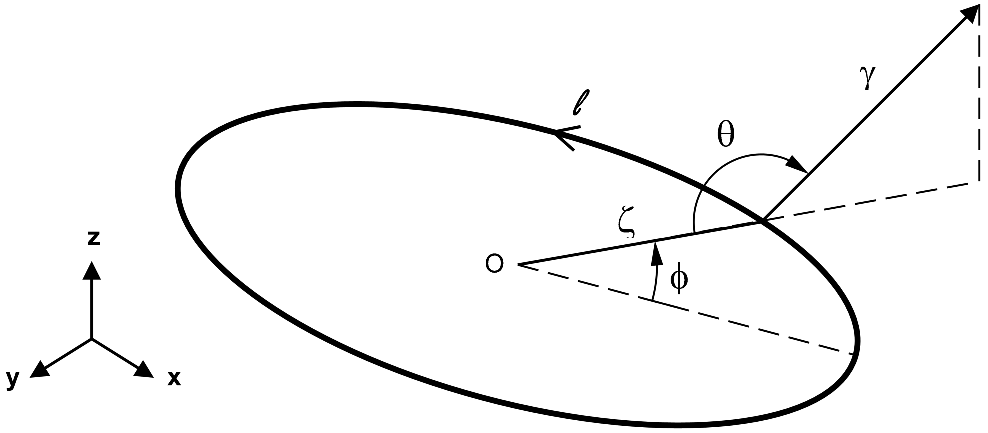

Figure 2.2: Variables used for the adhesion force computation

This expression was valid for droplets with circular shaped contact lines. Note that the integration is done along the contact line and not the whole contact area. They described this force as a retentive force, which was a critical value that indicated that the droplet was no more static and began to move. Two simplified versions of equation (2.18) were provided, one for circular drops and another for parallel-sided or elliptical contact lines:

$$\frac{F}{\gamma R} = k \left(\cos\left(\theta_R\right) - \cos\left(\theta_A\right)\right) \tag{2.19}$$

$$\frac{F}{\gamma w} = k \left(\cos\left(\theta_R\right) - \cos\left(\theta_A\right)\right) \tag{2.20}$$

where R is the radius, w is the droplet width and k is a constant that depends on the shape of the drop. Since the retentive force proved to increase with the drop size, they defined the reduced retentive force, which is presented as equations (2.19) and (2.20). Previous studies showed that the constant k was equal to $\frac{4}{\pi}$ by analytical calculation in [37] or $\frac{\pi}{2}$ from FEM.

In reference [37], the contact line was considered to be circular. Therefore, taking a look at Figure 2.2, the equivalent radius ζ is constant and equal to R, and equation (2.18) becomes:

$$F = \int_0^{2\pi} \gamma \cos\theta \cdot \cos\phi R d\phi \tag{2.21}$$

For a static droplet, the contact angle around the contact line remains constant. Nonetheless, if the droplet is distorted, the term $\cos\theta$ becomes a function of ϕ. Extrand and Gent [37] considered that $\cos\theta$ varied linearly around the perimeter between the receding angle value $\cos\theta_{\mathrm{R}}$ and the unperturbed value, according to equation (2.22).

$$\cos\theta = \frac{\phi}{\frac{\pi}{2}} \cdot \cos\theta_{\mathrm{A}} + \left(1 - \frac{\phi}{\frac{\pi}{2}}\right) \cdot \cos\theta_{\mathrm{R}} \tag{2.22}$$

The force could be computed as the result of two forces, one acting on the rear of the drop (F_{R}) and the other one acting toward the front (F_{A}). The rear force was computed taking into account equations (2.21) and (2.22), giving as a result equation (2.23):

$$F_{\mathrm{R}} = 2R\gamma\cos\theta_{\mathrm{A}} - \frac{4}{\pi}R\gamma\cos\theta_{\mathrm{A}} + \frac{4}{\pi}R\gamma\cos\theta_{\mathrm{R}} \tag{2.23}$$

The deduction of the precious formula can be found in Appendix B. The force acting on the front of the droplet was computed with equation (2.21) as well, but considering the contact angle to be constant and equal to θ_{A}. The resulting equation is equation (2.24).

$$F_{\mathrm{A}} = 2\int_0^{\frac{\pi}{2}} \gamma\cos\theta \cdot \cos\phi R d\phi = 2R\gamma\cos\theta_{\mathrm{A}} \int_0^{\frac{\pi}{2}} \cos\phi d\phi = 2R\gamma\cos\theta_{\mathrm{A}} \tag{2.24}$$

Finally, the net force acting on the droplet was computed as the difference between both front and rear forces, yielding equation (2.25).

$$F = F_{\mathrm{R}} - F_{\mathrm{A}} = 2R\gamma\cos\theta_{\mathrm{A}} - \frac{4}{\pi}R\gamma\cos\theta_{\mathrm{A}} + \frac{\pi}{4}R\gamma\cos\theta_{\mathrm{R}} - 2R\gamma\cos\theta_{\mathrm{A}}$$

$$F = \frac{4}{\pi}R\gamma\left(\cos\theta_{\mathrm{R}} - \cos\theta_{\mathrm{A}}\right) \tag{2.25}$$

On the other hand, Dussan and Chow [14] stated that $k = 2$ for parallel-sided drops. Extrand and Kumagai [15] found with their experiment that this constant increased with the droplet elongation, and they provided a more accurate expression for k:

$$k = 0.23 + 1.04\beta \tag{2.26}$$

where β is the ratio between droplet length and width. Celestini and Kofman [38] studied the fundamental vibration mode of a supported droplet, and they described the surface tension force as a restoring force associated with the deformation:

$$F = -\gamma\frac{\Delta S}{dx} = -\frac{\gamma S_0 h\left(\theta\right)}{R^2}dx \tag{2.27}$$

where S_0 is the surface of the droplet without deformation, R is the radius of the truncated sphere, dx is the displacement of the center of mass and $h\left(\theta\right)$ is a quadratic function depending on the static contact angle. This function was found for different contact angles using the Surface Evolver software, and it does not depend on the surface material [38]. However, in their work they did not specify if this function depends on the droplet size. Note that equation (2.27) can be thought of as a spring model equation since the force is linear with the displacement. Therefore, the eigenfrequency of the droplet was defined as follows:

$$\omega_0 = \sqrt{\frac{k_e}{m}} = \sqrt{\frac{k_e}{\rho V}} \tag{2.28}$$

where k_e is the effective spring constant:

$$k_e = -\frac{\gamma S_0 h\left(\theta\right)}{R^2} \tag{2.29}$$

Using the expressions for S_0 and the volume V for a truncated sphere, equation (2.28) reads:

$$\omega_0 = \sqrt{\frac{6\gamma h\left(\theta\right)}{\rho\left(1-\cos\theta\right)\left(2+\cos\theta\right)}} R^{-\frac{3}{2}} \tag{2.30}$$

The work of Antonini et al. [35] was a review of previous studies of the adhesion force characterization, and they proposed a new method for the evaluation of this magnitude. Among others, the previously presented works suposed specific geometries for the drop contact line (i.e. circular, elliptical, parallel-sided). However, in reference [35] a new method is proposed, considering a more general shape for the contact line. They highlighted that the equation for the adhesion force should be redifined. Whereas up to that date it was defined as:

$$\frac{F_{adh,max}}{\gamma R} = k\left(\cos\left(\theta_R\right) - \cos\left(\theta_A\right)\right) \tag{2.31}$$

Antonini et al. stated that the equation should be changed to:

$$\frac{F_{adh,max}}{\gamma R} = k\left(\cos\left(\theta_{\min}\right) - \cos\left(\theta_{\max}\right)\right) \tag{2.32}$$

since $\theta_{\min}$ and $\theta_{\max}$ do not necessarily coincide with θ_R and θ_A. Refering to previous work such as Extrand and Kumagai [15], they redefined the general expression for the adhesion force as well:

$$F_{adh} = F_x = \int_0^L \gamma_x dl = -\gamma \int_0^L \cos\theta\left(l\right)\cos\psi\left(l\right)dl \tag{2.33}$$

where $\psi\left(l\right)$ is a function describing the distribution of the normal to the contact line. Equation (2.33) could be alternatively written as:

$$F_{adh} = -\gamma \int_0^{2\pi} \cos\theta\left(\phi\right)\cos\psi\left(\phi\right)\sqrt{r^2 + \left(\frac{dr}{d\phi}\right)^2}d\phi \tag{2.34}$$

Using a novel techinque for droplet observation, they reconstructed the contact line shape from drop images and were able to compute the adhesion force with an error of less than 1%. As mentioned before, they characterized the contact line shape as a cosine Fourier series:

$$r\left(\phi\right) = \sum_{j=0}^{n-1} a_j \cos\left(j\phi\right) \tag{2.35}$$

where n is the number of coefficients a_j used in the series.

Milne and Amirfazli [39] used the formulation proposed in [35]. It is worth mentioning that the work from Antonini et al. was focused on drops resting on tilted planes, whereas [39] is focused on drop shedding by shear flow. Therefore, the contact line can be considered to have an elliptical shape, so the adhesion force is characterized with equation (2.32). The aim of their work was to find a critical value for the air velocity which lead to drop detachment from the surface.

Later on, Esposito et al. [20] based their characterization of the surface tension force on the work from Celestini and Kofman [38], taking equation (2.27) as a partial derivative:

$$F_{ST} = -\gamma \frac{\partial S}{\partial x_{\text{CM}}} \tag{2.36}$$

Since they developed a geometric model for the droplet, the surface was characterized as a function of the x-coordinate of the center of mass, resulting in an analytical expression for the surface tension force that was used to predict the droplet growth, deformation and detachment.

2.2 Governing equations

So far, the different forces acting on the water droplet have been described. The following model assumes that the gravity and viscous effects are negligible compared to the surface tension force, as it has been concluded in section 2.1.1. Thus, Figure 2.3 shows a schematic view of the studied problem.

The problem is as follows: a water droplet emerges from a pore into a channel with a constant volume flow Q, where the air flows with a fully developed velocity profile and an average velocity of u_{mean}. As the air flows around the droplet, it exerts a viscous force F_{drag} on the droplet surface, which tends to deform it. Since this force breaks the droplet equilibrium, the adhesion force acts on the opposite direction of the air drag, thus taking back the droplet to a new equilibrium state. It is easy to realize that this process of unbalance and balance of the droplet leads to the droplet oscillations. These issues will be discused further on. Note that the reference point for the coordinate system is located in the left contact point of the droplet (i.e. where the advancing angle is measured).

The equation that characterizes the balance of forces acting on the droplet is Newton's Second Law applied to the x-coordinate of the droplet center of mass:

$$m \frac{d^2 x_{\text{CM}}}{dt^2} = F_{\text{ST}} - F_{\text{drag}} \tag{2.37}$$

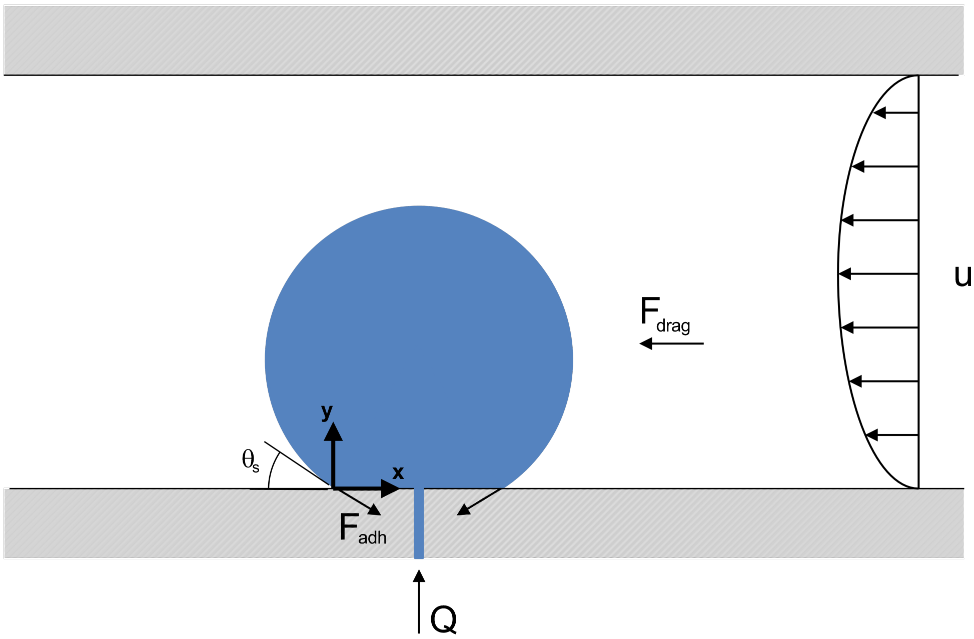

Figure 2.3: Droplet emerging on the GDL surface subjected to the drag and adhesion forces

where m is the mass of the droplet and is a function of time, x_{CM} is the center of mass x-coordinate and F_{ST} and F_{drag} are the adhesion and drag forces, respectively. These forces are described by the following equations:

$$F_{\mathrm{drag}} = \frac{1}{2}\rho_{\mathrm{air}} u_{\mathrm{air}}^{2} C_{\mathrm{D}} A \tag{2.38}$$

$$F_{\mathrm{ST}} = k\gamma t_{\mathrm{d}} \left(\cos\theta_{\mathrm{R}} - \cos\theta_{\mathrm{A}}\right) \tag{2.39}$$

where ρ_{air} is the air density, C_{D} is the drag coefficient and A is the frontal projected area of the droplet. The terms that form the equation of the adhesion force have been already explained in Section 2.1.2. In the following sections, the geometry and the dynamic models of the droplet will be explained, as well as the surface tension force model.

2.3 Droplet Geometry Model

The first step in the development of the droplet model is the full characterization of its geometry. The geometry model is based on the one developed by Esposito et al. [20] but with several corrections and improvements, which will be discussed in the following sections. The middle section of the deformed droplet is shown in Figure 2.4. It is important to note that point A is the reference for the coordinate system used in the whole study (Figure 2.3).

The main points and angles have been labeled in order to follow better the explanation of each formula found. The first task is to characterize every distance

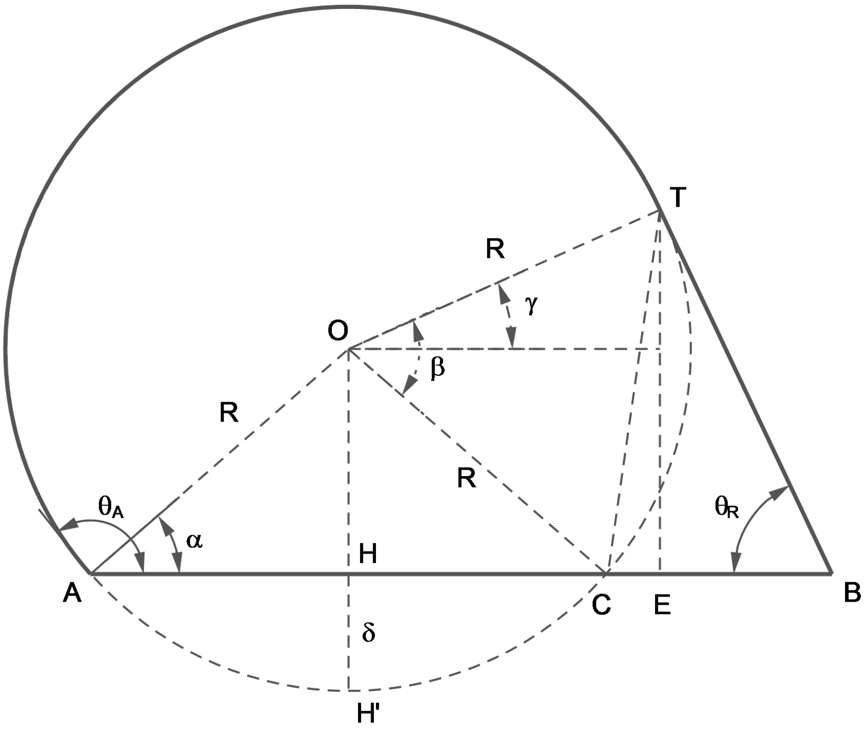

Figure 2.4: Deformed droplet geometry. Air flows from right to left

and angle, before finding the area of every sector in the droplet.

2.3.1 Angles and distances

According to Figure 2.4, the angle α is:

$$\theta_{\mathrm{A}} = \frac{\pi}{2} + \alpha \qquad \longrightarrow \qquad \alpha = \theta_{\mathrm{A}} - \frac{\pi}{2} \tag{2.40}$$

The first hypothesis used in the present model is that the segment $\bar{OT}$ is perpendicular to the segment $\bar{TB}$, hence the angle $\widehat{ETB}$ is equal to γ. Therefore:

$$\pi = \frac{\pi}{2} + \theta_{\mathrm{R}} + \gamma \qquad \longrightarrow \qquad \gamma = \frac{\pi}{2} - \theta_{\mathrm{R}} \tag{2.41}$$

The angle β can be found at point O, knowing that the angle $\widehat{HOC}$ is equal to $\frac{\pi}{2} - \alpha$:

$$\widehat{HOC} + (\beta - \gamma) = \frac{\pi}{2} \qquad \longrightarrow \qquad \frac{\pi}{2} - \alpha + \beta - \left(\frac{\pi}{2} - \theta_{\mathrm{R}}\right) = \frac{\pi}{2}$$

$$\frac{\pi}{2} - \left(\theta_{\mathrm{A}} - \frac{\pi}{2}\right) + \beta - \frac{\pi}{2} + \theta_{\mathrm{R}} = \frac{\pi}{2} \qquad \longrightarrow \qquad \frac{\pi}{2} - \theta_{\mathrm{A}} + \frac{\pi}{2} + \beta + \theta_{\mathrm{R}} = \pi \tag{2.42}$$

$$\beta = \theta_{\mathrm{A}} - \theta_{\mathrm{R}} \tag{2.43}$$

Once the angles have been characterized, the different distances are found. Distance $\bar{OH}$ can be found using:

$$\sin\alpha = \frac{\bar{OH}}{R} \qquad \longrightarrow \qquad \sin\left(\theta_{\mathrm{A}} - \frac{\pi}{2}\right) = \sin\theta_{\mathrm{A}}\cos\frac{\pi}{2} - \cos\theta_{\mathrm{A}}\sin\frac{\pi}{2} = -\cos\theta_{\mathrm{A}} = \frac{\bar{OH}}{R}$$

Therefore:

$$\bar{OH} = -R\cos\theta_{\mathrm{A}} \tag{2.44}$$

The distance δ can be found using the distance $\bar{OH}$:

$$R = \bar{OH} + \delta \qquad \longrightarrow \qquad \delta = R - \bar{OH} = R - (-R\cos\theta_{\mathrm{A}}) = R\left(1 + \cos\theta_{\mathrm{A}}\right) \tag{2.45}$$

$\bar{TC}$ is given by:

$$\frac{\bar{TC}}{2} = R\sin\frac{\beta}{2} \qquad \longrightarrow \qquad \bar{TC} = 2R\sin\frac{\beta}{2} \tag{2.46}$$

$\bar{AC}$ is obtained from geometrical arguments as:

$$\bar{AC} = 2\bar{AH} = 2R\cos\alpha = 2R\left(\cos\theta_{\mathrm{A}} - \frac{\pi}{2}\right) = 2R\left(\cos\theta_{\mathrm{A}}\cos\frac{\pi}{2} + \sin\theta_{\mathrm{A}}\sin\frac{\pi}{2}\right)$$

$$\bar{AC} = 2R\sin\theta_{\mathrm{A}} \tag{2.47}$$

Also, $\bar{CB}$ can be obtained using the the sine theorem applied in the triangle CTB. However, the angle $\widehat{CTB}$ has to be found first. In the triangle COT:

$$\beta + 2\widehat{OTC} = \pi \qquad \longrightarrow \qquad \widehat{OTC} = \frac{\pi}{2} - \frac{\beta}{2}$$

Knowing that the angle $\widehat{OTB}$ is equal to $\frac{\pi}{2}$:

$$\widehat{OTC} + \widehat{CTB} = \frac{\pi}{2} \qquad \longrightarrow \qquad \frac{\pi}{2} - \frac{\beta}{2} + \widehat{CTB} = \frac{\pi}{2}$$

Thus:

$$\widehat{CTB} = \frac{\beta}{2} \tag{2.48}$$

Applying the sine theorem in the triangle CTB:

$$\bar{CB} = \bar{TC}\frac{\sin\frac{\beta}{2}}{\sin\theta_{\mathrm{R}}} = 2R\frac{\sin^2\frac{\beta}{2}}{\sin\theta_{\mathrm{R}}} \tag{2.49}$$

Chord and height

The previous distances enable to find an expression for both the chord and the droplet height:

$$c = \bar{AC} + \bar{CB} = 2R\sin\theta_{\mathrm{A}} + 2R\frac{\sin^2\frac{\beta}{2}}{\sin\theta_{\mathrm{R}}} = 2R\left(\sin\theta_{\mathrm{A}} + \frac{\sin^2\frac{\beta}{2}}{\sin\theta_{\mathrm{R}}}\right)$$

However, this equation can be further simplified:

$$c = 2R\left(\sin\theta_{\mathrm{A}} + \frac{\sin^2\frac{\beta}{2}}{\sin\theta_{\mathrm{R}}}\right) = 2R\left(\sin\theta_{\mathrm{A}} + \frac{1-\cos\beta}{2\sin\theta_{\mathrm{R}}}\right) =$$

$$= R\left(2\sin\theta_{\mathrm{A}} + \frac{1-\cos\left(\theta_{\mathrm{A}}-\theta_{\mathrm{R}}\right)}{\sin\theta_{\mathrm{R}}}\right) =$$

$$= \frac{R}{\sin\theta_{\mathrm{R}}}\left(2\sin\theta_{\mathrm{A}}\sin\theta_{\mathrm{R}} + 1 - \left(\cos\theta_{\mathrm{A}}\cos\theta_{\mathrm{R}} + \sin\theta_{\mathrm{A}}\sin\theta_{\mathrm{R}}\right)\right) =$$

$$= \frac{R}{\sin\theta_{\mathrm{R}}}\left(2\sin\theta_{\mathrm{A}}\sin\theta_{\mathrm{R}} + 1 - \cos\theta_{\mathrm{A}}\cos\theta_{\mathrm{R}} - \sin\theta_{\mathrm{A}}\sin\theta_{\mathrm{R}}\right)$$

$$c = \frac{R}{\sin\theta_{\mathrm{R}}}\left(1 + \sin\theta_{\mathrm{A}}\sin\theta_{\mathrm{R}} - \cos\theta_{\mathrm{A}}\cos\theta_{\mathrm{R}}\right) \tag{2.50}$$

The droplet height can be easily found:

$$h = R + \bar{OH} = R - R\cos\theta_{\mathrm{A}} = R\left(1 - \cos\theta_{\mathrm{A}}\right) \tag{2.51}$$

The rest of the distances can be found using the previous relationships. Distance $\bar{TB}$ is found using again the sine theorem on the CTB triangle:

$$\frac{\bar{TB}}{\sin\widehat{TCB}} = \frac{\bar{TC}}{\sin\theta_{\mathrm{R}}} \qquad \longrightarrow \qquad \bar{TB} = \frac{2R\sin\frac{\beta}{2}}{\sin\theta_{\mathrm{R}}}\sin\widehat{TCB}$$

The angle $\widehat{TCB}$ equals to:

$$\widehat{TCB} + \theta_{\mathrm{R}} + \frac{\beta}{2} = \pi \qquad \longrightarrow \qquad \widehat{TCB} = \pi - \theta_{\mathrm{R}} - \frac{\beta}{2}$$

Then, the distance $\bar{TB}$ is:

$$\bar{TB} = \frac{2R\sin\frac{\beta}{2}}{\sin\theta_{\mathrm{R}}}\sin\left(\pi - \left(\theta_{\mathrm{R}} + \frac{\beta}{2}\right)\right) =$$

$$= \frac{2R\sin\frac{\beta}{2}}{\sin\theta_{\mathrm{R}}}\left(\sin\pi \cdot \cos\left(\theta_{\mathrm{R}} + \frac{\beta}{2}\right) - \cos\pi \cdot \sin\left(\theta_{\mathrm{R}} + \frac{\beta}{2}\right)\right)$$

$$\bar{TB} = \frac{2R\sin\frac{\beta}{2}}{\sin\theta_{\mathrm{R}}}\sin\left(\theta_{\mathrm{R}} + \frac{\beta}{2}\right) \tag{2.52}$$

Distance $\bar{TE}$ can be found using equation (2.52):

$$\sin\theta_\mathrm{R} = \frac{\bar{TE}}{\bar{TB}} \qquad \longrightarrow \qquad \bar{TE} = \bar{TB}\cdot\sin\theta_\mathrm{R} = \left(\frac{2R\sin\frac{\beta}{2}}{\sin\theta_\mathrm{R}}\sin\left(\theta_\mathrm{R}+\frac{\beta}{2}\right)\right)\sin\theta_\mathrm{R}$$

$$\bar{TE} = 2R\sin\left(\frac{\beta}{2}\right)\sin\left(\theta_\mathrm{R}+\frac{\beta}{2}\right) \tag{2.53}$$

Equivalently, the distance $\bar{EB}$ is equal to:

$$\cos\theta_\mathrm{R} = \frac{\bar{EB}}{\bar{TB}} \qquad \longrightarrow \qquad \bar{EB} = \bar{TB}\cdot\cos\theta_\mathrm{R} = \left(\frac{2R\sin\frac{\beta}{2}}{\sin\theta_\mathrm{R}}\sin\left(\theta_\mathrm{R}+\frac{\beta}{2}\right)\right)\cos\theta_\mathrm{R}$$

$$\bar{EB} = 2R\sin\left(\frac{\beta}{2}\right)\sin\left(\theta_\mathrm{R}+\frac{\beta}{2}\right)\mathrm{cotan}\theta_\mathrm{R} \tag{2.54}$$

It is important to note that this distance is negative for $\theta_\mathrm{R} > \frac{\pi}{2}$. The last distance to be characterized is $\bar{CE}$:

$$\bar{CE} = \bar{CB} - \bar{EB} = 2R\frac{\sin^2\frac{\beta}{2}}{\sin\theta_\mathrm{R}} - 2R\sin\left(\frac{\beta}{2}\right)\sin\left(\theta_\mathrm{R}+\frac{\beta}{2}\right)\mathrm{cotan}\theta_\mathrm{R}$$

$$\bar{CE} = 2R\frac{\sin\frac{\beta}{2}}{\sin\theta_\mathrm{R}}\left(\sin\frac{\beta}{2} - \sin\left(\theta_\mathrm{R}+\frac{\beta}{2}\right)\cos\theta_\mathrm{R}\right) \tag{2.55}$$

Perimeter

Once all the distances have been characterized, the perimeter is computed as follows:

$$P = \widehat{AT} + \bar{TB} = R\left(2\pi - \left(\beta + 2\left(\frac{\pi}{2}-\alpha\right)\right)\right) + \frac{2R\sin\frac{\beta}{2}}{\sin\theta_\mathrm{R}}\sin\left(\theta_\mathrm{R}+\frac{\beta}{2}\right)$$

The first term of the previous expression can be simplified:

$$2\pi - \left(\beta + 2\left(\frac{\pi}{2}-\alpha\right)\right) = 2\pi - \left(\theta_\mathrm{A} - \theta_\mathrm{R} + \pi - 2\left(\theta_\mathrm{A} - \frac{\pi}{2}\right)\right) =$$

$$= 2\pi - (\theta_\mathrm{A} - \theta_\mathrm{R} + \pi - 2\theta_\mathrm{A} + \pi) = 2\pi - (2\pi - \theta_\mathrm{A} - \theta_\mathrm{R}) = \theta_\mathrm{A} + \theta_\mathrm{R}$$

Therefore:

$$P = R\left(\theta_\mathrm{A} + \theta_\mathrm{R}\right) + \frac{2R\sin\frac{\beta}{2}}{\sin\theta_\mathrm{R}}\sin\left(\theta_\mathrm{R}+\frac{\beta}{2}\right) \tag{2.56}$$

2.3.2 Area

The area of the middle section of the droplet can be calculated as:

$$A = A_{\text{circ}} - A_{\widehat{AH'C}} - A_{\widehat{CT}} + A_{\text{CTB}} \tag{2.57}$$

The areas of the different sectors are found in the following sections. The area of the circle is:

$$A_{\text{circ}} = \pi R^2 \tag{2.58}$$

On the other hand, the area of the sector $A_{\widehat{AH'C}}$ is:

$$A_{\widehat{AH'C}} = \frac{R^2}{2}\left(2\left(\frac{\pi}{2}-\alpha\right) - \sin\left(2\left(\frac{\pi}{2}-\alpha\right)\right)\right) = \frac{R^2}{2}\left(\pi - 2\alpha - \sin\left(\pi - 2\alpha\right)\right) \tag{2.59}$$

This expression can be simplified knowing that:

$$\pi - 2\alpha = \pi - 2\left(\theta_{\text{A}} - \frac{\pi}{2}\right) = \pi - 2\theta_{\text{A}} + \pi = 2\pi - 2\theta_{\text{A}} \tag{2.60}$$

and

$$\sin\left(\pi - 2\alpha\right) = \sin\left(2\pi - 2\theta_{\text{A}}\right) = \sin 2\pi \cdot \cos 2\theta_{\text{A}} - \cos 2\pi \cdot \sin 2\theta_{\text{A}} = -\sin 2\theta_{\text{A}} \tag{2.61}$$

Using equations (2.60) and (2.61) in (2.59), it yields:

$$A_{\widehat{AH'C}} = \frac{R^2}{2}\left(2\pi - 2\theta_{\text{A}} + \sin 2\theta_{\text{A}}\right) \tag{2.62}$$

The area of $A_{\widehat{CT}}$ is characterized as follows:

$$A_{\widehat{CT}} = \frac{R^2}{2}\left(\beta - \sin\beta\right) \tag{2.63}$$

The area of the triangle CTB can be easily found since distances $\bar{C}B$ and $\bar{T}E$ are already known:

$$A_{\text{CTB}} = \frac{1}{2}\bar{C}B \cdot \bar{T}E = \frac{1}{2}\left(2R\frac{\sin^2\frac{\beta}{2}}{\sin\theta_{\text{R}}}\right)\left(2R\sin\left(\frac{\beta}{2}\right)\sin\left(\theta_{\text{R}} + \frac{\beta}{2}\right)\right)$$

$$A_{\text{CTB}} = \frac{2R^2}{\sin\theta_{\text{R}}}\sin^3\left(\frac{\beta}{2}\right) \cdot \sin\left(\theta_{\text{R}} + \frac{\beta}{2}\right) \tag{2.64}$$

Droplet area

Considering the equations for the different sections of the area, equation (2.57) becomes:

$$A = \pi R^2 - \frac{R^2}{2}\left(2\pi - 2\theta_{\text{A}} + \sin 2\theta_{\text{A}}\right) - \frac{R^2}{2}\left(\beta - \sin\beta\right) + \frac{2R^2}{\sin\theta_{\text{R}}}\sin^3\left(\frac{\beta}{2}\right) \cdot \sin\left(\theta_{\text{R}} + \frac{\beta}{2}\right) \tag{2.65}$$

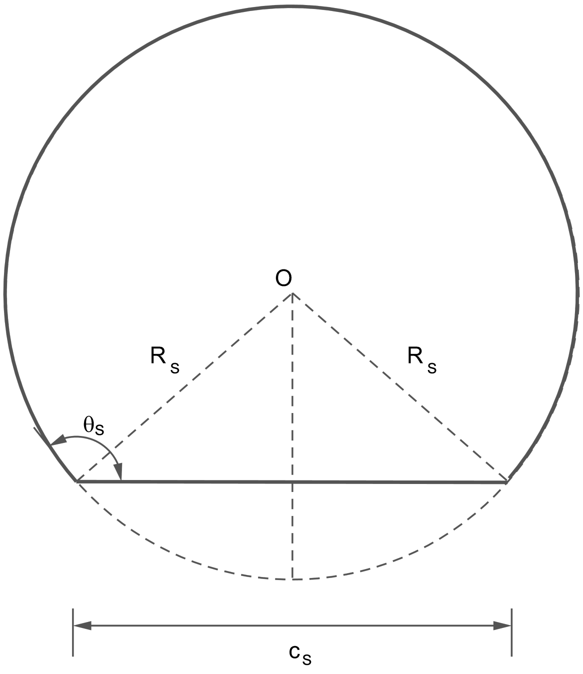

Figure 2.5: Static droplet geometry

This equation can be further simplified using the known expression for β and simplifying some terms:

$$A = \frac{R^2}{2}\left(\theta_{\mathrm{A}} + \theta_{\mathrm{R}} - \sin 2\theta_{\mathrm{A}} + \sin\left(\theta_{\mathrm{A}} - \theta_{\mathrm{R}}\right) + \frac{4\sin^3\left(\frac{\theta_{\mathrm{A}}-\theta_{\mathrm{R}}}{2}\right)\sin\left(\frac{\theta_{\mathrm{A}}+\theta_{\mathrm{R}}}{2}\right)}{\sin\theta_{\mathrm{R}}}\right) \tag{2.66}$$

Finally, the equation for the droplet area in any configuration yields:

$$\begin{aligned} A = \frac{R^2}{2\sin\theta_{\mathrm{R}}}\Big(&\left[\theta_{\mathrm{A}} + \theta_{\mathrm{R}} - \sin 2\theta_{\mathrm{A}} + \sin\left(\theta_{\mathrm{A}} - \theta_{\mathrm{R}}\right)\right]\sin\theta_{\mathrm{R}} + \\ &+ 4\sin^3\left(\frac{\theta_{\mathrm{A}} - \theta_{\mathrm{R}}}{2}\right)\sin\left(\frac{\theta_{\mathrm{A}} + \theta_{\mathrm{R}}}{2}\right)\Big) \end{aligned} \tag{2.67}$$

2.3.3 Equation to solve

With all the distances and areas defined, the relationship between the advancing and receding angles can be found. When there is no force acting on the droplet, it can be considered as static with the geometry in Figure 2.5.

The area of the static droplet is the following:

$$A_{\mathrm{S}} = R_{\mathrm{S}}^2\left(\theta_{\mathrm{S}} - \frac{\sin 2\theta_{\mathrm{S}}}{2}\right) \tag{2.68}$$

where the static radius R_{S} can be found using the following equation:

$$c_{\mathrm{S}} = 2R_{\mathrm{S}}\sin\theta_{\mathrm{S}} \longrightarrow R_{\mathrm{S}} = \frac{c_{\mathrm{S}}}{2\sin\theta_{\mathrm{S}}} \tag{2.69}$$

Therefore, the area of the static droplet can be written as follows:

$$A_{\mathrm{S}} = \left(\frac{c_{\mathrm{S}}}{2\sin\theta_{\mathrm{S}}}\right)^2 \left(\theta_{\mathrm{S}} - \frac{\sin 2\theta_{\mathrm{S}}}{2}\right) = \frac{c_{\mathrm{S}}^2}{4\sin^2\theta_{\mathrm{S}}} \left(\theta_{\mathrm{S}} - \frac{\sin 2\theta_{\mathrm{S}}}{2}\right) = \frac{c_{\mathrm{S}}^2}{4} \cdot K_3 \tag{2.70}$$

Using the hypothesis of small deformations, the area of the middle section of the droplet can be supposed constant. Therefore, using both equations (2.67) and (2.70):

$$\frac{c_{\mathrm{S}}^2}{4} \cdot K_3 =$$

$$= \frac{R^2}{2\sin\theta_{\mathrm{R}}} \left([\theta_{\mathrm{A}} + \theta_{\mathrm{R}} - \sin 2\theta_{\mathrm{A}} + \sin(\theta_{\mathrm{A}} - \theta_{\mathrm{R}})] \sin\theta_{\mathrm{R}} + 4\sin^3\left(\frac{\theta_{\mathrm{A}} - \theta_{\mathrm{R}}}{2}\right) \sin\left(\frac{\theta_{\mathrm{A}} + \theta_{\mathrm{R}}}{2}\right)\right) \tag{2.71}$$

The radius R can be substituted using the equation (2.50), and the previous equation yields:

$$\frac{c_{\mathrm{S}}^2}{4} \cdot K_3 =$$

$$= \frac{1}{2\sin\theta_{\mathrm{R}}} \left(\frac{c \cdot \sin\theta_{\mathrm{R}}}{(1 + \sin\theta_{\mathrm{A}}\sin\theta_{\mathrm{R}} - \cos\theta_{\mathrm{A}}\cos\theta_{\mathrm{R}})}\right)^2 (\theta_{\mathrm{A}} + \theta_{\mathrm{R}} - \sin 2\theta_{\mathrm{A}} + \sin(\theta_{\mathrm{A}} - \theta_{\mathrm{R}}) + \cdots) \tag{2.72}$$

The r.h.s. term can be further simplified and written in a more compact form:

$$\frac{c_{\mathrm{S}}^2}{4} \cdot K_3 = \frac{c^2 \cdot \sin\theta_{\mathrm{R}}}{2K_2^2} \cdot K_1 \tag{2.73}$$

From equation (2.73), it can be seen that both terms in each side have the chord squared. It has been observed in some experiments that the chord length doesn't chance from the static droplet to the deformed one [20]. Therefore, both chord terms can be cancelled, giving the following equation in compact form:

$$\frac{K_3}{4} = \frac{\sin\theta_{\mathrm{R}}}{2K_2^2} \cdot K_1 \qquad \longrightarrow \qquad K_2^2 \cdot K_3 - 2\sin\theta_{\mathrm{R}} \cdot K_1 = 0 \tag{2.74}$$

where:

$$K_1 = \left((\theta_{\mathrm{A}} + \theta_{\mathrm{R}} - \sin 2\theta_{\mathrm{A}} + \sin(\theta_{\mathrm{A}} - \theta_{\mathrm{R}})) \sin\theta_{\mathrm{R}} + 4\sin^3\left(\frac{\theta_{\mathrm{A}} - \theta_{\mathrm{R}}}{2}\right) \sin\left(\frac{\theta_{\mathrm{A}} + \theta_{\mathrm{R}}}{2}\right)\right) \tag{2.75}$$

$$K_2 = 1 + \sin\theta_{\mathrm{A}}\sin\theta_{\mathrm{R}} - \cos\theta_{\mathrm{A}}\cos\theta_{\mathrm{R}} \tag{2.76}$$

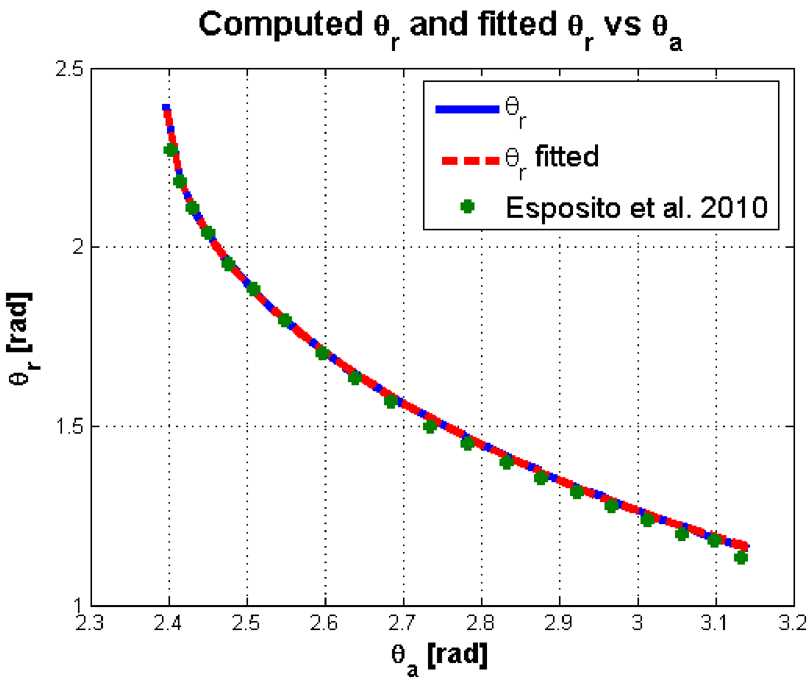

Figure 2.6: Computed θ_{R} versus fitted θ_{R}

$$K_3 = \frac{1}{\sin^2\theta_{\mathrm{S}}}\left(\theta_{\mathrm{S}} - \frac{\sin 2\theta_{\mathrm{S}}}{2}\right) \tag{2.77}$$

Equation (2.74) is solved in MATLAB for θ_{R}, and in each step a different value of θ_{A} is given, varying from θ_{S} to π. It is very important to note that the only two variables in this equation are the angles, which means that their relationship is the same regardless the size of the droplet. The result can be plotted in order to find a relationship between the advancing and receding angles.

Since it is impossible to find an explicit equation for the receding angle, a fitting function needs to be found in order to have an expression for this magnitude. Figure 2.6 shows the computed values for the receding angle and a fitting curve, compared to the fitting curve found by the study of Esposito et al. [20]. From the yielding plot, one can observe two clearly different parts: from $\theta_{\mathrm{A}} = 2.39$ to 2.43 rad, the receding angle drops quickly, whereas from 2.43 to π θ_{R} decreases almost linearly. Therefore, two different equations are proposed for the two parts of the curve. Using the free software CurveFit, the best curve for both cases is:

$$\theta_{\mathrm{R}} = \frac{a + b\theta_{\mathrm{A}}}{1 + c\theta_{\mathrm{A}} + d\theta_{\mathrm{A}}^2} \tag{2.78}$$

where the constants a, b, c and d have the values shown in Table 2.1.

In both cases, the Coefficient of Determination R^2 is higher than 0.999, which means that the proposed functions have an excellent fit with the numerical data.

θ_{A}	a	b	c	d
[2.39, 2.43)	-0.5771	0.2414	-0.9432	0.2195
[2.43, π]	-1.5154	0.6500	-1.1679	0.3164

Table 2.1: Constants used in the fitting curve of the advancing and receding angles relationship

2.3.4 Center of Mass

In this section, the expressions for both coordinates of the droplet center of mass are developed.

Circle

The center of mass coordinates are the same than the point O:

$$x_{\mathrm{circ}} = R\mathrm{sin}\theta_{\mathrm{A}} \tag{2.79}$$

$$y_{\mathrm{circ}} = -R\mathrm{cos}\theta_{\mathrm{A}} \tag{2.80}$$

The center of mass x-coordinate of the sector $\widehat{AHC}$ is the same than the circle:

$$x_{\widehat{AHC}} = \bar{A}H = R\mathrm{sin}\theta_{\mathrm{A}} \tag{2.81}$$

On the other hand, the y-coordinate has to be computed using some known relationships. For a circular sector as the one shown on the following Figure 2.7, the x-coordinate of the center of mass is:

$$x_{\widehat{AHCO}} = \frac{2R\mathrm{sin}\alpha_2}{3\alpha_2} \tag{2.82}$$

Since the geometry is symmetric with respect the x axis, the y-coordinate of the center of mass is 0. Thus, the center of mass of the sector AH'C can be computed as the difference between the circular sector AH'CO and the triangle ACO:

$$x_{\widehat{AHC}} = \frac{x_{\widehat{AHCO}}A_{\widehat{AHCO}} - x_{\mathrm{ACO}}A_{\mathrm{ACO}}}{A_{\mathrm{AHC}}} \tag{2.83}$$

where

$$A_{\widehat{AHCO}} = \frac{1}{2}R^2 2\alpha_2 = R^2\alpha_2 \tag{2.84}$$

$$x_{\mathrm{ACO}} = \frac{2R\mathrm{cos}\alpha_2}{3} \tag{2.85}$$

$$A_{\mathrm{ACO}} = 2\cdot\frac{1}{2}R\mathrm{sin}\alpha_2 R\mathrm{cos}\alpha_2 = R^2\mathrm{sin}\alpha_2\mathrm{cos}\alpha_2 = R^2\frac{\mathrm{sin}2\alpha_2}{2} \tag{2.86}$$

$$A_{\mathrm{AHC}} = A_{\widehat{AHCO}} - A_{\mathrm{ACO}} = R^2\alpha_2 - R^2\frac{\mathrm{sin}2\alpha_2}{2} \tag{2.87}$$

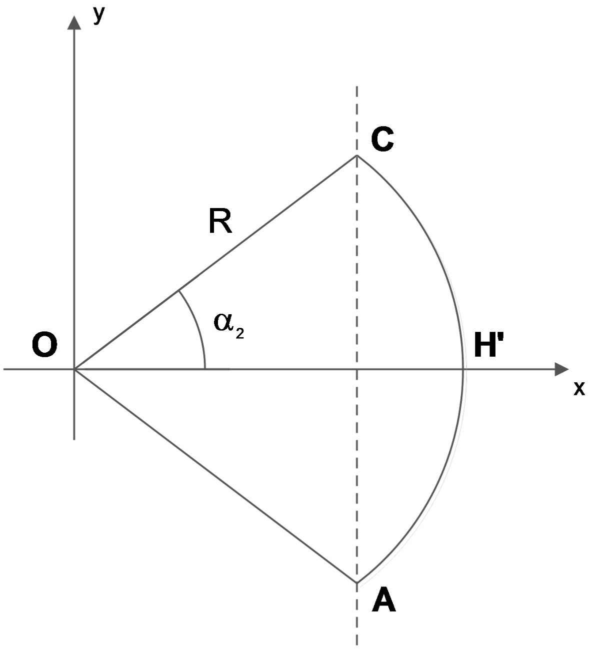

Figure 2.7: Center of mass of a circular sector

Therefore, equation (2.83) becomes:

$$x_{\widehat{AHC}} = \frac{\frac{2R\sin\alpha_2}{3\alpha_2}R^2\alpha_2 - \frac{2R\cos\alpha_2}{3}R^2\frac{\sin2\alpha_2}{2}}{R^2\alpha_2 - R^2\frac{\sin2\alpha_2}{2}} \tag{2.88}$$

Simplifying terms, the previous expression yields:

$$x_{\widehat{AHC}} = \frac{\frac{2R\sin\alpha_2}{3}\left(1-\cos^2\alpha_2\right)}{\alpha_2 - \frac{\sin2\alpha_2}{2}} = \frac{\frac{2R\sin\alpha_2}{3}\left(\sin^2\alpha_2\right)}{\alpha_2 - \frac{\sin2\alpha_2}{2}} = \frac{\frac{2R\sin^3\alpha_2}{3}}{\alpha_2 - \frac{\sin2\alpha_2}{2}} \tag{2.89}$$

In this case, the angle α_2 is:

$$\alpha_2 = \frac{\pi}{2} - \alpha = \frac{\pi}{2} - \left(\theta_{\mathrm{A}} - \frac{\pi}{2}\right) = \pi - \theta_{\mathrm{A}} \tag{2.90}$$

The expressions with the sine of α_2 can be simplified:

$$\sin\alpha_2 = \sin\left(\pi - \theta_{\mathrm{A}}\right) = \sin\pi \cdot \cos\theta_{\mathrm{A}} - \cos\pi \cdot \sin\theta_{\mathrm{A}} = \sin\theta_{\mathrm{A}} \tag{2.91}$$

$$\sin2\alpha_2 = \sin\left(2\pi - 2\theta_{\mathrm{A}}\right) = \sin2\pi \cdot \cos2\theta_{\mathrm{A}} - \cos2\pi \cdot \sin2\theta_{\mathrm{A}} = \sin2\theta_{\mathrm{A}} \tag{2.92}$$

Then, equation (2.89) becomes:

$$x_{\widehat{AHC}} = \frac{\frac{2}{3}R\sin^3\theta_{\mathrm{A}}}{\left(\pi - \theta_{\mathrm{A}}\right) + \frac{\sin2\theta_{\mathrm{A}}}{2}} \tag{2.93}$$

However, this expression is based on the system of coordinates shown in Figure 2.7. The coordinates in the global system of coordinates are:

$$y_{\widehat{AHC}} = -\frac{\frac{2}{3}R\sin^3\theta_\mathrm{A}}{(\pi - \theta_\mathrm{A}) + \frac{\sin 2\theta_\mathrm{A}}{2}} + R\sin\alpha = -\frac{\frac{2}{3}R\sin^3\theta_\mathrm{A}}{(\pi - \theta_\mathrm{A}) + \frac{\sin 2\theta_\mathrm{A}}{2}} - R\cos\theta_\mathrm{A} \tag{2.94}$$

Both equations (2.81) and (2.94) give an expression for the $\widehat{AHC}$ center of mass.

The equations used for $\widehat{CT}$ sector are the same than the ones for the $\widehat{AHC}$ sector, but this one is rotated with an angle α_3 (Figure 2.8). Using the relationships in the previous section, but substituting the angle α_2 by $\frac{\beta}{2}$:

$$x_{\widehat{CT}} = \frac{\frac{2}{3}R\sin^3\frac{\beta}{2}}{\frac{\beta}{2} - \frac{\sin 2\frac{\beta}{2}}{2}} \tag{2.95}$$

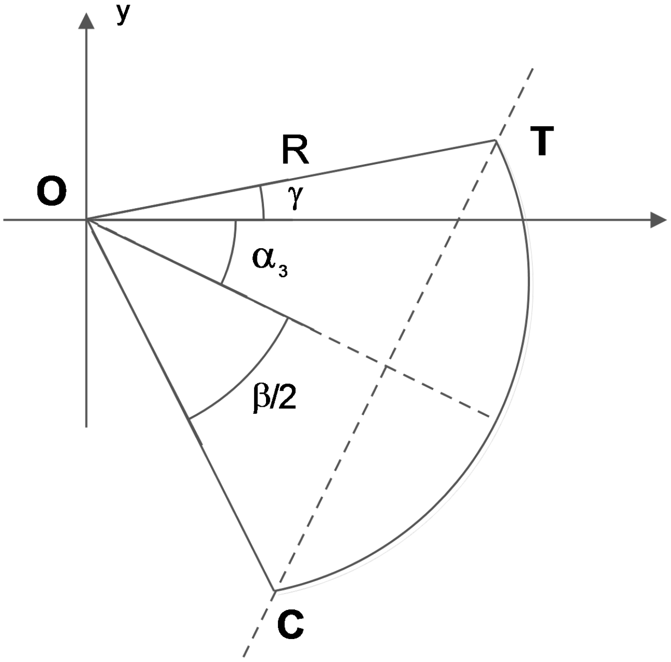

Figure 2.8: Center of mass of the sector CT

This expression is for the sector before the rotation. The global coordinates of the center of mass can be found with the projection of this distance using the angle α_3:

$$x_{\widehat{CT}} = \left(\frac{\frac{2}{3}R\sin^3\frac{\beta}{2}}{\frac{\beta}{2} - \frac{\sin 2\frac{\beta}{2}}{2}}\right) \cdot \cos\alpha_3 \tag{2.96}$$

$$y_{\widehat{CT}} = -\left(\frac{\frac{2}{3}R\sin^3\frac{\beta}{2}}{\frac{\beta}{2} - \frac{\sin 2\frac{\beta}{2}}{2}}\right) \cdot \sin\alpha_3 \tag{2.97}$$

Taking into account the coordinates of the point O in the global coordinates, the final expressions yield:

$$x_{\widehat{CT}} = R\sin\theta_{\mathrm{A}} + \left(\frac{\frac{2}{3}R\sin^3\frac{\beta}{2}}{\frac{\beta}{2} - \frac{\sin\beta}{2}} \right) \cdot \cos\alpha_3 \tag{2.98}$$

$$y_{\widehat{CT}} = -R\cos\theta_{\mathrm{A}} - \left(\frac{\frac{2}{3}R\sin^3\frac{\beta}{2}}{\frac{\beta}{2} - \frac{\sin\beta}{2}} \right) \cdot \sin\alpha_3 \tag{2.99}$$

The angle α_3 can be easily computed as:

$$\frac{\beta}{2} + \alpha_3 + \gamma = \beta \qquad \longrightarrow \qquad \alpha_3 = \frac{\beta}{2} - \gamma \tag{2.100}$$

Using both relationships expressed in (2.43) and (2.41), the previous expression yields:

$$\alpha_3 = \frac{\theta_{\mathrm{A}} - \theta_{\mathrm{R}}}{2} - \left(\frac{\pi}{2} - \theta_{\mathrm{R}}\right) = \frac{\theta_{\mathrm{A}}}{2} - \frac{\theta_{\mathrm{R}}}{2} - \frac{\pi}{2} + \theta_{\mathrm{R}} = \frac{\theta_{\mathrm{A}} + \theta_{\mathrm{R}}}{2} - \frac{\pi}{2} \tag{2.101}$$

The sine and cosine of α_3 yield:

$$\sin\alpha_3 = \sin\left(\frac{\theta_{\mathrm{A}} + \theta_{\mathrm{R}}}{2} - \frac{\pi}{2}\right) = \sin\frac{\theta_{\mathrm{A}} + \theta_{\mathrm{R}}}{2} \cdot \cos\frac{\pi}{2} - \cos\frac{\theta_{\mathrm{A}} + \theta_{\mathrm{R}}}{2} \cdot \sin\frac{\pi}{2} = -\cos\frac{\theta_{\mathrm{A}} + \theta_{\mathrm{R}}}{2} \tag{2.102}$$

$$\cos\alpha_3 = \cos\left(\frac{\theta_{\mathrm{A}} + \theta_{\mathrm{R}}}{2} - \frac{\pi}{2}\right) = \cos\frac{\theta_{\mathrm{A}} + \theta_{\mathrm{R}}}{2} \cdot \cos\frac{\pi}{2} + \sin\frac{\theta_{\mathrm{A}} + \theta_{\mathrm{R}}}{2} \cdot \sin\frac{\pi}{2} = \sin\frac{\theta_{\mathrm{A}} + \theta_{\mathrm{R}}}{2} \tag{2.103}$$

Finally, the expressions (2.98) and (2.99) yield:

$$x_{\widehat{CT}} = R\sin\theta_{\mathrm{A}} + \left(\frac{\frac{2}{3}R\sin^3\frac{\beta}{2}}{\frac{\beta}{2} - \frac{\sin\beta}{2}} \right) \cdot \sin\frac{\theta_{\mathrm{A}} + \theta_{\mathrm{R}}}{2} \tag{2.104}$$

$$y_{\widehat{CT}} = -R\cos\theta_{\mathrm{A}} + \left(\frac{\frac{2}{3}R\sin^3\frac{\beta}{2}}{\frac{\beta}{2} - \frac{\sin\beta}{2}} \right) \cdot \cos\frac{\theta_{\mathrm{A}} + \theta_{\mathrm{R}}}{2} \tag{2.105}$$

The center of mass of CTE triangle can be easily found with the following relationships:

$$x_{CTE} = \bar{A}C + \frac{2}{3}\bar{C}E = 2R\sin\theta_{\mathrm{A}} + \frac{2}{3}\left(2R\frac{\sin\frac{\beta}{2}}{\sin\theta_{\mathrm{R}}}\left(\sin\frac{\beta}{2} - \sin\left(\theta_{\mathrm{R}} + \frac{\beta}{2}\right)\cos\theta_{\mathrm{R}}\right)\right) \tag{2.106}$$

$$y_{CTE} = \frac{1}{3}\bar{T}E = \frac{2R}{3}\sin\left(\frac{\beta}{2}\right)\sin\left(\theta_{\mathrm{R}} + \frac{\beta}{2}\right) \tag{2.107}$$

The center of mass of ETB triangle depends on the value of θ_{R} since, according to equation (2.54), the distance $\bar{EB}$ is negative or positive for certain values of the receding angle. Therefore, the area of this triangle becomes negative when $\theta_{\mathrm{R}} > \frac{\pi}{2}$, whereas it is positive when $\theta_{\mathrm{R}} < \frac{\pi}{2}$ as shown in Figure 2.9. Notice that the area is exactly 0 when $\theta_{\mathrm{R}} = \frac{\pi}{2}$.

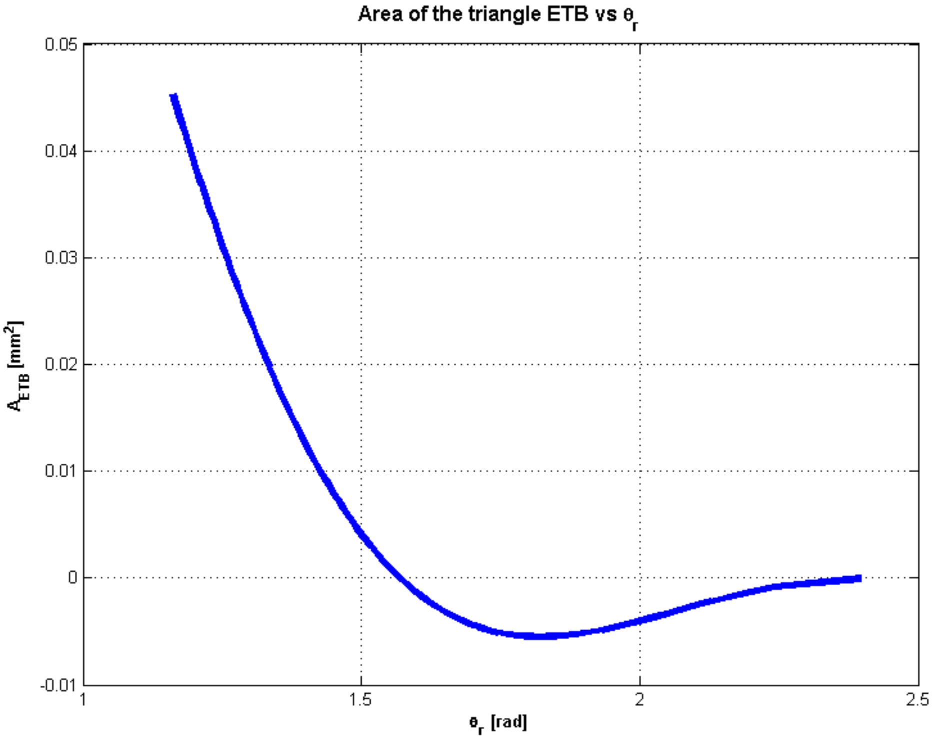

Figure 2.9: Area of the ETB triangle depending on θ_{R}

Due to the change in the sign, two possible situations are studied depending on the value of the receding angle in order to see if there is any difference in the computation.

Figure 2.10 shows the shape of triangle ETB when $\theta_{\mathrm{R}} > \frac{\pi}{2}$. Therefore, the x coordinate of the center of mass can be computed as follows:

$$x_{ETB} = \bar{AC} + \bar{CB} + \frac{2}{3}\bar{EB} =$$

$$= 2R\sin\theta_{\mathrm{A}} + 2R\frac{\sin^2\frac{\beta}{2}}{\sin\theta_{\mathrm{R}}} + \left|\frac{4}{3}R\sin\left(\frac{\beta}{2}\right)\sin\left(\theta_{\mathrm{R}} + \frac{\beta}{2}\right)\mathrm{cotan}\theta_{\mathrm{R}}\right| \tag{2.108}$$

On the other hand, when $\theta_{\mathrm{R}} < \frac{\pi}{2}$ as shown in Figure 2.11, the x coordinate of the center of mass can be computed as follows:

$$x_{ETB} = \bar{AC} + \bar{CE} + \frac{1}{3}\bar{EB} = \bar{AC} + \bar{CB} - \bar{EB} + \frac{1}{3}\bar{EB} = \bar{AC} + \bar{CB} - \frac{2}{3}\bar{EB}$$

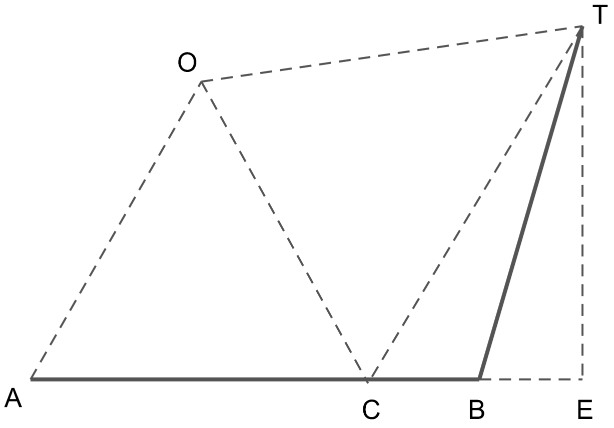

Figure 2.10: Triangle ETB for values of $\theta_{\mathrm{R}} > \frac{\pi}{2}$

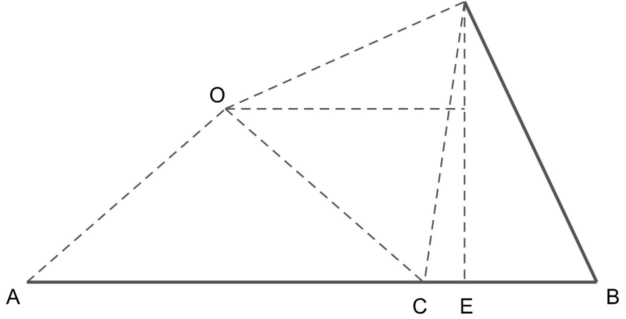

Figure 2.11: Triangle ETB for values of $\theta_{\mathrm{R}} < \frac{\pi}{2}$

$$= 2R\mathrm{sin}\theta_\mathrm{A} + 2R\frac{\mathrm{sin}^2\frac{\beta}{2}}{\mathrm{sin}\theta_\mathrm{R}} - \frac{4}{3}R\mathrm{sin}\left(\frac{\beta}{2}\right)\mathrm{sin}\left(\theta_\mathrm{R} + \frac{\beta}{2}\right)\mathrm{cotan}\theta_\mathrm{R} \tag{2.109}$$

$$y_{ETB} = \frac{1}{3}\bar{TE} = \frac{2R}{3}\mathrm{sin}\frac{\beta}{2}\mathrm{sin}\left(\theta_\mathrm{R} + \frac{\beta}{2}\right) \tag{2.110}$$

Looking at equations (2.108) and (2.109) it can be concluded that the same equation works for any value of the receding angle. It is important to note that this result does not agree with the one shown by Esposito et al. [20]. The results found in that study state that there is indeed a difference on the x_{ETB} equation depending on the value of θ_R. When $\theta_\mathrm{R} > \frac{\pi}{2}$, the equation is the same that equation (2.108):

$$x_{ETB} = 2R\mathrm{sin}\theta_\mathrm{A} + 2R\frac{\mathrm{sin}^2\frac{\beta}{2}}{\mathrm{sin}\theta_\mathrm{R}} - \frac{4}{3}R\mathrm{sin}\left(\frac{\beta}{2}\right)\mathrm{sin}\left(\theta_\mathrm{R} + \frac{\beta}{2}\right)\mathrm{cotan}\theta_\mathrm{R}$$

Nonetheless, the equation for $\theta_\mathrm{R} < \frac{\pi}{2}$ is the following:

$$x_{ETB} = 2R\mathrm{sin}\theta_\mathrm{A} + 2R\frac{\mathrm{sin}^2\frac{\beta}{2}}{\mathrm{sin}\theta_\mathrm{R}} + \frac{2}{3}R\mathrm{sin}\left(\frac{\beta}{2}\right)\mathrm{sin}\left(\theta_\mathrm{R} + \frac{\beta}{2}\right)\mathrm{cotan}\theta_\mathrm{R}$$

The easiest way to see which formula makes sense is to plot both equations in the same chart. Figure 2.12 shows the difference between the previous expressions. Before reaching any conclusion, it is worth mentioning that the plot has been obtained using a droplet of a fixed chord, in this case 0.5mm. Therefore, according to Esposito et al., the center of mass x-coordinate of the ETB triangle is always greater than the chordThis result is not physical.

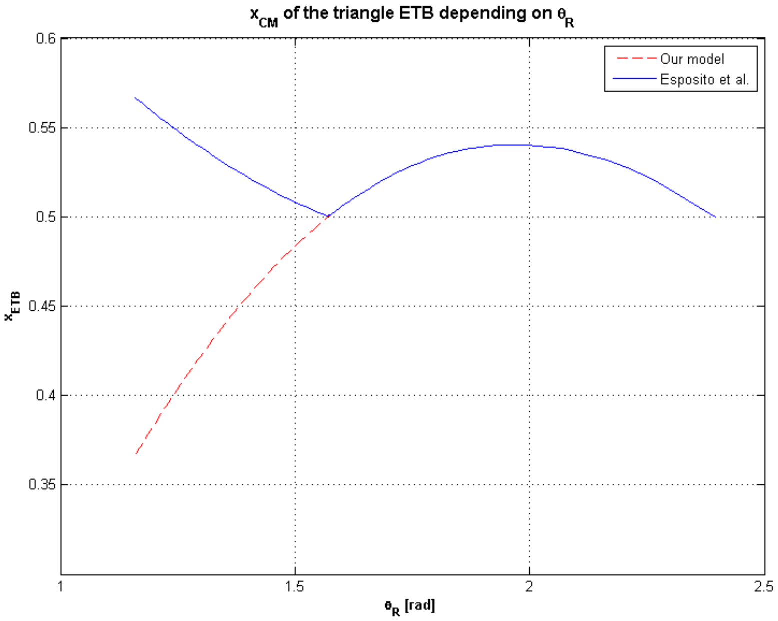

Figure 2.12: Center of mass coordinates depending on θ_A

Alternatively, the present model uses the same formula for both cases and the result makes sense: when $\theta_\mathrm{R} > \frac{\pi}{2}$, the center of mass of the ETB triangle is outside the droplet and is greater than the chord. On the other hand, when $\theta_{\mathrm{R}} < \frac{\pi}{2}$ the center of mass of the aforementioned triangle is inside the droplet, which means that its x-coordinate has to be less than the chord.

Finally, the center of mass of the droplet can be computed using the different equations displayed in the previous sections:

$$x_{\mathrm{drop}} = \frac{x_{\mathrm{circ}}A_{\mathrm{circ}} - x_{\widehat{AHC}}A_{\widehat{AHC}} - x_{\widehat{CT}}A_{\widehat{AHC}} + x_{\mathrm{CTE}}A_{\mathrm{CTE}} + x_{\mathrm{ETB}}A_{\mathrm{ETB}}}{A} \tag{2.111}$$

$$y_{\mathrm{drop}} = \frac{y_{\mathrm{circ}}A_{\mathrm{circ}} - y_{\widehat{AHC}}A_{\widehat{AHC}} - y_{\widehat{CT}}A_{\widehat{AHC}} + y_{\mathrm{CTE}}A_{\mathrm{CTE}} + y_{\mathrm{ETB}}A_{\mathrm{ETB}}}{A} \tag{2.112}$$

Having the center of mass well characterized, the previous equations are implemented in MATLAB, and the relationship of both coordinates of the center of mass with the advancing angle can be seen in Figure 2.13. Additionally, the results obtained by Esposito et al. [20] are displayed as well, proving that there is a good agreement between both results.

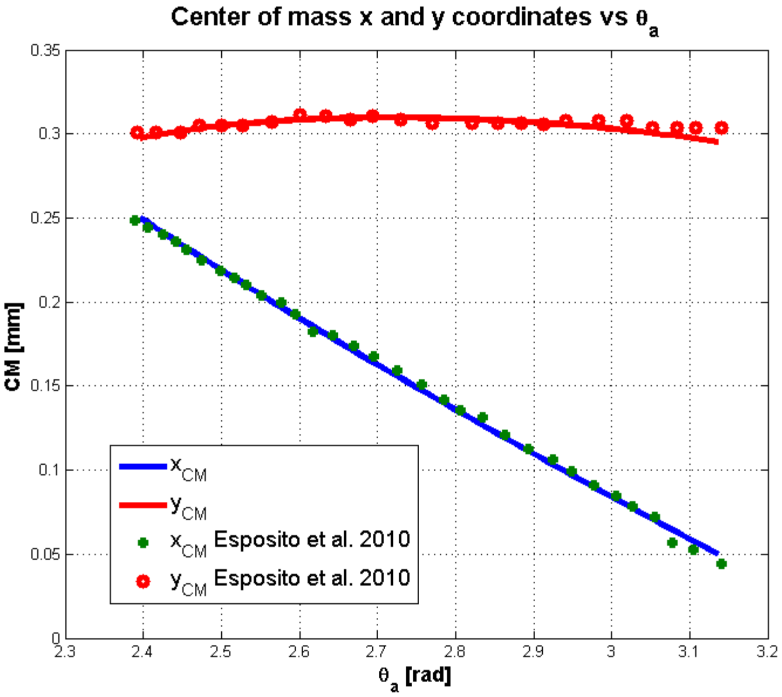

Figure 2.13: Center of mass coordinates depending on θ_{A}

Two conclusions can be extracted from Figure 2.13. Firstly, the y-coordinate of the mass center is fairly constant with respect the advancing angle. In addition, the relationship between the x-coordinate and θ_{A} is linear, so a fitting curve can be obtained. This means that if one can find an explicit relationship between the x-coordinate and the advancing angle, it is also possible to find its relationship with the radius, the height and the perimeter of the droplet.

2.3.5 Volume of the droplet

Another important variable that needs to be parameterized is the droplet volume. Figure 2.5 shows the geometry of a static droplet laying on a horizontal surface. Its volume can be computed as the difference between the volume of the sphere of radius R_s minus the volume of the spherical cap:

$$V_{drop} = V_{sphere} - V_{cap} \tag{2.113}$$

Volume of the sphere

The equation for the sphere volume is well-known. For a sphere of radius R_s:

$$V_{sphere} = \frac{4}{3}\pi R_s^3 \tag{2.114}$$

Volume of the spherical cap

The volume of a spherical cap contained in a sphere of radius R (Figure A.1 in Appendix A can be expressed with the following equation:

$$V_{cap} = \frac{\pi}{3}R_s^3\left(1+\cos\theta_s\right)^2\left(2-\cos\theta_s\right) \tag{2.115}$$

Volume of the droplet

Finally, according to equations (2.113), (2.114) and (2.115), the volume of the droplet is expressed by the following equation:

$$V_{drop} = \frac{4}{3}\pi R_s^3 - \frac{\pi}{3}R_s^3\left(1+\cos\theta_s\right)^2\left(2-\cos\theta_s\right) = R_s^3\left[\frac{4}{3}\pi - \frac{\pi}{3}\left(1+\cos\theta_s\right)^2\left(2-\cos\theta_s\right)\right] \tag{2.116}$$

Equation (2.116) can be used to have an explicit relationship between the droplet chord and its volume:

$$c_s = 2R_s\sin\theta_s = 2\sin\theta_s\left[\frac{V_{\text{drop}}}{\frac{4}{3}\pi - \frac{\pi}{3}\left(1+\cos\theta_s\right)^2\left(2-\cos\theta_s\right)}\right]^{\frac{1}{3}} \tag{2.117}$$

It is worth mentioning that this equation is different than the one proposed by Esposito et al. [20]:

$$c_s = 2\sin\theta_s\left[\frac{V_{\text{drop}}}{\frac{4}{3}\pi - \pi\left(1+\cos\theta_s\right)^2\cos\theta_s}\right]^{\frac{1}{3}} \tag{2.118}$$

Contact line

The surface tension force is a force that acts along the droplet contact line [15]. However, this line has not been characterized yet. In order to simplify the computation of the surface tension force, the contact line will be considered rectangular. Since the volume and the area are already described by equations (2.116) and (2.68) respectively, the thickness of the cylinder can be found as follows:

$$\begin{aligned} t_d = \frac{V}{A} &= \frac{R_\mathrm{S}^3 \left[\frac{4}{3}\pi - \frac{\pi}{3}\left(1+\cos\theta_\mathrm{S}\right)^2\left(2-\cos\theta_\mathrm{S}\right)\right]}{R_\mathrm{S}^2\left(\theta_\mathrm{S} - \frac{\sin 2\theta_\mathrm{S}}{2}\right)} = \\ &= R_\mathrm{S}\frac{\left[\frac{4}{3}\pi - \frac{\pi}{3}\left(1+\cos\theta_\mathrm{S}\right)^2\left(2-\cos\theta_\mathrm{S}\right)\right]}{\left(\theta_\mathrm{S} - \frac{\sin 2\theta_\mathrm{S}}{2}\right)} \end{aligned} \tag{2.119}$$

Of course, this is a coarse approximation of the actual geometry of the contact line, but future works will include a parametrization of the contact line depending on the droplet deformation. As shown in [15], as soon as the droplet deforms, the contact line deforms as well, from a circular shape to a less intuitive shape, formed by half a circle and half an ellipse (Figure 2.14).

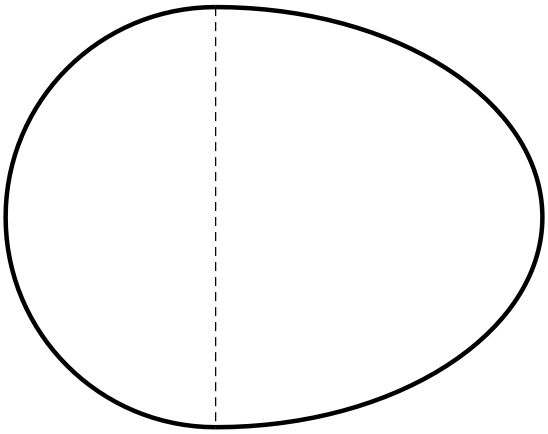

Figure 2.14: Droplet contact line once it is deformed

This shape is closer to the actual one due to the effect of pinning [20], [15].

2.4 Droplet Dynamics Model

2.4.1 Governing equation

In the previous section it has been concluded that the y-coordinate of the center of mass remains constant for the different values of the advancing angle. Thus, if one applies Newton's Second Law to the center of mass of the droplet, it only needs to be applied in the x-coordinate. The forces acting on the droplet are the drag force exerted by the air flowing around the dropet surface and the surface tension force. The former pushes the droplet away from its static configuration, whereas the latter tries to take the droplet back to its initial shape if it is deformed. Therefore, the dynamic equation applied to the droplet reads:

$$m\frac{d^2x_{\mathrm{CM}}}{dt^2} = F_{\mathrm{ST}} - F_{\mathrm{drag}} \tag{2.120}$$

The mass is a function of time as well, and is computed with the following equation:

$$m\left(t\right) = \left(Qt + V_0\right)\rho_w \tag{2.121}$$

where Q is the water flow rate, V_0 is the initial volume of the droplet and ρ_w is the water density.

2.4.2 Drag force

The equation used for the characterization of the drag force is the one used for an object moving into a fluid or, in this case, an static object inside a fluid flow:

$$F_{\mathrm{drag}} = \frac{1}{2}C_{\mathrm{D}}\rho_{\mathrm{air}}u_{\mathrm{air}}^2A \tag{2.122}$$

where the air density ρ_{air}, the air mean velocity u_{air} and the droplet projected frontal area A are well-known. This equation is valid for the considered conditions of the present work, and it is justified in the *Droplet height* study of this section. On the other hand, the drag coefficient C_{D} depends on the droplet geometry and the air velocity, amongst other factors. In reference [20], this parameter is computed using the formula from White's book, Chapter 4 [40]:

$$C_{\mathrm{D}} = 0.4 + \frac{24}{Re} + \frac{6}{1+\sqrt{Re}} \tag{2.123}$$

which is used to estimate the drag coefficient for a free sphere immersed in a gas flow and is based on the droplet diameter. Of course, the droplet shape is far away from a sphere, and this approximation has been identified as one of the factors that take the model predictions away from the experimental data [20]. Consequently, the best option is to implement the droplet geometry using a CFD software and compute the drag force numerically. Since there are a lot of factors involved in the value of F_{drag} and C_{D}, two of them have been chosen as the most important:

- The droplet height, which can be used as the characteristic length to compute the Reynolds number, i.e. Re_{h}
- The droplet deformation state, which can be described with the contact angle hysteresis.

The rest of the parameters, such as the channel geometry, the air density, viscosity and mean velocity or the water mass flow have been kept constant in the study of the drag coefficient. Several simulations have been done using the software COMSOL for every parameter, so their effects have been studied separately. The computational domain in the base case is a channel with a squared cross-sectional area of 13 mm per side and 500 mm long. It is significantly bigger than a fuel cell channel, but the computational domain has been designed to have a size that matches the experimental data setup in reference [20] for which experimental data has been reported in the literature.

The simulations have been done considering that the air is flowing in steady-state with a fully developed laminar profile for the velocity and an average value of u_{air} (Table 2.2 in Section 2.4.4). The governing equations of the air's velocity and pressure are the continuum and the momentum equations.

The boundary conditions are the following:

- Dirichlet boundary condition for the velocity at the inlet (yellow wall from Figure 2.15). Fully developed laminar profile with average velocity $u_{\text{air}} = 14.5$ m s^{-1}.
- Neumann boundary condition for the pressure at the outlet (green wall from Figure 2.15), i.e. no viscous stress.
- No slip boundary condition (rest of the domain walls).

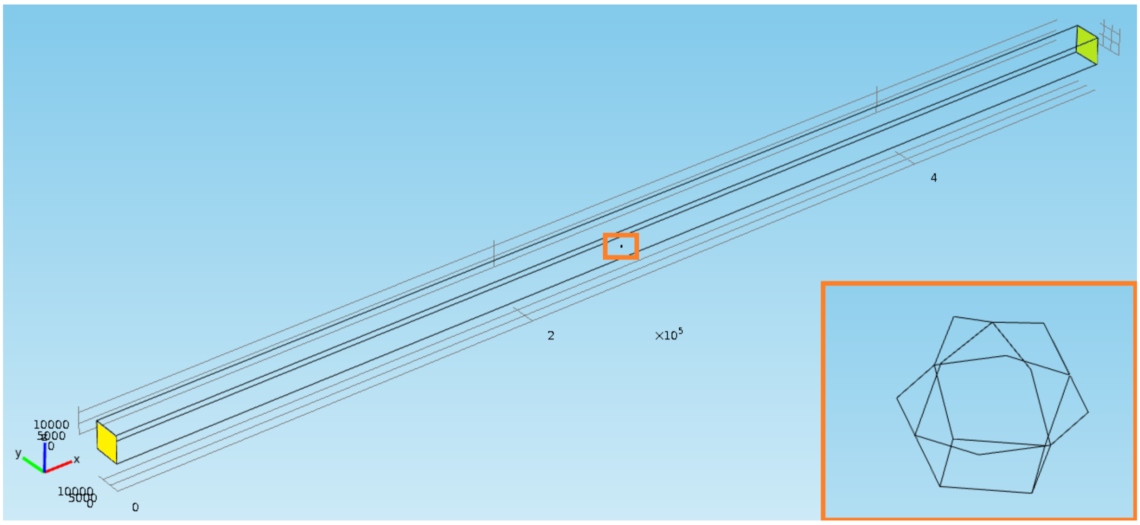

Figure 2.15: Computational domain of the channel and detail of the droplet geometry

The droplet has been characterized as an obstacle laying on the channel floor and therefore the no slip boundary condition is applied to the droplet surface as well. Since the droplet size is really small compared to the channel size, Figure 2.15 shows a detail of the droplet geometry. Due to this difference of size, the mesh around the droplet has smaller elements than the rest of the geometry, thus increasing the number of elements. An example of one of the meshed geometries is depicted in Figure 2.16.

A mesh that provides grid independent results has been used. The channel smaller sides have been divided in 13 elements, and the sides along the channel have been divided in 1000 parts. The elements used are P1+P1 tetrahedrals. Having discretized the computational domain, the equations are solved using the direct

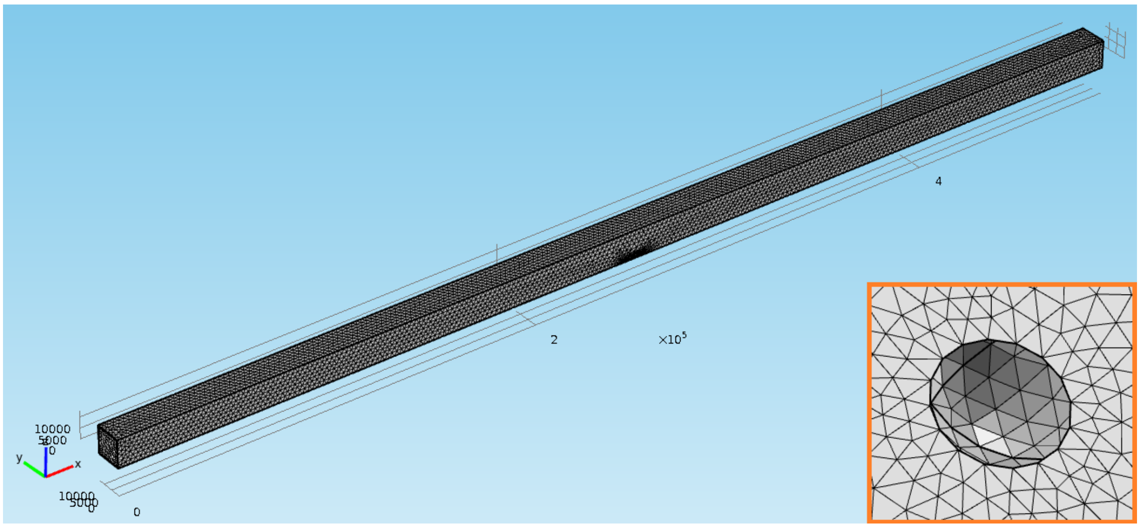

Figure 2.16: Channel geometry meshed with a detail of the droplet from below

solver MUMPS from COMSOL. In the following numerical simulations, the total number of elements has oscillated between 170000 and 200000 elements, having a computational time cost between 400 and 900s.

The objective of the present section is to compute the drag force of the air exerted on the droplet. This force is computed in COMSOL using the surface integration tool and integrating the pressure values over the droplet surface.

Droplet height

The droplet height is clearly one of the main factors that influences the drag coefficient value. The two previous cases have included a change in the droplet height. Here the effect of this variable is studied alone. The computational domain is maintained at a constant geometry of 13 mm of height and width, and a length of 500 mm. Using the values in section 2.4.4, the considered heights correspond to the values of the droplet from t = 0s to t = 1.5s, keeping the geometry in its static configuration. The obtained results are shown in Figure 2.17.

These two curves in the resulting plot correspond to the numerical result of the drag coefficient and the one obtained with equation (2.123) from White [40]. Note that the difference in some cases is almost 100% of the value. Since the water droplet is very small compared to the channel height, the hypothesis of the droplet under a free air stream is invalid. Thus, the drag force cannot be computed with the classic formula (2.122)The new values of this parameter will be used. There is a significant difference between the computed and the theoretical drag force as well, as one can observe in Figure 2.18

In order to check that equation (2.122) is valid, two points have been chosen from the data used in Figure 2.18. The first one is the point where $Re_h = 712$ and has half the area of the point located in $Re_h = 1003$. Since the force of the former (8×10^{-4} N) is aprrroximately half the drag force on the latter (1.57×10^{-3} N), it can be concluded that the equation for the drag force is valid in the scope of this work.

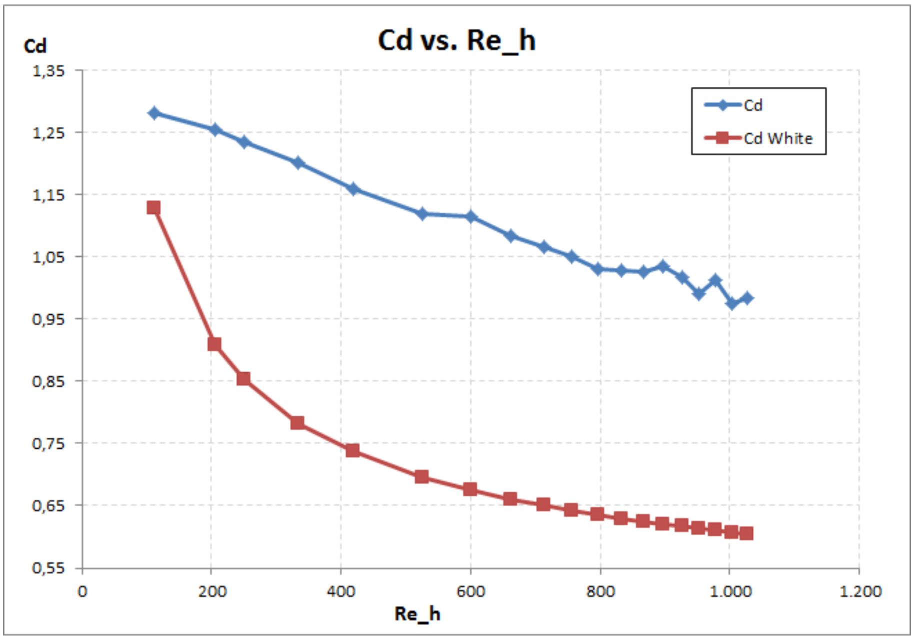

Figure 2.17: Theoretical and computed drag coefficient dependence on the droplet height

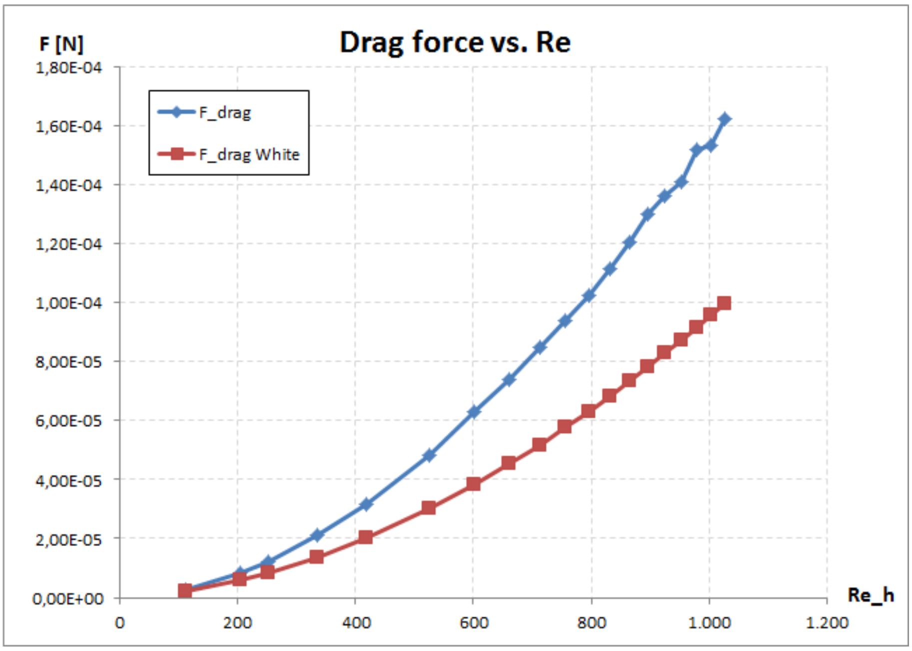

Figure 2.18: Theoretical and computed drag force dependence on the droplet height

Droplet deformation

The other variable to be analysed is the droplet deformation. The contact angle hysteresis is the indicator of this state: when the droplet is static, both advancing and receding angles are equal to the static contact angle, so the difference between them is 0. As the air flows around the droplet, the advancing angle grows and the receding angle diminishes as seen in Figure 2.6, thus increasing the difference between both angles. A more deformed shape of the droplet implies that it is more aerodynamic, which means that the drag coefficient is lower.

The three-dimensional geometry of the deformed droplet is not easy to draw in the computer. In the present study, it has been considered that the droplet tends to have the shape of a truncated ellipsoid, which makes sense considering the studies that have analysed the droplet deformation [15], [7], [35]. Although the shape of the droplet has been approximated, geometry variables such as droplet chord length, height, radius and frontal area have not been changed. Figure 2.19 shows the geometry of two deformed droplets:

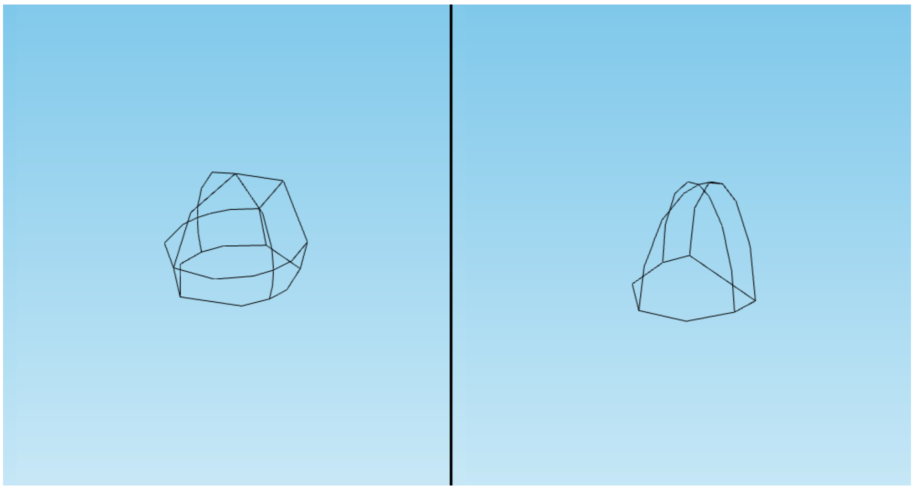

Figure 2.19: Deformed droplet geometries with contact angle histeresys 0.94 rad (left) and 1.68 rad (right)

After doing the simulations for three different deformation states, the results obtained are depicted in Figure 2.20.

These results show that the droplet deformation plays an important role in the value of both the drag coefficient and force (Figure 2.21).

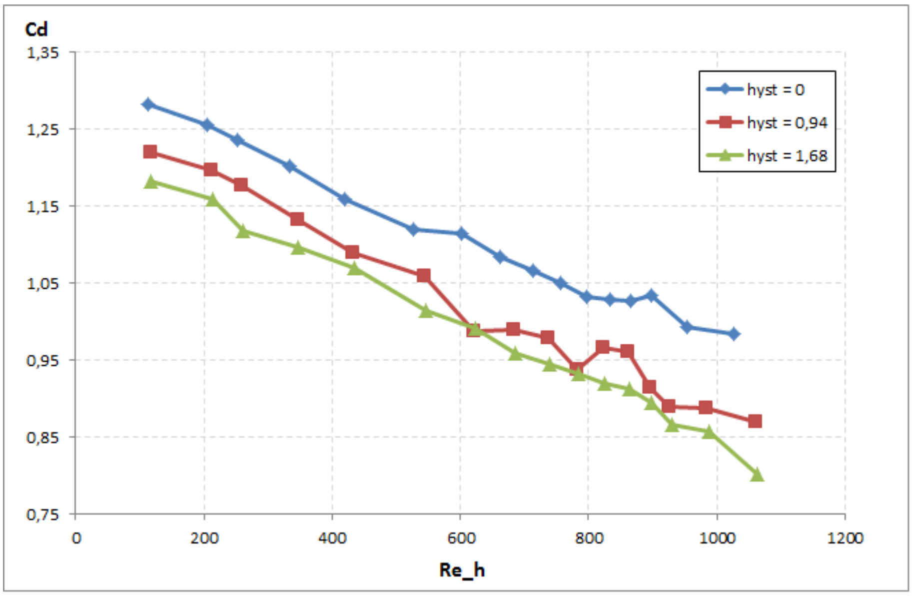

Figure 2.20: Drag coefficient of the two deformed droplets compared to the static geometry

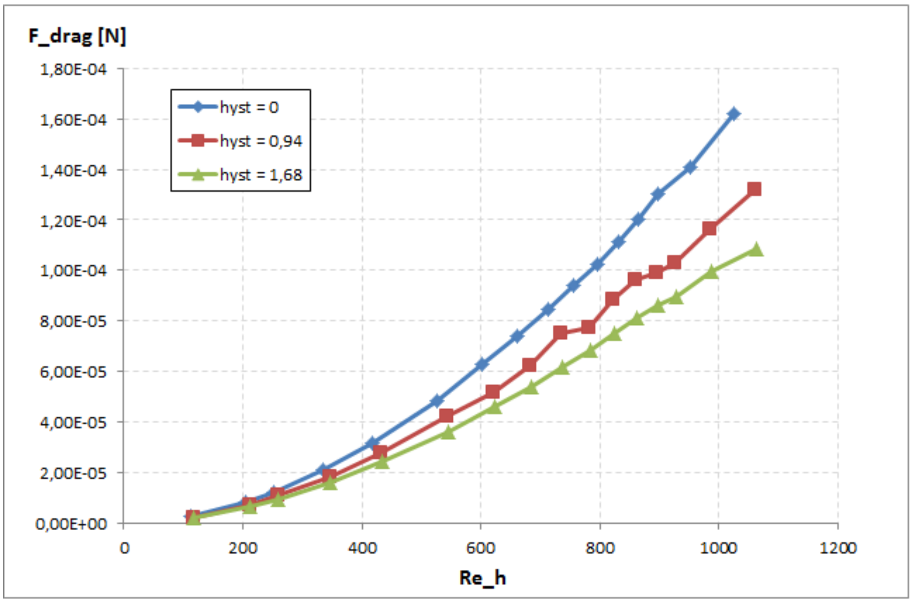

Figure 2.21: Drag force of the two deformed droplets compared to the static geometry

Drag coefficient parametrical equation

In the previous sections, the effects of the droplet height and its contact angle hysteresis on the drag coefficient have been studied. Multiple regression analysis is performed with the data obtained from the numerical simulations. The software Minitab v15 is used to run the statistical analysis, yielding the following output:

```
The regression equation is
Cd = 1,33 - 0,000366 Re_h - 0,0730 hyst


Predictor         Coef     SE Coef       T      P
Constant       1,33266     0,00731  182,33  0,000
Re_h       -0,00036565  0,00000924  -39,58  0,000
hyst         -0,072978    0,003834  -19,04  0,000


S = 0,0182599   R-Sq = 97,7%   R-Sq(adj) = 97,6\%
```

The drag coefficient as a function of Reyolds number and hysteresis angle is shown in the second line of the analysis output. The previous table analyses each variable independently and also shows its significance in the model, represented by the p-value (rightmost column in the table). Given the chosen Confidence Interval (95%), a variable is considered statistically significant when the p-value is lower than 5% (i.e. p ¡ 0,05). This percentage indicates the probability of accepting a linear relationship when it actually do not exist (Type I error). The resulting table indicates that the three variables included in the model have p-values lower than 0,001, and thus they are statistically significant in the model. The resulting equation is represented in a three-dimensional plot shown in Figure 2.22.

The relationship between the drag coefficient and the considered variables is fairly linear since the $R - sq$ value of the resulting model is closer to 100%.

2.4.3 Surface tension force

As said before, this force acts when the droplet is taken away from its resting position and is proportional to the deformation. Celestini and Kofman (2006) [38] stated that this restoring force can be expressed as:

$$F_{\mathrm{ST}} = -\gamma \frac{\Delta S}{dx} \tag{2.124}$$

where γ is the water surface tension, ΔS is the surface variation due to the deformation and dx is the displacement of the center of mass from its original position. Even though this form of the surface tension is very intuitive, it is an approximation of the actual phenomena. Moreover, the spring model can create a misunderstanding since the spring force acts on the center of mass, whereas the adhesion force takes place in the contact line with the surface. Thus, in this work the equation considered for the adhesion force of the droplet is [15]:

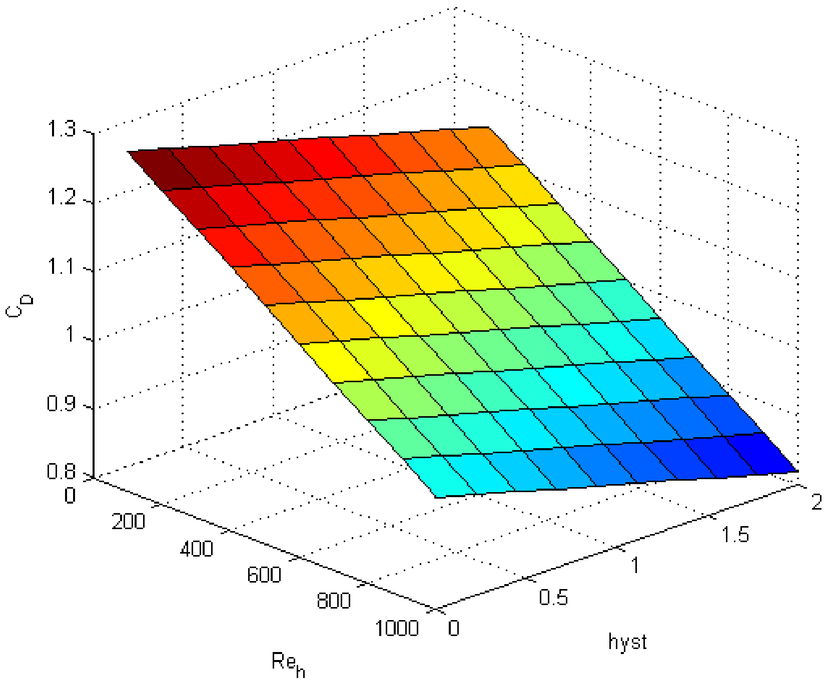

Figure 2.22: Drag coefficient representation as a function of the hysteresis angle and the Reynolds number

$$F_{\mathrm{ST}} = k\gamma t_{\mathrm{d}} \left(\cos\left(\theta_R\right) - \cos\left(\theta_A\right)\right) \tag{2.125}$$

where $k = 2$ since the contact line is considered to be rectangular.

2.4.4 Boundary and initial conditions

In order to solve the differential equation (2.120), some conditions must be imposed regarding the x-coordinate of the center of mass. Since equation (2.120) is a second order differential equation, two initial conditions must be imposed (equations (2.126) and (2.127)).

$$x_{\mathrm{CM}}\big|_{t=0} = \frac{c_0}{2} \tag{2.126}$$

$$\left.\frac{dx_{\mathrm{CM}}}{dt}\right|_{t=0} = v_{\mathrm{CM}}\big|_{t=0} = 0 \tag{2.127}$$

In other words, at $t = 0$ the droplet is static as shown in Figure 2.5. The term c_0 refers to the droplet chord at the beginning of the simulation. The rest of the parameters used in the simulation are described in Table 2.2.

The velocity of the air inside the channel is given by the geometry of the channel and the working conditions of the fuel cell. Typically, a fuel cell channel has a 1 mm × 1 mm cross-sectional area and 5 cm length. An usual value for the current density

Variable	Simbol	Value	Units
Initial chord	c_0	0.1	mm
Water flow rate	Q	0.1	μl s^{-1}
Water surface tension	γ	0.072	N m^{-1}
Water density	ρ_{w}	1000	kg m^{-3}
Static contact angle	θ_{S}	137	°
Air density	ρ_{air}	1.205	kg m^{-3}
Air viscosity	μ_{air}	1.98×10^{-5}	kg m^{-1} s^{-1}
Air velocity	u_{air}	14.5	m s^{-1}
Channel height	H	13	mm

Table 2.2: Parameters used in the simulation

is 1 A cm^{-2}, and for this current the amount of oxygen needed in the cathode is given by:

$$\dot{m}_{\mathrm{O}_2} = \frac{I}{4F} = \frac{i \cdot A_{\mathrm{act}}}{4F} \tag{2.128}$$

where i is the current density, A_{act} is the active area of the channel and F is the Faraday's constant, which equals to 96485 C mol^{-1} or, equivalently, 96485 A s mol^{-1}. Given that the base of the channel is a rectangle of 1 by 50 mm, the oxygen needed is:

$$\dot{m}_{\mathrm{O}_2} = \frac{1\frac{\mathrm{A}}{\mathrm{cm}^2} \cdot 0.5\mathrm{cm}^2}{4 \cdot 96485\frac{\mathrm{C}}{\mathrm{mol}}} = 1.2955 \cdot 10^{-6}\frac{\mathrm{mol\ O}_2}{s} \tag{2.129}$$

Finally, the necessary mass flow of air needed to have the desired current density is:

$$\dot{m}_{\mathrm{air}} = 1.2955 \cdot 10^{-6}\frac{\mathrm{mol\ O}_2}{s} \times \frac{1\mathrm{mol\ air}}{0.21\mathrm{mol\ O}_2} \times 28.96\frac{\mathrm{g}}{\mathrm{mol\ air}} \times \frac{1m^3}{1205\mathrm{g}} = 1.4827 \cdot 10^{-7}\frac{m^3}{s} \tag{2.130}$$

For the considered geometry, this value of the mass flow gives an inlet air velocity of 0.1483 m s^{-1}. Nonetheless, the considered value for the velocity is 14.5 m s^{-1} since it matches with the experimental setup found in literature [20].

Equation (2.120) and the aforementioned boundary conditions are implemented in MATLAB an solved using the 4th order Runge-Kutta method.

2.4.5 Solution Procedure

To test the numerical algorithm has been coded correctly, an ODE that has a well-known exact solution is solved using the implemented method. The equation is:

$$ay'' + by' + cy = 0 \tag{2.131}$$

Equation (2.131) is a 2nd order ODE with the following exact solution:

$$y\left(x\right) = c_1 e^{\lambda_1 x} + c_2 x e^{\lambda_2 x} \tag{2.132}$$

where λ_1 and λ_2 are found with the characteristic equation:

$$a\lambda^2 + b\lambda + c = 0 \tag{2.133}$$

and the constants c_1 and c_2 are found imposing some boundary conditions. As an example, the following equation is solved:

$$y'' - 2y' + y = 0 \tag{2.134}$$

with the following boundary conditions:

$$y\left(0\right) = 1$$

$$y'\left(0\right) = 0 \tag{2.135}$$

Using the characteristic equation (2.133) and the boundary conditions, the exact solution of the ODE (2.134) is:

$$y\left(x\right) = e^x - xe^x \tag{2.136}$$

The MATLAB code is used to solve equation (2.134), and the result is shown in Figure 2.23. Therefore, it can be said that the numerical algorithm that solves the current problem has been implemented correctly. The code used in this section can be found in Appendix D.3.

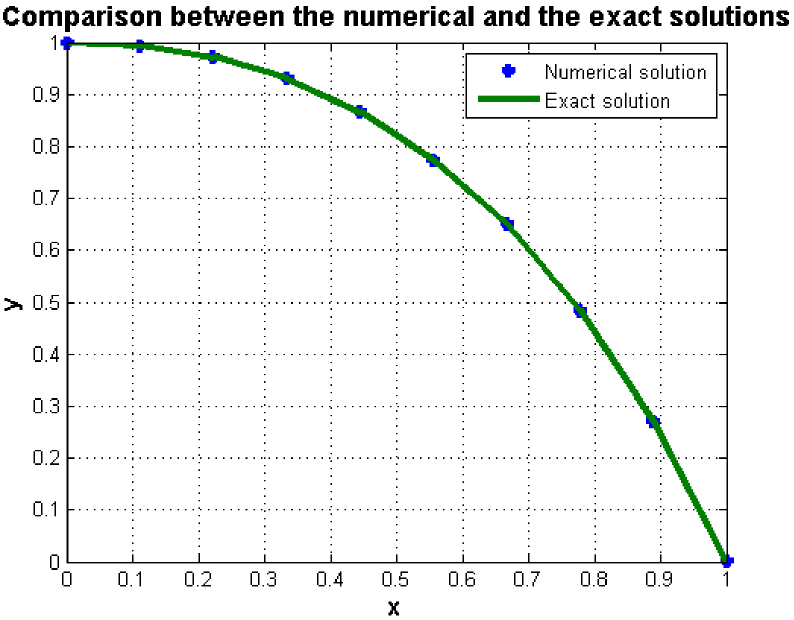

Figure 2.23: Numerical and exact solution of a 2nd order ODE using the developed code

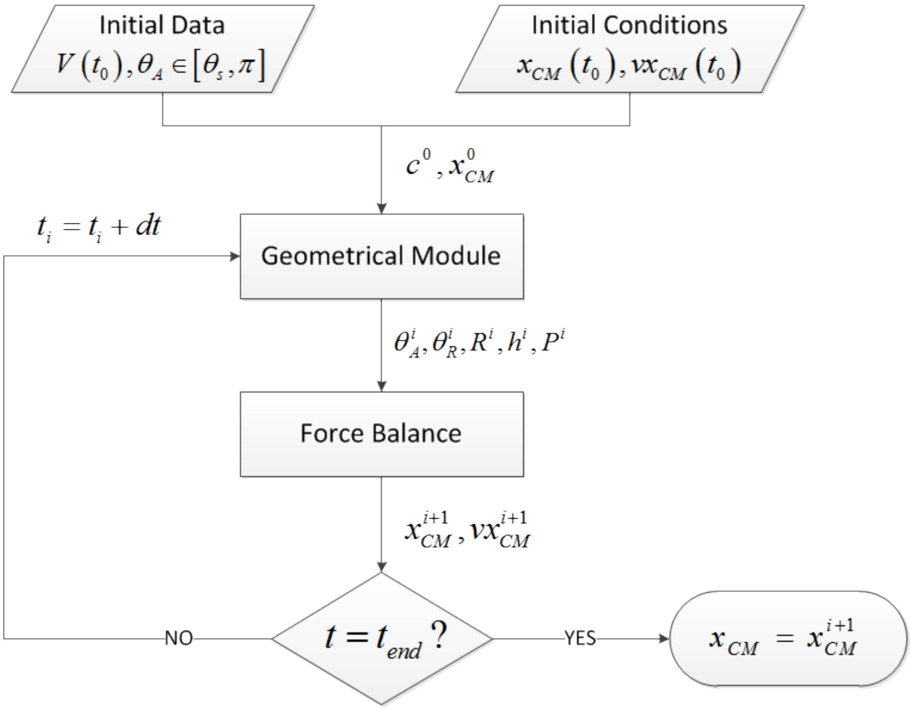

Figure 2.24: Flowchart of the algorithm to solve the dynamic problem

2.5 Flowchart

The whole algorithm described in the previous sections can be summarised in the flowchart shown on Figure 2.24. Initially, the droplet has a certain volume. Since the water flow rate is known, the volume and the chord length are recalculated at every time step using equations (2.121) and (2.117), respectively. Using the initial data from the previous section, the geometric variables are computed in the geometric module, which provides the droplet height, contact angles and cross-sectional area needed to compute the shear drag force. Then, the force balance is solved and the center of mass x-coordinate is obtained.

This process is repeated until the time step reaches the final time of the simulation or some critical condition is reached. Such condition could be that the droplet height is equal to the channel height or that the advancing or receding angles have reached a maximum value. The first condition has not been implemented because the droplet modelled is assumed to be small compared to the channel height. A maximum value for the hysteresis angle is applied as a detachment condition.

Chapter 3

Results and discussion

In this section, the most important results regarding the droplet dynamics are displayed. The total time of the simulation is 1s, using a droplet that grows constantly. The velocity of the air flowing around the droplet is 14.5 m s^{-1} (Table 2.2). The simluation shows the evolution of the droplet shape at every time step suring its execution. Figure 3.1 shows the simulation state at four different time steps.

The time step size chosen for this simulation is 10^{-4}s, and the total computational time is about 2 min.

3.1 Evolution of the center of mass and hysteresis angle

The evolution of the x-coordinate of the center of mass over time is shown in Figure 3.2. The evolution of the x-coordinate of a static droplet is shown as well, in order to notice the effects of the airflow. The origin of the x-coordinate is shown in Figure 2.3.

Since the two forces acting on the droplet have opposite directions, the center of mass oscillates during droplet growth. The advancing and receding angles have oscillations as well, as displayed on Figure 3.3.

In this simulation, as the droplet grows, the drag force deforms the droplet. As the drag increases, the difference between both angles also increases, which is represented as the hysteresis angle.

3.2 Influence of the air velocity

This section is devoted to study the effect of the air velocity on the evolution of the center of mass x-coordinate. Four different simulations have been done, considering a different air velocity in each one: 0, 5, 10 and 20m/s. The results are shown on Figure 3.4.

Two effects can be observed in Figure 3.4. First, the higher the air velocity, the stronger the drag force, which leads to a bigger deformation. In other words, the final value of the x-coordinate is lower as the velocity increases. Second, the amplitude of the oscillations increases due to the same reason, but the frequency

(a) t = 0 s (b) t = 0.25 s

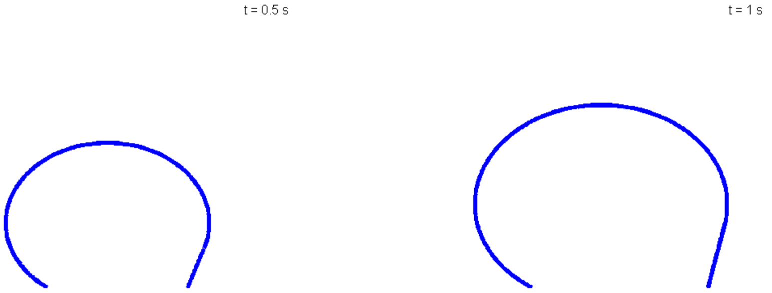

(c) t = 0.5 s (d) t = 1 s

Figure 3.1: Droplet deformed shape representation at different time steps of the simulation

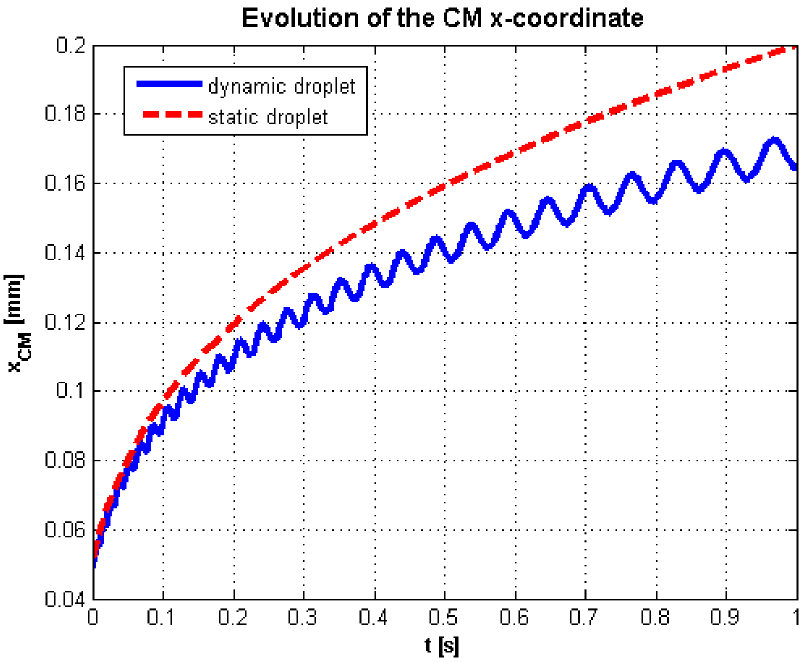

Figure 3.2: Evolution of the x-coordinate of the center of mass over time

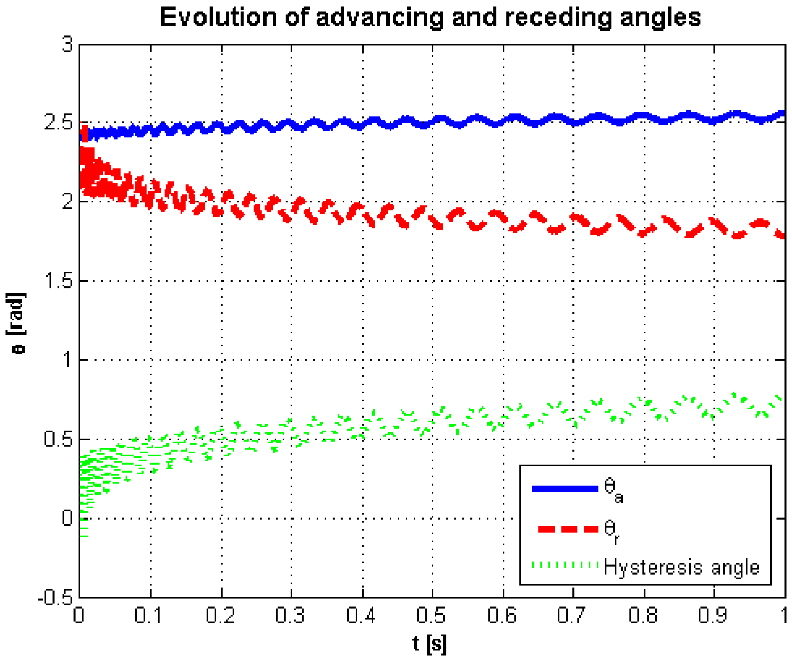

Figure 3.3: Evolution of the advancing and receding angles over time

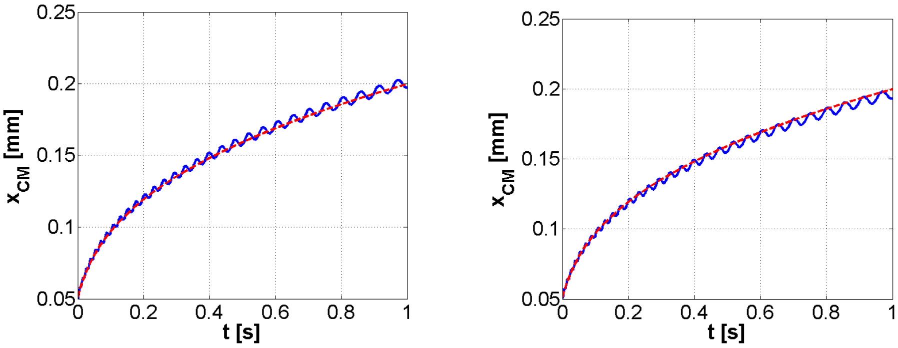

(a) $u_{\text{air}} = 0m/s$ (b) $u_{\text{air}} = 5m/s$

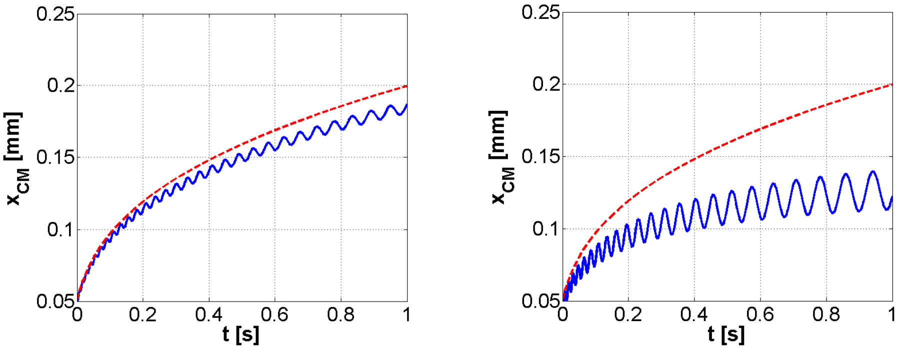

(c) $u_{\text{air}} = 10m/s$ (d) $u_{\text{air}} = 20m/s$

Figure 3.4: Influence of the air velocity on the evolution of the center of mass

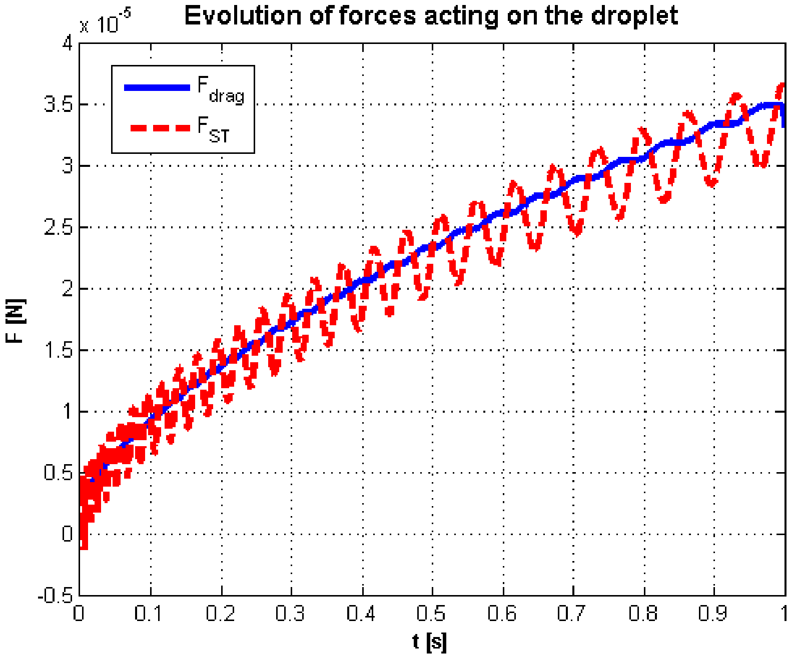

Figure 3.5: Evolution of the forces acting on the droplet over time

remains constant. Future works will include a frequency analysis depending on the droplet geometry.

The evolution of the center of mass observed in Figure 3.4(a) should be a straight line since the velocity of the air is 0, but instead, it has some small oscillations. These oscillations are caused by the approximation introduced in the geometry model because the angles and lengths are approximated by fitting functions.

3.3 Evolution of the forces acting on the droplet

The two forces acting on the droplet are responsible for its oscillation. As the droplet grows, the drag force increases since it has a linear relationship with the frontal area (equation (2.122)). The surface tension force is modelled using equation (2.125). The evolution of both forces over time is shown in Figure 3.5.

The results in Figure 3.5 correspond to the simulation done in Section 3.1. One can observe that the drag force oscillates with a small amplitude compared to the surface tension force. The main reason is that, for a certain droplet size, the frontal area does not change much with the oscillation of the center of mass x-coordinate. In addition, the drag force has a quadratic growth due to its quadratic relationship with the droplet radius (equations (2.122) and (2.68)).

3.4 New formulation of the drag force

In Section 2.4.2 it has been stated that some authors use the equation from White's book [40] for the drag coefficient. If C_D is computed with equation 2.123, the results

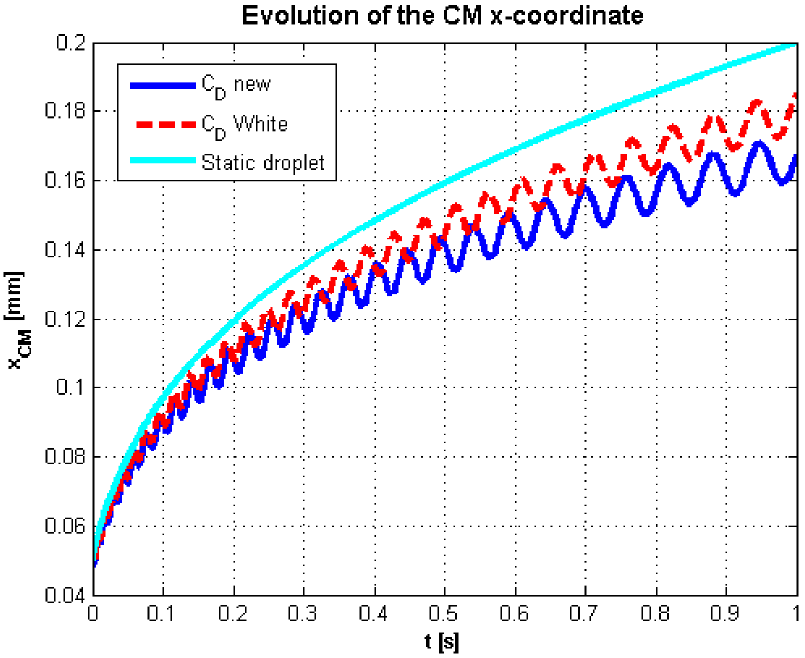

Figure 3.6: Evolution of the x-coordinate of the center of mass over time

of the previous simulation for the x-coordinate evolution is shown in Figure 3.6.

As seen on Section 2.4.2, Figure 2.17 shows that White's formula underestimates the drag coefficient for the current flow conditions, even for the fully deformed droplet. Thus, the value of the drag force is underestimated as well, giving as a result a less deformed droplet (red dashed curve from Figure 3.6), closer to the static configuration.

3.5 New formulation of the surface tension force

The alternative equation for the surface tension force from studies [20] and [38] is considered in this section. This equation can be found in Section 2.1.2, equation (2.27). The MATLAB simulation is run again, yielding the following result for the center of mass x-coordinate (Figure 3.7).

Adhesion model refers to the model considered in the present study (equation (2.31)), and *Spring model* is the model that uses equation (2.27). From Figure 3.7 it is clear that the droplet has bigger deformations with this formulation of the surface tension force. In other words, the surface tension has lower values and it is less resistant to the drag force. This drop in the surface tension force can be also observed in Figure 3.8.

The oscillations in the spring model have more amplitud but less frequency, as shown in Figure 3.7.

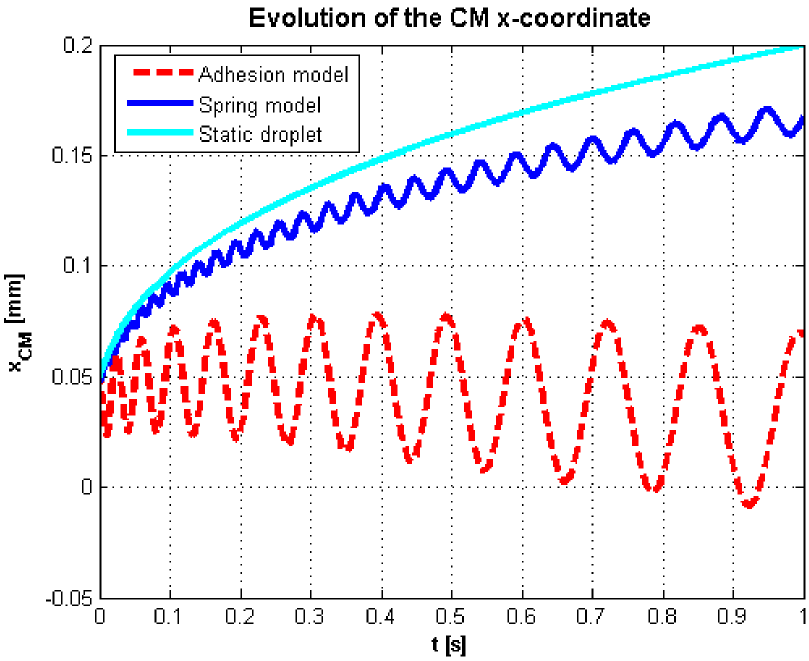

Figure 3.7: Evolution of the x-coordinate of the center of mass over time

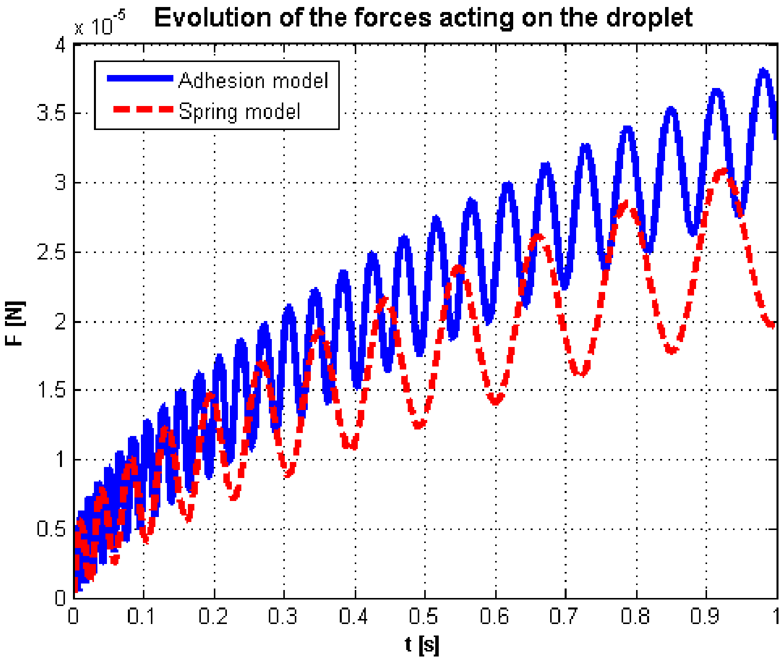

Figure 3.8: Evolution of the surface tension force of both models over time

3.6 Influence of the liquid mass flow

Considering that the surface tension force is modelled with the adhesion model (equation (2.31) from Section 2.1.2), it is worth finding the effect of the liquid mass flow on the evolution of the center of mass x-coordinate. Four different simulations have been done, considering a different mass flow in each one: 1.6, 3.2, 6.4 and 12.8 μl min^{-1}. The results are shown on Figure 3.9.

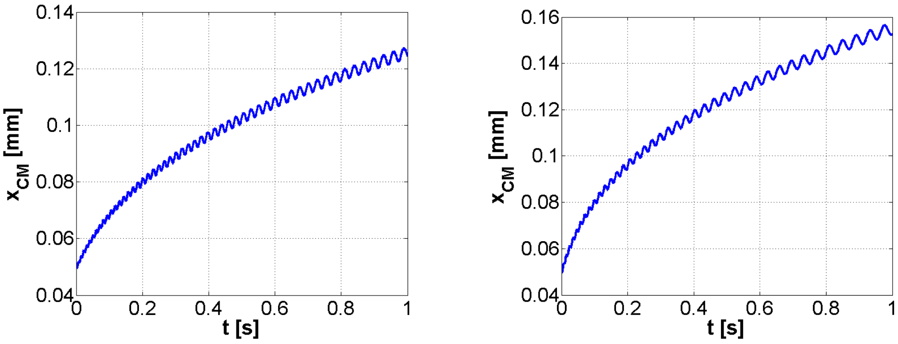

(a) $Q = 1.6\mu$l min^{-1} (b) $Q = 3.2\mu$l min^{-1}

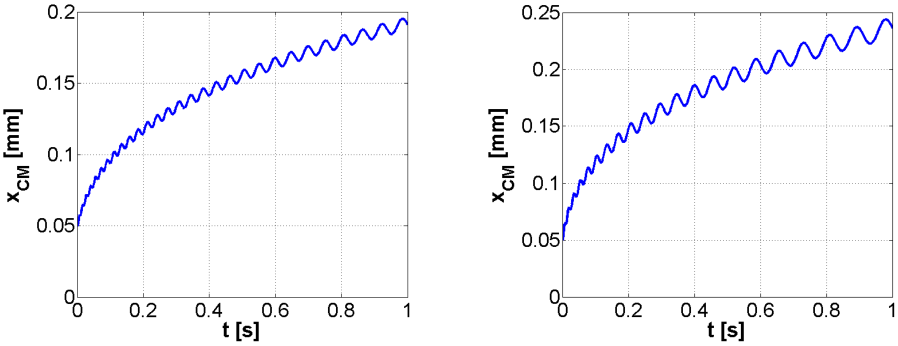

(c) $Q = 6.4\mu$l min^{-1} (d) $Q = 12.8\mu$l min^{-1}

Figure 3.9: Influence of the mass flow on the evolution of the center of mass

Obviously, the bigger the mass flow rate, the higher is the value of the x-coordinate since the droplet grows faster during the same simulation time. However, this is not the effect that needs to be analyzed. It is important to notice that as the mass flow grows, the number of oscillations decreases. In other words, an increase in the mass flow means a decrease in the frequency.

Other studies of water droplet modelling have used different values of water flow rate. For instance, in the base case of Zhu et al. study [6], the water emerges from a circular pore of 50μm of diameter at a speed of 1ms^{-1}, which means that the flow rate is equal to 118μl min^{-1}. The same value of water flow rate is used in reference [4]. Kumbur et al. [7] used a constant water flow rate of 23μl min^{-1}. Theodorakakos [3] used different values for both the pore size and the water inlet velocity, giving values of the water flow rate within the range of 0.08 and 106μl min^{-1}. More recently, Wu and Djilali [11] chose a water flow rate between 3 and 15μl min^{-1}.

3.7 Oscillation frequency

In the previous sections, it has been shown that the droplet oscillates as it grows due to the forces acting on it. Thus, it would be interesting to carry out a frequency analysis of these oscillations. To this end, several simulations were performed considering a droplet of a fixed mass in order to obtain the frequency depending on its size. The results are displayed in Figure 3.10.

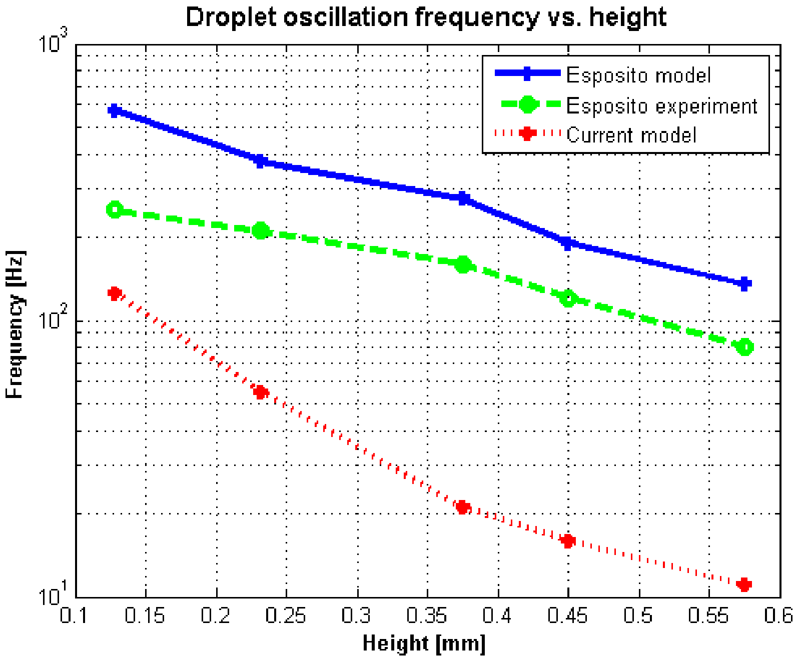

Figure 3.10: Frequency of oscillation of the droplet depending on its heigth

The results for the droplet oscillation in Figure 3.10 are significantly different from the results of Esposito et al. [20]. The liquid mass flow data provided in that study do not correspond with their results since it should have to be higher in order to match with the results of the droplet growth. Therefore, it is pointless to compare the results from reference [20] with the current results since they are based on different data. Despite this fact, the frequency results from the present study have the same tendency than the other results, i.e. bigger droplets have lower oscillation frequencies [38].

Chapter 4

Conclusions and future work

A semi-analytical model of a water droplet emerging from a GDL pore in a cathode gas channel has been developed. The drag coefficient has been identified in the literature as one key parameter that introduces errors in the analytical model predictions [20]. Using a CFD software, the geometry of the channel has been modeled as well as the geometry of the droplet. Several simulations have been done for different droplet sizes and deformation states. A statistical analysis of the resulting data leads to the conclusion that the drag coefficient has a linear relationship with the Reynolds number (computed with the droplet height) and hysteresis angle. An explicit equation of this relationship is given in order to use it to compute the drag force in the analytical model of the droplet.

From the study of the drag coefficient it can also be concluded that studies using Reynolds number with the formula provided by White [40] underpredict the values of the drag coefficient and therefore the drag force.

The current analytical model has been implemented in MATLAB and it has proben to give results that are consistent with previous works [4], [3], [8], [20]. As the droplet grows, it oscillates due to the unbalanced acting forces, namely the drag and the surface tension force. The airflow velocity has been modified in order to check the consistency of the algorithm. When the velocity of the air is 0, the x-coordinate of the droplet center of mass evolves without almost any oscillation, as expected. It has been observed that the higher the air velocity, the bigger the amplitude of the droplet oscillations, i.e. the droplet is more unstable and is prone to detach from the GDL surface. The frequency of the oscillations however remains almost constant.

The results for the surface tension force show that the considered equation gives higher results than others obtained from a spring model [20], [38]. A lower value of the surface tension force means that the droplet oscillates with higher amplitude but with less frequency.

The value of the liquid mass flow has been changed as well. By increasing this parameter, the frequency of the oscillations has decreased but the amplitude has increased. Therefore, when the liquid water emerges faster from the pore, it will detach sooner.

The frequency analysis has shown very different results from similar studies [20]. Although the frequency decreases with the size of the droplet in both cases, the results cannot be compared since they are obtained using different data.

Despite all the work done so far, there is still much work to do regarding the simulation of the water droplet emerging from a pore. Future work includes:

1. function of the contact line depending on the droplet deformation
2. development of a solver for KRATOS using the particle method
3. experiment with an actual channel and injected water
4. fluid/structure interaction applications for the drag coefficient relationship
5. area coverage function
6. MEA + channel model
7. Cassie equation and Wenzel angle (chemical heterogeneity and roughness of the surface effects)

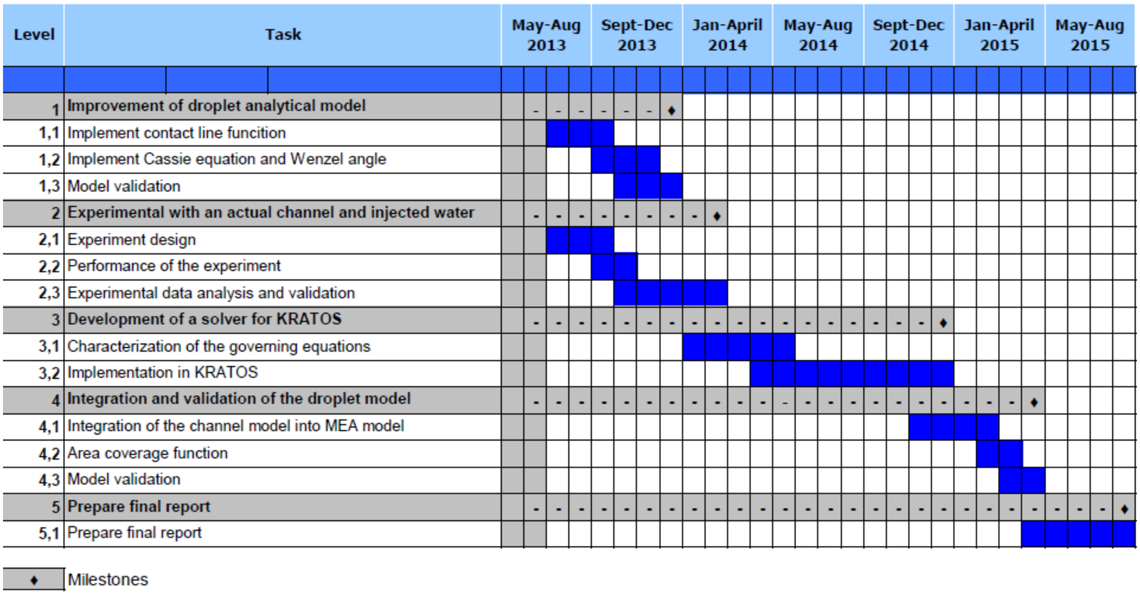

Level	Task	May-Aug 2013				Sept-Dec 2013				Jan-April 2014				May-Aug 2014				Sept-Dec 2014				Jan-April 2015				May-Aug 2015			
1	**Improvement of droplet analytical model**		-	-	-	-	-	-	♦																				
1,1	Implement contact line funcition			■	■	■																							
1,2	Implement Cassie equation and Wenzel angle					■	■	■																					
1,3	Model validation						■	■	■																				
2	**Experimental with an actual channel and injected water**		-	-	-	-	-	-	-	-	♦																		
2,1	Experiment design			■	■	■																							
2,2	Performance of the experiment					■	■																						
2,3	Experimental data analysis and validation						■	■	■	■	■																		
3	**Development of a solver for KRATOS**		-	-	-	-	-	-	-	-	-	-	-	-	-	-	-	-	-	-	♦								
3,1	Characterization of the governing equations									■	■	■	■	■															
3,2	Implementation in KRATOS												■	■	■	■	■	■	■	■	■								
4	**Integration and validation of the droplet model**		-	-	-	-	-	-	-	-	-	-	-	-	-	-	-	-	-	-	-	-	-	-	♦				
4,1	Integration of the channel model into MEA model																			■	■	■	■						
4,2	Area coverage function																						■	■					
4,3	Model validation																							■	■				
5	**Prepare final report**		-	-	-	-	-	-	-	-	-	-	-	-	-	-	-	-	-	-	-	-	-	-	-	-	-	-	♦
5,1	Prepare final report																								■	■	■	■	■

♦	Milestones

Figure 4.1: Gantt chart of future works

Figure 4.1 shows the Gantt chart of future works.

Bibliography

[1] USA College of the Desert. *Hydrogen Fuel Cell Engines and Related Technologies*. College of the Desert, 1st edition, 2001.

[2] J.G. Carton, V. Lawlor, A.G. Olabi, C. Hochenauer, and G. Zauner. Water droplet accumulation and motion in pem (proton exchange membrane) fuel cell mini-channels. *Energy*, 39:63–73, 2012.

[3] A. Theodorakakos, T. Ous, M. Gavaises, J.M. Nouri, N. Nikolopoulos, and H. Yanagihara. Dynamics of water droplets detached from porous surfaces of relevance to pem fuel cells. *Journal of Colloid and Interface Science*, 300:673–687, 2006.

[4] X. Zhu, P.C. Sui, and N. Djilali. Three-dimensional numerical simulations of water droplet dynamics in a pemfc gas channel. *Journal of Power Sources*, 181:101–115, 2008.

[5] X. Zhu, Q. Liao, P.C. Sui, and N. Djilali. Numerical investigation of water droplet dynamics in a low-temperature fuel cell microchannel: Effect of channel geometry. *Journal of Power Sources*, 195:801–812, 2010.

[6] X. Zhu, P.C. Sui, and N. Djilali. Numerical simulation of emergence of a water droplet from a pore into a microchannel gas stream. *Microfluid Nanofluid*, 4:543–555, 2008.

[7] E.C. Kumbur, K.V. Sharp, and M.M. Mench. Liquid droplet behavior and instability in a polymer electrolyte fuel cell flow channel. *Journal of Power Sources*, 161:333–345, 2006.

[8] K.S. Chen, M.A. Hickner, and D.R. Noble. Simplified models for predicting the onset of liquid water droplet instability at the gas diffusion layer/gas flow channel interface. *International Journal of Energy Research*, 29(12):1113–1132, 2005.

[9] Zhigang Zhan, Chen Wang, Weiguo Fu, and Mu Pan. Visualization of water transport in a transparent pemfc. *International Journal of Hydrogen Energy*, 37:1094–1105, 2012.

[10] F. Y. Zhang, X. G. Yang, and C. Y. Wang. Liquid water removal from a polymer electrolyte fuel cell. *Journal of The Electrochemical Society*, 153(2):A225–A232, 2006.

[11] T.C. Wu and N. Djilali. Experimental investigation of water droplet emergence in a model polymer electrolyte membrane fuel cell microchannel. *Journal of Power Sources*, 208:248–256, 2012.

[12] C.W. Hirt and B.D. Nichols. Volume of fluid (vof) method for the dynamics of free boundaries. *Journal of Computational Physics*, 39:201–225, 1981.

[13] V.R. Gopala and G.M. van Wachem. Volume of fluid methods for immiscible-fluid and free-surface flows. *Chemical Engineering Journal*, 141:204–221, 2008.

[14] E.B. Dussan and R.T. Chow. On the ability of drops or bubbles to stick to non-horizontal surfaces of solids. *Journal of Fluid Mechanichs*, 137:1–29, 1983.

[15] C.W. Extrand and Y. Kumagai. Liquid drops on an inclined plane: the relation between contact angles, drop shape, and retentive force. *Journal of Colloid and Interface Science*, 170:515–521, 1995.

[16] P. Dimitrakopoulos and J.J.L. Higdon. Displacement of fluid droplets from solid surfaces in low-reynolds-number shear flows. *Journal of Fluid Mechanichs*, 336:351–378, 1997.

[17] P. Dimitrakopoulos. Deformation of a droplet adhering to a soplid interface in shear flow: onset of interfacial sliding. *Journal of Fluid Mechanichs*, 580:451–466, 2007.

[18] S.D. Hong, M.Y. Ha, and S. Balachandar. Static and dynamic contact angles of water droplet on a solid surface using molecular dynamics simulation. *Journal of Colloid and Interface Science*, 339:187–195, 2009.

[19] V. Cristini and Y. C. Tan. Theory and numerical simulation of droplet dynamics in complex flows - a review. *Lab on a Chip*, 4:257–264, 2004.

[20] A. Esposito, P. Polverino, C. Pianese, and Y.G. Guezennec. A lumped model of single droplet deformation, oscillation and detachment on the gdl surface of a pem fuel cell. *ASME 2010 8th International Fuel Cell Science, Engineering and Technology Conference*, 2010.

[21] S. C. Cho, Y. Wanga, and K.S. Chen. Droplet dynamics in a polymer electrolyte fuel cell gas flow channel: Forces, deformation, and detachment. i: Theoretical and numerical analyses. *Journal of Power Sources*, 206:119–128, 2012.

[22] J.U. Brackbill, D.B. Kothe, and C. Zemach. A continuum method for modeling surface tension. *Journal of Computational Physics*, 100:335–354, 1992.

[23] K. Tuber, D. Pcza, and C. Hebling. Visualization of water buildup in the cathode of a transparent pem fuel cell. *Journal of Power Sources*, 124:403–414, 2003.

[24] X. G. Yang, F. Y. Zhang, A. L. Lubawy, and C. Y. Wang. Visualization of liquid water transport in a pefc. *Electrochemical and Solid-State Letters*, 7(11):A408–A411, 2004.

[25] M. A. Hickner, N. P. Siegel, K. S. Chen, D. N. McBrayer, D. S. Hussey, D. L. Jacobson, and M. Arif. Real-time imaging of liquid water in an operating proton exchange membrane fuel cell. *Langmuir*, 22(14):6234–6237, 2006.

[26] R. Satija, D.L. Jacobson, M. Arif, and S.A. Werner. In situ neutron imaging technique for evaluation of water management systems in operating pem fuel cells. *Journal of Power Sources*, 129:238–245, 2004.

[27] A. Hakenjos, H. Muenter, U. Wittstadt, and C. Hebling. A pem fuel cell for combined measurement of current and temperature distribution, and flow field flooding. *Journal of Power Sources*, 131:213–216, 2004.

[28] M. M. Daino, Z. Lu, J. M. LaManna, J. P. Owejan, T. A. Trabold, and S. G. Kandlikar. Through-plane water transport visualization in a pemfc by visible and infrared imaging. *Electrochemical and Solid-State Letters*, 14(6):B51–B54, 2011.

[29] M. Wang, K. W. Feindel, S. H. Bergens, and R. E. Wasylishen. In situ quantification of the in-plane water content in the nafion membrane of an operating polymer-electrolyte membrane fuel cell using 1h micro-magnetic resonance imaging experiments. *Journal of Power Sources*, 195:7316–7322, 2010.

[30] C. E. Colosqui, M. J. Cheah, I. G. Kevrekidis, and J. B. Benziger. Droplet and slug formation in polymer electrolyte membrane fuel cell flow channels: The role of interfacial forces. *Journal of Power Sources*, 196:10057–10068, 2011.

[31] S.H. Williams, A. Hilger, N. Kardjilov, I. Manke, M. Strobl, P.A. Douissard, T. Martin, H. Riesemeier, and J. Banhart. Detection system for microimaging with neutrons. *Journal of Instrumentation*, 7(2):P02014, 2012.

[32] S.G. Kandlikar, Z. Lu, W.E. Domigan, A.D. White, and M.W. Benedict. Measurement of flow maldistribution in parallel channels and its application to ex-situ and in-situ experiments in pemfc water management studies. *International Journal of Heat and Mass Transfer*, 52:1741–1752, 2009.

[33] N. Akhtar, A. Qureshi, J. Scholta, C. Hartnig, M. Messerschmidt, and W. Lehnert. Investigation of water droplet kinetics and optimization of channel geometry for pem fuel cell cathodes. *International Journal of Hydrogen Energy*, 34:3104–3111, 2009.

[34] M. Secanell, R. Songprakorp, A. Suleman, and N. Djilali. Multi-objective optimization of a polymer electrolyte fuel cell membrane electrode assembly. *Energy and Environmental Science*, 1:378–388, 2008.

[35] C. Antonini, F.J. Carmona, E. Pierce, M. Marengo, and A. Amirfazli. General methodology for evaluating the adhesion force of drops and bubbles on solid surfaces. *Langmuir*, 25(11):6143–6154, 2009.

[36] J.N. Israelachvili. *Intermolecular and Surface Forces.* Elsevier, 3rd edition, 2011.

[37] C.W. Extrand and A.N. Gent. Retention of liquid drops by solid surfaces. *Journal of Colloid and Interface Science*, 138(2):431–442, 1990.

[38] F. Celestini and R. Kofman. Vibration of submillimeter-size supported droplets. *Physical Review*, 73(1), 2006.

[39] A.J.B. Milne and A. Amirfazli. Drop shedding by shear flow or hydrophilic to superhydrophobic surfaces. *Langmuir*, 25(24):14155–14164, 2009.

[40] F.M. White. *Viscous Fluid Flow*. McGraw-Hill, 2nd edition, 1991.

Appendix A

Area ratio deduction

The droplet in its static configuration it's supposed to have the shape of a spherical cap, as shown on Figure A.1.

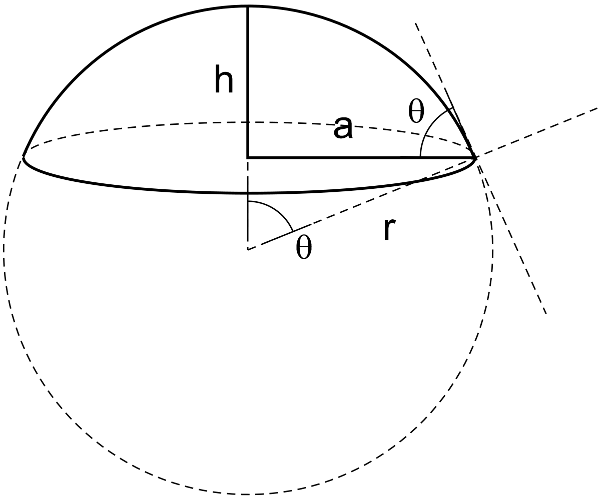

Figure A.1: Characterization of a droplet with a spherical cap shape

According to the considered geometry, the aforementioned areas can be described with equations (A.1) and (A.2), respectively.

$$A_{\mathrm{f}} = \pi a^2 = \pi \left(r\mathrm{sin}\theta\right)^2 = \pi r^2 \mathrm{sin}^2\theta \tag{A.1}$$

$$A_{\mathrm{c}} = 2\pi r h = 2\pi r \left(r - r\mathrm{cos}\theta\right) = 2\pi r^2 \left(1 - \mathrm{cos}\theta\right) \tag{A.2}$$

At equilibrium, equation (2.7) becomes (A.3)

$$\gamma_{LV} \left(dA_{\mathrm{c}} + dA_{\mathrm{f}}\right) - W_{\mathrm{SVL}} dA_{\mathrm{f}} = 0 \tag{A.3}$$

The expression in equation (A.3) can be divided by dA_{f}, giving the following equation:

$$\gamma_{LV} \left(\frac{dA_{\mathrm{c}}}{dA_{\mathrm{f}}} + 1\right) - W_{\mathrm{SVL}} = 0 \tag{A.4}$$

The derivative of A_{c} with respect A_{f} can be easily transformed using the chain rule:

$$\frac{dA_{\mathrm{c}}}{dA_{\mathrm{f}}} = \frac{dA_{\mathrm{c}}}{d\theta}\frac{d\theta}{dA_{\mathrm{f}}} = \frac{\frac{dA_{\mathrm{c}}}{d\theta}}{\frac{dA_{\mathrm{f}}}{d\theta}} \tag{A.5}$$

For a droplet of constant volume these derivatives can be found deriving the area expressions with respect to θ. According to equations (A.1) and (A.2), both areas depend on the radius of the sphere and the contact angle θ. However, the radius may depend on the angle. The volume of a spherical cap has the following expression:

$$V_{\mathrm{cap}} = \frac{\pi h}{6}\left(3a^2 + h^2\right) \tag{A.6}$$

where a and h are the flat area radius and the cap height, respectively (Figure A.1). This equation can be expressed as a function of r and θ:

$$V_{\mathrm{cap}} = \frac{\pi\left(r - r\mathrm{cos}\theta\right)}{6}\left(3\left(r\mathrm{sin}\theta\right)^2 + \left(r - r\mathrm{cos}\theta\right)^2\right) =$$

$$= \frac{\pi r\left(1 - \mathrm{cos}\theta\right)}{6}\left(3r^2\mathrm{sin}^2\theta + r^2\left(1 - \mathrm{cos}\theta\right)^2\right) =$$

$$= \frac{\pi}{6}r^3\left(1 - \mathrm{cos}\theta\right)\left(3\mathrm{sin}^2\theta + \left(1 - \mathrm{cos}\theta\right)^2\right) =$$

$$= \frac{\pi}{6}r^3\left(1 - \mathrm{cos}\theta\right)\left(2\mathrm{sin}^2\theta + \mathrm{sin}^2\theta + \mathrm{cos}^2\theta - 2\mathrm{cos}\theta + 1\right) =$$

$$= \frac{\pi}{6}r^3\left(1 - \mathrm{cos}\theta\right)\left(2\mathrm{sin}^2\theta + 1 - 2\mathrm{cos}\theta + 1\right) =$$

$$= \frac{\pi}{3}r^3\left(1 - \mathrm{cos}\theta\right)\left(\mathrm{sin}^2\theta + 1 - \mathrm{cos}\theta\right) =$$

$$= \frac{\pi}{3}r^3\left(1 - \mathrm{cos}\theta\right)\left(\left(1 - \mathrm{cos}^2\theta\right) + 1 - \mathrm{cos}\theta\right) =$$

$$= \frac{\pi}{3}r^3\left(1 - \mathrm{cos}\theta\right)\left(2 - \mathrm{cos}\theta - \mathrm{cos}^2\theta\right) =$$

$$= \frac{\pi}{3}r^3\left(2 - \mathrm{cos}^2\theta - \mathrm{cos}\theta - 2\mathrm{cos}\theta + \mathrm{cos}^3\theta + \mathrm{cos}^2\theta\right) =$$

$$= \frac{\pi}{3}r^3\left(2 - 3\mathrm{cos}\theta + \mathrm{cos}^3\theta\right) \tag{A.7}$$

Thus, for a spherical cap of constant volume, the radius depends on θ:

$$r = \left(\frac{V_{\mathrm{cap}}}{\frac{\pi}{3}\left(2 - 3\mathrm{cos}\theta + \mathrm{cos}^3\theta\right)}\right)^{\frac{1}{3}} \tag{A.8}$$

Substituting the radius in equations (A.1) and (A.2) and deriving them with respect to θ, one obtains the following relationship:

$$\frac{dA_{\mathrm{c}}}{dA_{\mathrm{f}}} = \cos\theta \tag{A.9}$$

Conclusively, equation (A.4) becomes:

$$\gamma_{LV}\left(\cos\theta + 1\right) = W_{\mathrm{SVL}} \tag{A.10}$$

Appendix B

Rear adhesion force

$$F_{\mathrm{R}} = 2\int_0^{\frac{\pi}{2}} \gamma \mathrm{cos}\theta \cdot \mathrm{cos}\phi R d\phi = 2R\gamma \int_0^{\frac{\pi}{2}} \left[\frac{\phi}{\frac{\pi}{2}} \cdot \mathrm{cos}\theta_{\mathrm{A}} + \left(1 - \frac{\phi}{\frac{\pi}{2}}\right) \cdot \mathrm{cos}\theta_{\mathrm{R}} \right] \cdot \mathrm{cos}\phi d\phi =$$

$$= 2R\gamma \frac{2}{\pi} \mathrm{cos}\theta_{\mathrm{A}} \int_0^{\frac{\pi}{2}} \phi \mathrm{cos}\phi d\phi + 2R\gamma \mathrm{cos}\theta_{\mathrm{R}} \int_0^{\frac{\pi}{2}} \mathrm{cos}\phi d\phi - 2R\gamma \frac{2}{\pi} \mathrm{cos}\theta_{\mathrm{R}} \int_0^{\frac{\pi}{2}} \phi \mathrm{cos}\phi d\phi =$$

$$= \frac{4}{\pi} R\gamma \left(\mathrm{cos}\theta_{\mathrm{A}} - \mathrm{cos}\theta_{\mathrm{R}}\right) \int_0^{\frac{\pi}{2}} \phi \mathrm{cos}\phi d\phi + 2R\gamma \mathrm{cos}\theta_{\mathrm{R}} \Big[\mathrm{sin}\phi\Big]_0^{\frac{\pi}{2}} =$$

$$= \frac{4}{\pi} R\gamma \left(\mathrm{cos}\theta_{\mathrm{A}} - \mathrm{cos}\theta_{\mathrm{R}}\right) \left(\Big[\phi \mathrm{sin}\phi\Big]_0^{\frac{\pi}{2}} + \Big[\mathrm{cos}\phi\Big]_0^{\frac{\pi}{2}} \right) + 2R\gamma \mathrm{cos}\theta_{\mathrm{R}} =$$

$$= \frac{4}{\pi} R\gamma \left(\mathrm{cos}\theta_{\mathrm{A}} - \mathrm{cos}\theta_{\mathrm{R}}\right) \left(\frac{\pi}{2} - 1\right) + 2R\gamma \mathrm{cos}\theta_{\mathrm{R}} =$$

$$= 2R\gamma \mathrm{cos}\theta_{\mathrm{A}} - \frac{4}{\pi} R\gamma \mathrm{cos}\theta_{\mathrm{A}} - 2R\gamma \mathrm{cos}\theta_{\mathrm{R}} + \frac{4}{\pi} R\gamma \mathrm{cos}\theta_{\mathrm{R}} + 2R\gamma \mathrm{cos}\theta_{\mathrm{R}} =$$

$$= 2R\gamma \mathrm{cos}\theta_{\mathrm{A}} - \frac{4}{\pi} R\gamma \mathrm{cos}\theta_{\mathrm{A}} + \frac{4}{\pi} R\gamma \mathrm{cos}\theta_{\mathrm{R}} \tag{B.1}$$

Appendix C

Spherical cap volume

The volume of a spherical cap (Figure A.1 in Appendix A is computed according to the following equation:

$$V_{cap} = \frac{\pi \delta_s}{6}\left(3\left(\frac{c_s}{2}\right)^2 + \delta_s^2\right) \tag{C.1}$$

where c_s is the droplet chord, which is computed using equation (2.69), and the distance δ (Figure 2.4) can be computed using equation (2.45):

$$\delta_s = R_s\left(1 + \mathrm{cos}\theta_s\right) \tag{C.2}$$

Thus, using equations (2.69) and (C.2), equation (C.1) yields:

$$V_{cap} = \frac{\pi R_s\left(1+\mathrm{cos}\theta_s\right)}{6}\left(3\left(R_s\mathrm{sin}\theta_s\right)^2 + R_s^2\left(1+\mathrm{cos}\theta_s\right)^2\right) =$$

$$= \frac{\pi}{6}R_s^3\left(1+\mathrm{cos}\theta_s\right)\left[3\mathrm{sin}^2\theta_s + 1 + 2\mathrm{cos}\theta_s + \mathrm{cos}^2\theta_s\right] \tag{C.3}$$

The term between brackets in equation (C.3) can be further simplified:

$$3\mathrm{sin}^2\theta_s + 1 + 2\mathrm{cos}\theta_s + \mathrm{cos}^2\theta_s = 2\mathrm{sin}^2\theta_s + \mathrm{sin}^2\theta_s + 1 + 2\mathrm{cos}\theta_s + \mathrm{cos}^2\theta_s =$$

$$= 2\mathrm{sin}^2\theta_s + 1 + 2\mathrm{cos}\theta_s + 1 = 2\left(\mathrm{sin}^2\theta_s + 1 + \mathrm{cos}\theta_s\right) \tag{C.4}$$

On the other hand:

$$\mathrm{sin}^2\theta_s = 1 - \mathrm{cos}^2\theta_s = \left(1-\mathrm{cos}\theta_s\right)\left(1+\mathrm{cos}\theta_s\right) \tag{C.5}$$

Substituting the term $\mathrm{sin}^2\theta_s$ in equation (C.4), it yields:

$$2\left(\mathrm{sin}^2\theta_s + 1 + \mathrm{cos}\theta_s\right) = 2\left[\left(1-\mathrm{cos}\theta_s\right)\left(1+\mathrm{cos}\theta_s\right) + 1 + \mathrm{cos}\theta_s\right] =$$

$$= 2\left(1+\mathrm{cos}\theta_s\right)\left[\left(1-\mathrm{cos}\theta_s\right) + 1\right] = 2\left(1+\mathrm{cos}\theta_s\right)\left(2-\mathrm{cos}\theta_s\right) \tag{C.6}$$

Getting back to equation (C.3), the term between brackets is substituted by the simplified term in equation (C.6):

$$V_{cap} = \frac{\pi}{6} R_s^3 \left(1 + \cos\theta_s\right) 2 \left(1 + \cos\theta_s\right) \left(2 - \cos\theta_s\right) = \frac{\pi}{3} R_s^3 \left(1 + \cos\theta_s\right)^2 \left(2 - \cos\theta_s\right) \tag{C.7}$$

Appendix D

MATLAB codes

D.1 main.m

```
clear all
clc

%% Initial data
rho_w = 1e3;        % water density [kg m-3]
rho_air = 1.205;    % air density [kg m-3]
mu_air = 1.98e-5;   % air viscosity [kg m-1 s-1]
sigma = 7.2e-2;     % water surface tension [N m-1]
u_air = 14.5;       % air velocity [m s-1]
H = 13e-3;          % channel height [m]
theta_s = 137.29;   % static contact angle [deg]
Q = 0.1;            % water flow rate [uL s-1]
c0 = 0.1;           % initial chord [mm]

theta_s_deg = theta_s;
theta_s = theta_s*pi/180;

% Time vector
nt = 10001;                              % number of time step sizes
t_min = 0;                              % initial time [s]
t_max = 1;                              % final time [s]
t = linspace(t_min,t_max,nt);           % time vector [s]
dt = (t_max - t_min)/(length(t)-1);     % time step

% Volume and mass vector
kQ = 1e-6*1e-3;  % factor to have Q in [m3 s-1]
Q = Q*kQ;
V0 = ((c0*1e-3/(2*sin(theta_s)))^3)*((4/3)*pi - ...
    (pi/3)*((1+cos(theta_s))^2)*(2-cos(theta_s))); %[m^3]
V = Q*t + V0; %[m^3]
% According to Esposito:
V0_Esp = ((c0*1e-3/(2*sin(theta_s)))^3)*((4/3)*pi - ...
    pi*((1+cos(theta_s))^2)*cos(theta_s)); %[m^3]
V_Esp = Q*t + V0_Esp; %[m^3]
% Simple model:
Rs_simp = c0*1e-3/(2*sin(theta_s));             %[m]
delta_s = Rs_simp*(1 + cos(theta_s));           %[m]
h_s = 2*Rs_simp - delta_s;                      %[m]
V0s = (pi*h_s/6)*(3*(c0*1e-3/2)^2 + h_s^2);     %[m^3]
V_simp = Q*t + V0s;                             %[m^3]
```

```
m = V*rho_w;            %[kg]

% Chord vector
Rs = 1e3*(V/((4/3)*pi - (pi/3)*((1+cos(theta_s))^2)*...
    (2-cos(theta_s)))).^(1/3); %[mm]
c = 2*Rs*sin(theta_s);  % [mm]
c_min = min(c);         % droplet chord length at t = t_min [mm]
c_max = max(c);         % droplet chord length at t = t_max [mm]

% Ideal xCM
xCM_ideal = c/2;
h_ideal = Rs - Rs.*cos(theta_s);

% Initial xCM
xCM = zeros(1,length(c));
xCM(1) = c(1)/2;

% droplet thickness:
td = Rs*((4*pi/3 - (pi/3)*((1+cos(theta_s))^2)*...
    (2-cos(theta_s)))/(theta_s - sin(2*theta_s)/2));

%% theta_r model
thrmod = 0;

%% Model and size of the plots choice

% % Surface tension force model
disp(' ')
disp('Choose a model for the surface tension force')
disp(' ')
disp('         [0]: Model 1 - Spring model')
disp('         [1]: Model 2 - Adhesion model')
disp(' ')
modelact = input('Choose an option (default: 1):  ');
if isempty(modelact)
    modelact = 1;
end

% Size of the plots
disp(' ')
disp('Choose a size of the resulting image')
disp(' ')
disp('         [0]: Big')
disp('         [1]: Small')
disp(' ')
sizeact = input('Choose an option (default: 0):  ');
if isempty(sizeact)
    sizeact = 0;
end

if modelact == 0
    % h(\theta) function for the surface tension force:
    theta_s_func = 90:10:170;
    h_func = [0.92,0.7,0.49,0.36,0.25,0.16,0.09,0.04,0.01];
    p_h_func = polyfit(theta_s_func,h_func,2);
    h_func_fit = polyval(p_h_func,theta_s_deg);
    % thickness, radius, perimeter and surface of the undeformed droplet:
    td_0 = Rs*((4*pi/3 - (pi/3)*((1+cos(theta_s))^2)*...
    (2-cos(theta_s)))/(theta_s - sin(2*theta_s)/2));
    P_0 = 2*Rs*theta_s;
```

```
    A_0 = (Rs.^2)*(theta_s - sin(2*theta_s)/2);
    S_0 = td_0.*P_0 + 2*A_0;
else
    % Adhesion force parameters
    k = 2;
    % k = ones(1, length(c))*4/pi;
end

%% Loop over time - solution of xCM in every step

%Preallocation of the result vectors
theta_a = zeros(1,length(c));
theta_r = zeros(1,length(c));
hyst = zeros(1,length(c));
R = zeros(1,length(c));
h = zeros(1,length(c));
P = zeros(1,length(c));
Re_h = zeros(1,length(c));
Cd = zeros(1,length(c));
Ad = zeros(1,length(c));
Fdrag = zeros(1,length(c));
Fst = zeros(1,length(c));
y = zeros(2,length(c));

% Boundary conditions
y(1,1) = xCM(1);    % Initial position
y(2,1) = 0;         % Initial velocity

for I = 1:(length(t)-1)
    % Geometrical variables at time I
    [theta_a(I),theta_r(I),R(I),h(I),P(I)] = ...
    geomodule(c(I),theta_s,xCM(I),c_max,t(I),thrmod);
    hyst(I) = theta_a(I) - theta_r(I);
    assert(hyst(I)<1,...
    'Detachment condition reached at time t = %5.4f s. Height is h = %5.4f mm', t(I), h(I)
    hmass = (m(I) + m(I+1))/2;
    hchord = (c(I) + c(I+1))/2;
    hthick = (td(I) + td(I+1))/2;

    % Forces according to us
    Re_h(I) = rho_air*u_air*(h(I)*1e-3)/mu_air;
    Cd(I) = Cdfunc(Re_h(I),hyst(I+1));
    Ad(I) = (R(I)^2)*(theta_s - sin(2*theta_s)/2); %[mm^2]
    Fdrag(I) = (1/2)*rho_air*(u_air^2)*Cd(I)*(Ad(I)*1e-6);

    if modelact == 0
        Fst(I) = -sigma*(S_0(I)*h_func_fit/Rs(I)^2)*(xCM(I) - c(I)/2)/1000;
    else
        Fst(I) = sigma*k*(td(I)*1e-3).*(cos(theta_r(I)) - cos(theta_a(I)));
    end

    % Solution @t = t_n+1/2 of the governing equation for the current time - RK4
    k1 = [y(2,I);(1/m(I))*(Fst(I)-Fdrag(I))];
    yapprox = y(:,I) + (dt/2)*k1;

    % Geometrical variables at time I+1/2 using approximated solution yapprox(1)
    [theta_a(I+1),theta_r(I+1),R(I+1),h(I+1),P(I+1)] = ...
        geomodule_nd(c(I+1),theta_s,yapprox(1),thrmod);
    hyst(I+1) = theta_a(I+1) - theta_r(I+1);
    Re_h(I+1) = rho_air*u_air*(h(I+1)*1e-3)/mu_air;
```

```
    Cd(I+1) = Cdfunc(Re_h(I+1),hyst(I+1));
    Ad(I+1) = (R(I+1)^2)*(theta_s - sin(2*theta_s)/2); %[mm^2]
    Fdrag(I+1) = (1/2)*rho_air*(u_air^2)*Cd(I+1)*(Ad(I+1)*1e-6);

    if modelact == 0
        Fst(I+1) = -sigma*(S_0(I+1)*h_func_fit/Rs(I+1)^2)*...
        (yapprox(1) - c(I+1)/2)/1000;
    else
        Fst(I+1) = sigma*k*(hthick*1e-3).*...
        (cos(theta_r(I+1)) - cos(theta_a(I+1)));
    end

    k2 = [yapprox(2);(1/hmass)*(Fst(I+1)-Fdrag(I+1))];
    yapprox = y(:,I) + (dt/2)*k2;

    % Geometrical variables at time I+1/2 using approximated solution yapprox(1)
    [theta_a(I+1),theta_r(I+1),R(I+1),h(I+1),P(I+1)] = ...
        geomodule_nd(c(I+1),theta_s,yapprox(1),thrmod);
    hyst(I+1) = theta_a(I+1) - theta_r(I+1);
    Re_h(I+1) = rho_air*u_air*(h(I+1)*1e-3)/mu_air;
    Cd(I+1) = Cdfunc(Re_h(I+1),hyst(I+1));
    Ad(I+1) = (R(I+1)^2)*(theta_s - sin(2*theta_s)/2); %[mm^2]
    Fdrag(I+1) = (1/2)*rho_air*(u_air^2)*Cd(I+1)*(Ad(I+1)*1e-6);

    if modelact == 0
        Fst(I+1) = -sigma*(S_0(I+1)*h_func_fit/Rs(I+1)^2)*...
        (yapprox(1) - c(I+1)/2)/1000;
    else
        Fst(I+1) = sigma*k*(hthick*1e-3).*...
        (cos(theta_r(I+1)) - cos(theta_a(I+1)));
    end

    k3 = [yapprox(2);(1/hmass)*(Fst(I+1)-Fdrag(I+1))];
    yapprox = y(:,I) + dt*k3;

    % Geometrical variables at time I+1 using approximated solution yapprox(1)
    [theta_a(I+1),theta_r(I+1),R(I+1),h(I+1),P(I+1)] = ...
        geomodule_nd(c(I+1),theta_s,yapprox(1),thrmod);
    hyst(I+1) = theta_a(I+1) - theta_r(I+1);
    Re_h(I+1) = rho_air*u_air*(h(I+1)*1e-3)/mu_air;
    Cd(I+1) = Cdfunc(Re_h(I+1),hyst(I+1));
    Ad(I+1) = (R(I+1)^2)*(theta_s - sin(2*theta_s)/2); %[mm^2]
    Fdrag(I+1) = (1/2)*rho_air*(u_air^2)*Cd(I+1)*(Ad(I+1)*1e-6);

    if modelact == 0
        Fst(I+1) = -sigma*(S_0(I+1)*h_func_fit/Rs(I+1)^2)*...
        (yapprox(1) - c(I+1)/2)/1000;
    else
        Fst(I+1) = sigma*k*(hthick*1e-3).*...
        (cos(theta_r(I+1)) - cos(theta_a(I+1)));
    end

    k4 = [yapprox(2);(1/m(I+1))*(Fst(I+1)-Fdrag(I+1))];

    y(:,I+1) = y(:,I) + dt*(k1/6 + k2/3 + k3/3 + k4/6);
    xCM(I+1) = y(1,I+1);
end
```

D.2 geomodule.m

```matlab
function [theta_a_out,theta_r_out,R_out,h_out,P_out] = ...
 geomodule(c, theta_s, xCM_in,c_max)
%% Initial data
theta_a = linspace(theta_s,pi,40);
theta_r = f_theta_r(theta_a);

alfa = theta_a - pi/2;
beta = theta_a - theta_r;

%% R, A, h and P using theta_r and theta_r_fit
R = c.*sin(theta_r)./(1 + sin(theta_a).*sin(theta_r) - ...
    cos(theta_a).*cos(theta_r));

A_circ = pi*(R.^2);
A_CT = ((R.^2)/2).*(beta - sin(beta));
A_AHC = ((R.^2)/2).*(pi - 2*alfa - sin(pi - 2*alfa));
A_CTE = 2*(R.^2).*(sin(beta/2).^2).*sin(theta_r+(beta/2)).*(sin(beta/2) - ...
    sin(theta_r+(beta/2)).*cos(theta_r))./sin(theta_r);
A_ETB = 2*(R.^2).*(sin(beta/2).^2).*(sin(theta_r+(beta/2)).^2)./tan(theta_r);
A_CTB = (2*(R.^2).*((sin(beta/2)).^3).*(sin(theta_r + beta/2)))./(sin(theta_r));
A = A_circ - A_AHC - A_CT + A_CTB;

h = R.*(1 - cos(theta_a));

P = 2*R.*sin((theta_a-theta_r)/2).*sin((theta_a+theta_r)/2)./sin(theta_r) + ...
    R.*(theta_a+theta_r);

%% xCM depending on theta_r and theta_r_fit
% Circle:
xCM_circ = R.*sin(theta_a);
%yCM_circ = -R.*cos(theta_a);

% Circular sector CT:
alfa3 = (theta_a + theta_r)/2 - pi/2;
xCM_CT = xCM_circ + ((2/3)*R.*(sin(beta/2).^3)./...
    (beta/2 - sin(beta)/2)).*cos(alfa3);
xCM_CT(1) = c;

% Circular sector AH'C:
xCM_AHC = R.*sin(theta_a);

% Triangle CTE:
xCM_CTE = 2*R.*sin(theta_a) + (2/3)*(2*R.*sin(beta/2).*(sin(beta/2) - ...
    sin(theta_r+beta/2).*cos(theta_r))./sin(theta_r));
%yCM_CTE = (2/3)*R.*sin(beta/2).*sin(theta_r+beta/2);

% Triangle ETB:
xCM_ETB = 2*R.*sin(theta_a) + 2*R.*(sin(beta/2).^2)./(sin(theta_r)) - ...
    (2/3)*(2*R.*sin(beta/2).*sin(theta_r+beta/2)./tan(theta_r));

% Triangle CTB:
xCM_CTB = (xCM_CTE.*A_CTE + xCM_ETB.*A_ETB)./A_CTB;
xCM_CTB(1) = c;

% Droplet:
xCM = (xCM_circ.*A_circ - xCM_CT.*A_CT - xCM_AHC.*A_AHC + xCM_CTB.*A_CTB)./A;

%% fitting curves for theta_a, R, h and P depending on xCM
p_theta_a = polyfit(xCM,theta_a,1);
p_R = polyfit(xCM,R,2);
```

```
p_h = polyfit(xCM,h,2);
p_P = polyfit(xCM,P,2);

%% Computation of theta_a, theta_r, R, h and P with input xCM
theta_a_out = polyval(p_theta_a,xCM_in);
theta_r_out = f_theta_r(theta_a_out);
R_out = polyval(p_R,xCM_in);
h_out = polyval(p_h,xCM_in);
P_out = polyval(p_P,xCM_in);

%% Droplet drawing
xO = R_out*sin(theta_a_out);
yO = -R_out*cos(theta_a_out);
xB = c;
yB = 0;
alfa_out = theta_a_out - pi/2;
gamma = pi/2 - theta_r_out;
xT = xO + R_out*cos(gamma);
yT = yO + R_out*sin(gamma);

theta_min = pi + (pi/2 - (pi/2 - alfa_out));
theta_max = gamma;
theta = theta_min:-0.01:theta_max;
xcirc = xO + R_out*cos(theta);
ycirc = yO + R_out*sin(theta);

xtan = linspace(xT,xB,100);
ytan = linspace(yT,yB,100);

figure(1)
plot(xcirc,ycirc,'b-',xtan,ytan,'b-','LineWidth',4);

xminplot = -0.6*c_max;
xmaxplot = xminplot + 2*c_max;
yminplot = 0;
ymaxplot = 2*c_max;
axis ([xminplot,xmaxplot,yminplot,ymaxplot])
axis off
```

D.3 4th order Runge-Kutta algorithm

```
% This program solves a 2nd order ODE with a known exact solution
% in order to prove that the numerical algorithm is correct

clear all
clc

%% Initial data

% Time vector
nt = 10;                              % number of time step sizes
t_min = 0;                              % initial time [s]
t_max = 1;                              % final time [s]
t = linspace(t_min,t_max,nt);           % time vector [s]
dt = (t_max - t_min)/(length(t)-1);     % time step

% Exact solution
yexact = exp(t) - t.*exp(t);
```

```
% Preallocation of the result vector
y = zeros(2,length(t));

% Boundary conditions
y(1,1) = 1;
y(2,1) = 0;

%% Loop over time - solution of xCM in every step

for I = 1:(length(t)-1)
    % Solution @t = t_n+1/2 of the governing eq for the current time - RK4
    k1 = [y(2,I);2*y(2,I)-y(1,I)];
    yapprox = y(:,I) + (dt/2)*k1;

    % Solution at time I+1/2 using approximated solution yapprox(1)
    k2 = [yapprox(2);2*yapprox(2)-yapprox(1)];
    yapprox = y(:,I) + (dt/2)*k2;

    % Solution at time I+1/2 using approximated solution yapprox(1)
    k3 = [yapprox(2);2*yapprox(2)-yapprox(1)];
    yapprox = y(:,I) + dt*k3;

    % Solution at time I+1 using approximated solution yapprox(1)
    k4 = [yapprox(2);2*yapprox(2)-yapprox(1)];

    y(:,I+1) = y(:,I) + dt*(k1/6 + k2/3 + k3/3 + k4/6);
end

%% Error
err = abs(yexact - y(1,:));
```